The Dissertation Committee for Taehyung Kim
certifies that this is the approved version of the following dissertation:

Transmission Grid Strength Analysis and Operation of Inverter-Based Microgrids

Committee:

Surya Santoso, Supervisor

Xianyong Feng

Alex J. Hanson

Alex Q. Huang

Hao Zhu

Transmission Grid Strength Analysis and Operation of Inverter-Based Microgrids

by

Taehyung Kim

DISSERTATION

Presented to the Faculty of the Graduate School of

The University of Texas at Austin

in Partial Fulfillment

of the Requirements

for the Degree of

DOCTOR OF PHILOSOPHY

The University of Texas at Austin

May 2022

Abstract

Transmission Grid Strength Analysis and Operation of Inverter-Based Microgrids

Taehyung Kim, Ph.D.
The University of Texas at Austin, 2022

Supervisor: Surya Santoso

Renewable energy resources interfaced using inverters contribute insignificant inertia and short-circuit capacity to the power system. As a result, frequency response and voltage regulation may be adversely affected. For this reason, this work focuses on evaluating transmission system strength and operation of microgrids with inverter-interfaced resources.

The strength of the transmission grid with large wind farms is investigated based on the voltage phase angle stability. A novel approach for evaluating the strength of low-inertia systems that only relies on phasor measurement unit (PMU) data is proposed and implemented to the Panhandle region of the ERCOT system. The proposed metric evaluates the system strength by calculating the sensitivity of the voltage phase angle to the change of active power flow without using network parameters. The advantages of the proposed method are demonstrated using PMU field data collected from the ERCOT system.

This work also focuses on microgrids with inverters. Detailed electromagnetic models of grid-forming and grid-following inverters are discussed,

and their equivalent models are developed to improve computation efficiency for steady-state analysis. The equivalent circuit model is developed based on the voltage and current control loops with a current limiter. The current limiting algorithm for the steady-state solver is developed and incorporated into the short-circuit study process.

Moreover, voltage imbalance mitigation control of grid-forming inverters supplying unbalanced loads is analyzed. The performance of a grid-forming inverter with voltage balancing capability is demonstrated by blackstarting an islanded microgrid with an unbalanced load and an induction motor. Simulation results showed that the inverter can maintain balanced voltage at nominal value and limit the large unbalance current required to start the motor load. However, the magnitude of the negative-sequence current an inverter can supply is limited by its relatively low rated current. Therefore, we investigate the range of negative-sequence current the inverter can supply and derive formulas to determine the minimum capacity required to supply unbalanced loads interfaced with a delta-wye grounded transformer.

Finally, we analyze the power-sharing control of grid-forming inverters in unbalanced circuits. Even though conventional droop controls, designed to share active and reactive powers, are well-developed, they cannot contribute to assigning negative-sequence currents to each inverter. This work presents an adaptive negative-sequence virtual impedance control which allows inverters to inject negative-sequence current proportionally to their capacities. Simulation results show that inverters with the proposed method regulate both positive- and negative-sequence currents as desired.

Table of Contents

List of Tables

List of Figures

Chapter 1

Introduction

This chapter outlines the research on inverter-based resources in transmission and distribution systems. Background and motivation for this research are shown in Section 1.1. Literature review is presented in Section 1.2, whereas research objectives and contributions are shown in Section 1.3.

1.1 Background and Motivation

The electric power system is undergoing significant changes with the advances in energy conversion technologies. Power systems are evolving to have large amounts of inverter-based renewable resources such as wind and solar generators. As of 2021, there are 26 GW of wind power and 7 GW of solar power installed in the ERCOT grid [1].

However, inverter-based resources introduce challenges to conventional power systems where the main power source is synchronous generators (SGs) [2]. Renewable resources do not provide inertia support [3] and have a low short-circuit capacity compared to SGs [4]. As a result, inverter-interfaced resources adversely affect frequency response and voltage regulation.

In distribution systems, maintaining balanced voltage while supplying an unbalanced load is a major concern. According to ANSI C84.1, voltage imbalance must not exceed 3% [5]. Inverters can participate in voltage imbal-

ance compensation, but their performance is limited due to their relatively low rated capacity [6]. The negative-sequence current the inverter can supply is much lower in comparison to the SG.

Therefore, this work focuses on evaluating transmission system strength and operation of microgrids with inverter-interfaced resources. First, the strength of a low inertia transmission system with large-scale wind farms is examined based on their voltage phase angle stability. Subsequently, models of inverters used in islanded microgrids are developed, and their voltage balancing capability is analyzed. The objective of this work is summarized in Fig. 1.1.

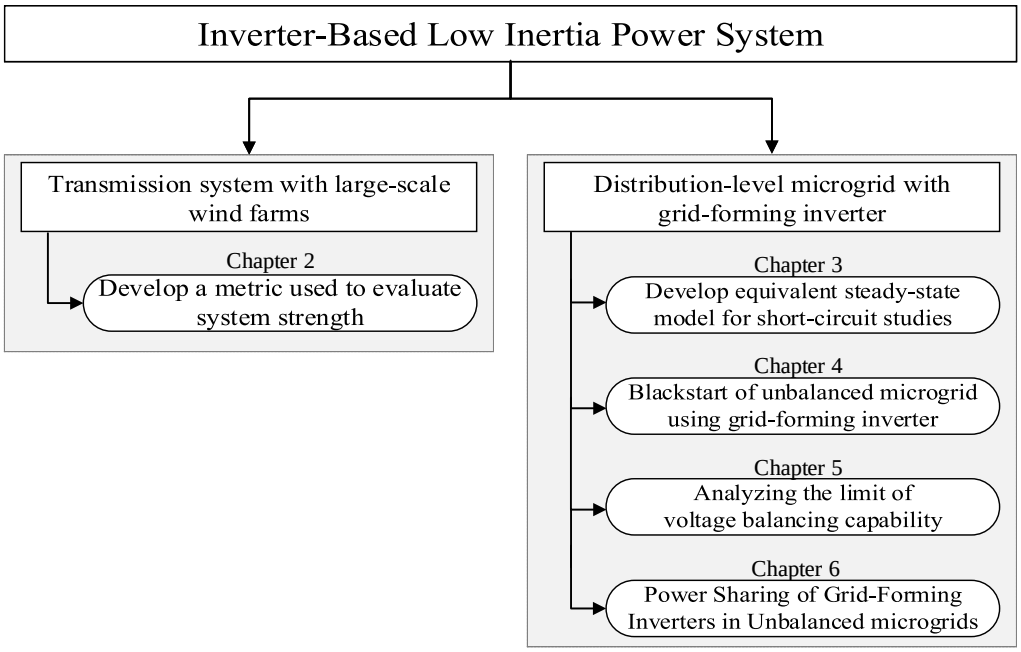

Figure 1.1: The outline of the proposed research.

1.2 Review of the State of the Art

1.2.1 Strength of Transmission Systems with Large Wind Farms

Integrating a large amount of wind generation adversely affected the strength of the ERCOT system and make the grid more susceptible to disturbances [7]. The system strength issue is more crucial at the remote parts of the transmission grids, such as the Panhandle region [2]. Therefore, evaluating system strength and identifying weak parts are important tasks for system operators.

There are several methods developed to define and evaluate the strength of power systems with inverter-based resources. In [3, 8–11], system strength is described in terms of short-circuit capacity (SCMVA) and voltage stability. SCMVA of a system consisting of inverter-interfaced resources is lower than that of the same system if it consisted of SGs of the same size. Those systems are considered as "weak" systems in terms of SCMVA [8]. These weak systems experience various voltage issues after disturbance. In weak systems, faults induce voltage oscillation [3] and delay voltage recovery [9]. Also, low-voltage ride-through (LVRT) controllers of wind farms do not perform well in weak systems [10], and wind turbines become vulnerable to faults [11].

Short-circuit ratio (SCR) is the most common method used to evaluate the strength of systems hosting wind power projects with respect to SCMVA [4]. However, as electrical distances get smaller between wind farms, SCR becomes less effective because SCR neglects the interaction between wind plants [12]. Authors of [12] proposed using a weighted short-circuit ratio (WSCR) to include the interactions between wind farms. Furthermore, site-dependent short-circuit ratio (SDSCR) is developed in [13] to consider the real electrical network connections between wind farms. However, these

methods require a Thevenin equivalent impedance or three-phase short-circuit current to compute the SCMVA of the system. As power systems become more complex and larger, calculating them will require more computation, and the results could become less accurate.

System inertia has become a widely used criterion for evaluating system strength as more inverter-interfaced resources are introduced in power systems [14–17]. Compared to SG-based grids, low inertia systems have the following characteristics, 1) insufficient frequency response and 2) large rate of change of frequency (RoCoF) [14]. Since wind turbine's rotor speed and system frequency are decoupled, wind turbines can only provide limited frequency response and inertia support [15]. Lack of inertial response causes a large RoCoF after disturbance and results in malfunction of SGs and inverters [14, 16, 17].

With the development of PMUs and wide-area monitoring system, [18] and [19] proposed to use PMU measurements to evaluate the system strength by estimating system inertia. Reference [18] proposed to use PMU frequency measurements to estimate the system inertia during a high wind period. It showed that system inertia could be estimated using measured power and RoCoF data captured during system disturbances. Reference [19] subsequently showed that the inertia could be estimated using steady-state data alone. However, these methods still require inertia constants of SGs to estimate the system inertia. Thus, this work presents a PMU-based metric which does not require network parameters.

1.2.2 Distribution Microgrids with Inverter-Based Resources

Modeling and Simulation of Grid-Following and Grid-Forming Inverters

In many modern microgrids, inverter-interfaced distributed generators (IIDGs) are the primary power source. Conventionally, inverters in microgrids operate in a grid-following mode with an SG. They control the active and reactive power injected into the microgrid and require a phased-locked loop (PLL) and a voltage reference generated from SGs [20]. However, modern microgrids may not have SG, especially when operating in islanded mode. Without a SG, the microgrid requires at least one inverter operating in grid-forming mode, which is capable of controlling the grid voltage and frequency without external support. Therefore, inverters operating in both modes have to be considered for islanded microgrid studies.

Inverters are mostly modeled using EMT tools because of their power electronic switches and complicated control structures [21]. However, dynamic models developed in EMT tools require a large computational effort, which is not necessary for steady-state analysis, such as a short-circuit study.

Steady-state equivalent models of grid-following and grid-forming inverters have been developed to improve computational efficiency [22–26]. A steady-state model of grid-following inverter operating in grid-connected mode was presented in [22]. An equivalent model of droop controlled grid-following inverters was analyzed in [23, 24].

Equivalent models of grid-forming inverters were proposed in [25, 26]. The authors of [25] developed an equivalent model for normal operating conditions. However, the current limiting control, which is crucial for short-circuit studies, was not included. An equivalent model with current limiting control was developed in [26]. It developed a steady-state model by calculating positive- and negative-sequence equivalent impedances of the inverter considering its control loop and current limiter.

Although equivalent models proposed in [22–26] had good accuracy, their performances were not analyzed when used in a microgrid with multiple inverters operating in different modes. Short-circuit studies of microgrids with multiple inverters were discussed in [27], but the impact of inverters on microgrid protection was analyzed in time-domain simulation. Therefore, we focus on a short-circuit analysis of an islanded microgrid with multiple inverters using a steady-state solver. The equivalent model of inverter and current limiting strategy are developed and incorporated into the short-circuit analysis process.

Blackstart operation of microgrids is also an important task that must be performed by inverter-based resources. Blackstarting a microgrid is needed for its formation or restoration after a complete shutdown due to internal short-circuit faults, DG outages, or switching events [28]. Blackstart of the power systems was mostly done by SGs that could set the voltage and frequency of the system [29]. DGs with inverters operating in a grid-following mode could not blackstart an islanded grid because they only control the power injected into the grid and require a phase-locked loop (PLL) with an external voltage reference.

However, the development of grid-forming control [20] made inverters capable of blackstarting microgrids. Unlike grid-following inverters, grid-forming inverters are modeled as a voltage source, and controls the voltage magnitude and frequency of microgrids. Therefore, additional voltage reference and PLL are not required, as they can set their own voltage and frequency.

Blackstart operation using inverter-based resources was analyzed in [30–32]. In [30], a hierarchical control of inverter that enables the inverter to blackstart an islanded microgrid was developed. In [31] and [32], blackstart

operation using a dynamic model of grid-forming inverter was presented. However, in [31], the inverter and current limiter were modeled as a voltage source with a variable resistor. On the other hand, [32] focused on voltage control without considering current limiter for motor start. This work aims to regulate the inverter current during the blackstart process and demonstrate the grid-forming inverter's blackstarting capability.

Voltage Balancing Capability of Grid-Forming Inverters

In microgrids, IIDGs must participate in compensation for grid voltage imbalance because they are the primary power source. Unbalanced voltage compensation of IIDGs depends on the mode of operation. IIDGs in microgrids generally operate in two modes: 1) grid-following and 2) grid-forming mode [20]. Inverters operating in both modes could mitigate voltage unbalance by controlling their output currents.

Inverters operating in both grid-following and grid-forming modes could mitigate voltage unbalance by controlling their output currents. Grid-following inverter's unbalanced voltage mitigating control is analyzed in [33–35]. A control strategy based on symmetrical components for short-term unbalanced voltage sags is proposed in [33]. Controls for long-term voltage imbalance are proposed in [34] and [35] with different control objectives. In [34], the grid-following inverter aims to maximize active power injection. The control scheme presented in [35] focuses on minimizing negative-sequence voltage magnitude and inverter output current. However, grid-following inverters, which are modeled as a current source with active and reactive power reference signals, can mitigate voltage imbalance to an extent but cannot completely eliminate negative-sequence voltage.

IIDGs operating in grid-forming mode have better control over unbalanced voltages because they directly control the grid voltage magnitude and frequency [36–38]. Grid-forming inverters can reduce the negative-sequence voltage to a negligible level by controlling the positive- and negative-sequence voltages separately [36]. The stability of an inverter operating based on this method was evaluated in [37]. Reference [38] showed that grid-forming inverter could control sequence components and maintain balanced voltage both in grid-connected and islanded microgrids.

Previous studies [36–38] showed that grid-forming inverters are capable of maintaining balanced voltage. However, the range of unbalanced load the inverter can handle without losing balanced voltage is not addressed. Although inverters are equipped with a negative-sequence voltage controller, they often cannot supply a large amount of negative-sequence current because of their low rated current compared to synchronous machines. Therefore, this work analyzes and identifies the range of grid-forming inverter's voltage balancing capability serving three-phase unbalanced loads.

As more inverters with grid-forming functions are installed in microgrids, allocating the power injected from grid-forming inverters becomes an issue. Unlike grid-following inverters, grid-forming inverters require additional functions to ensure correct power-sharing.

The active power (P) - frequency (ω) and reactive power (Q) – voltage magnitude (V) droop controls are widely used to share the power supplied by grid-forming inverters [39]. Yet, a droop-based reactive power sharing controller does not perform properly if the inverters have different line impedances and control parameters [40]. Various control strategies have been developed to improve reactive power sharing accuracy. Reference [41] proposed to elimi-

nate reactive power distribution error by injecting a disturbance signal. An improved Q - V droop control was developed in [42], but the output powers of inverters were not allocated accurately when DGs have local loads. Therefore, a virtual impedance controller was proposed in [43] to be used in islanded microgrids.

Previous works in [41–43] showed that P - ω and Q - V droop controls performed well in balanced systems. However, conventional droop control does not contribute to allocating negative-sequence currents. Without an additional controller, negative-sequence currents supplied by each inverter are determined based on the negative-sequence equivalent impedance between the load and the inverter. Reference [44] proposed a method to adjust the negative-sequence impedance by adding a virtual impedance. The ratios of current supplied by each DGs were improved but is still not proportional to the rated capacity of each inverter. This study proposes a droop-based adaptive negative-sequence virtual impedance controller and demonstrate that both positive- and negative-sequence currents are shared properly according to the sizes of inverters.

1.3 Research Objectives and Contributions

This section identifies the research objectives of the work presented herein, and lists the major contributions. Based on the discussion in Section 1.1, the main focuse of this work is inverter-based low inertia power systems including both transmission and distribution systems. The scope of this research is described below.

1.3.1 Objectives and Contributions on Evaluating Transmission System Strength

Objective 1: Develop a PMU-based metric to evaluate the transmission system strength.

The objective of this work is to develop a metric which does not rely on network data. Previous SCR and inertia based methods require system parameters, which may not be available as systems get larger. With the availability of PMU data, we propose a PMU-based metric which can be used to evaluate system strength. The proposed metric utilizes PMU data (voltage magnitude, voltage phase angle, and line power flow) and calculates the sensitivity of voltage angle to power change.

Contributions to Objective 1:

In Chapter 2, a PMU-based metric is developed and implemented using field data obtained from PMUs in the Panhandle region. The theoretical concept of voltage angle sensitivity is analyzed in terms of system inertia and voltage angle sensitivity, and formulas for calculating angle sensitivity are derived. Also, a regression based algorithm which improves the efficiency of calculation is developed. The performance of the proposed metric is validated through time-domain simulation using PSCAD/EMTDC.

The application of proposed method is demonstrated by analyzing the strength of lines and buses in the Panhandle area. Case studies shows that the proposed metric can reflect the varying system strength affected by changes in network states. The weak and strong parts of the Panhandle region are identified, and the result is consistent with the works using network data.

Publication:

– **T. Kim**, A. F Bastos, P. Gravois, M. Miller, N. Kadel, J. Schmall, S. H. Huang, W. Blevins, W. M Grady, and S. Santoso, "Evaluating Strength of Transmission System with Wind Plants Using Voltage Angle Sensitivity Metrics Based on PMU Measurements", in *IEEE Transaction on Sustainable Energy (submitted).*

– **T. Kim**, A. F. Bastos, S. Santoso, W. M. Grady, P. Gravois, M. Miller, N. Kadel, J. Schmall, S. H. Huang, and B Blevins, "PMU-Based Evaluation of Transmission Bus Strength through Angle Sensitivity Metrics", in *IEEE Power and Energy Society General Meeting, Montreal, August 2020, pp. 1-5*

1.3.2 Objectives and Contributions on Operation of Inverter-Based Distribution Microgrids

Objective 2: Develop models of inverters for both EMT and steady-state simulation.

The goal is to develop simulation models of grid-following and grid-forming inverters used in stand-alone microgrids. Detailed EMT models of grid-following and grid-forming inverters are necessary to understand the behavior of inverters for microgrid studies. In addition, steady-state models of inverters are also needed to analyze the inverter's performance in large systems and improve the computation efficiency. Therefore, the models of inverters for both EMT and steady-state analysis are investigated.

Contributions to Objective 2:

In this context, Chapter 3 presents a dynamic model of an inverter which can operate in both grid-following and grid-forming modes by providing different reference signals. Moreover, equivalent impedance models based on inverter control parameters are proposed for steady-state short-circuit stud-

ies. Equivalent models and current limiting strategy are developed and incorporated into the short-circuit analysis process. The accuracy of the proposed equivalent model is examined by comparing the short-circuit node voltages and line currents computed using OpenDSS with those obtained from PSCAD/EMTDC using detailed models.

Publication:

– **T. Kim**, N. Barry, W. Kim, S. Santoso, V. C. Cunha, W. Freitas, W. Wang, R. Dugan, D. Ramasubramanian, and A. Maitra, "Modeling and Simulation of Short-Circuit Faults in Inverter-Based Microgrids Using Steady-State Equivalent Circuits", in *IEEE Power and Energy Society General Meeting*, Denver, July 2022, *(Accepted)*.

Objective 3: Analyze the blackstart capability grid-forming inverters in microgrids.

Blackstart operation was mostly responsible for SGs in conventional systems. However, as grid-forming control of inverters evolve, inverters became capable of blackstarting stand-alone microgrids by generating voltage and frequency without external support. Therefore, the objective is to develop an inverter model which can handle the large transformer inrush current and supply reactive power during the motor start. In addition, the grid-forming inverter also aims to compensate for grid voltage unbalance to improve the power quality.

Contributions on Objective 3:

Chapter 4 presents the blackstart operation of islanded microgrid using only a grid-forming inverter. The inverter is designed to maintain balanced

grid voltage at its nominal value by controlling both positive- and negative-sequence voltages. The current limiter is modified to operate in the abc-frame to regulate the large unbalanced current during motor start and energizing events. The performance of the grid-forming inverter is evaluated by black-starting an islanded microgrid with a motor load. Simulation results show that the grid-forming inverter can blackstart an islanded microgrid and generate its own voltage to energize loads and transformers. It is also shown that the inverter can start the motor while limiting the associated inrush current.

Publication:

– **T. Kim**, V. C. Cunha, S. Santoso, W. Wang, R. Dugan, D. Ramasubramanian, and A. Maitra, "Blackstart of Unbalanced Microgrids Using Grid-Forming Inverter with Voltage Balancing Capability", in *2022 IEEE T & D Conference and Exposition*, New Orleans, April 2022, *(Accepted)*.

Objective 4: Analyze the voltage balancing capability of grid-forming inverters.

The voltage imbalance is one of the main concerns in distribution systems. As inverter-based resources become dominant in islanded microgrids, they must participate in voltage unbalance compensation. This work focuses on analyzing the voltage balancing capability of grid-forming inverters. The objective is to analyze and identify the range of voltage balancing capability of grid-forming inverters serving three-phase unbalanced loads. Also, zero-sequence paths of the inverter's interconnection transformer with different connections are examined to improve the inverter's voltage balancing capability.

Contributions on Objective 4:

The inverter's voltage balancing capability was analyzed in Chapter 5. This work focused on three-phase three-leg grid-forming inverters commonly

used in distribution systems. They can deliver positive- and negative-sequence currents, but do not have a path for zero-sequence current, which can be provided by the inverter's interconnection transformer or a separate grounding transformer. Thus, the relationship between the transformer connection and the zero-sequence is examined, and the limit of negative-sequence current the inverter can supply is analyzed.

Additionally, this work proposed a method to calculate the required capacity of the grid-forming inverter to supply a given unbalanced system. With delta connection on the inverter side of the interconnection transformer, it is challenging to estimate the amount of required current when the system is unbalanced. The proposed method accounts for the delta-wye grounded connection of the inverter transformer, and the inverter's size can be computed using only the load size and power factor without requiring analytical methods and simulations.

Publication:

– **T. Kim**, N. Barry, W. Kim, S. Santoso, W. Wang, R. Dugan, D. Ramasubramanian, and A. Maitra, "Voltage Balancing Capability of Grid-Forming Inverters", in *IEEE Open Access Journal of Power and Energy (Submitted).*

Objective 5: Analyze the power-sharing control of grid-forming inverters.

Conventional droop controls perform well in the general case, but their behaviors are greatly affected by line impedance. Also, they are designed to regulate positive-sequence currents supplied by inverters. Therefore, this work focuses on improving negative-sequence current allocation. The objective is to develop an adaptive negative-sequence virtual impedance controller and

improve the power-sharing capability of grid-forming inverters in distribution microgrid.

Contributions on Objective 5:

Power-sharing control of grid-forming inverters is addressed in Chapter 6. With a conventional droop controller, the negative-sequence current supplied by the inverter is determined by the equivalent impedance between the inverters and the loads. An adaptive virtual impedance controller was proposed and demonstrated through simulation studies to share the negative-sequence current proportionally to inverters' sizes. The simulation results show that the adaptive controller regulates the negative-sequence current regardless of the I_2/I_1 ratio of the load and inverters could inject currents as desired.

Chapter 2

Evaluating Strength of Transmission System Strength with Wind Plants

2.1 Introduction

Evaluating system strength and identifying weak parts are becoming important tasks as large wind farms are interconnected to the power system [2]. There are several metrics developed to estimate system strength, as discussed in Section 1.1. The main challenge of existing methods is that they cannot be used without network data. We propose a metric that does not require any system parameter and only relies on PMU measurements. The performance of the proposed metric is validated through time-domain simulation using PSCAD/EMTDC, and the strength of buses and lines in the Panhandle region is evaluated using PMU field data.

This chapter is organized as follows. In Section 2.2, the Panhandle region transmission system and PMUs installed in the Panhandle region are

---

Parts of the work presented in this chapter appear in the following published papers:

– **T. Kim**, A. F Bastos, P. Gravois, M. Miller, N. Kadel, J. Schmall, S. H. Huang, W. Blevins, W. M Grady, and S. Santoso, "Evaluating Strength of Transmission System with Wind Plants Using Voltage Angle Sensitivity Metrics Based on PMU Measurements", in *IEEE Transaction on Sustainable Energy (submitted)*.

– **T. Kim**, A. F. Bastos, S. Santoso, W. M. Grady, P. Gravois, M. Miller, N. Kadel, J. Schmall, S. H. Huang, and B Blevins, "PMU-Based Evaluation of Transmission Bus Strength through Angle Sensitivity Metrics", in *IEEE Power and Energy Society General Meeting*, Montreal, August 2020, pp. 1-5.

introduced. Theoretical background of the proposed metric is analyzed in Section 2.3. Section 2.4 presents equations for angle sensitivity metric, and the method of calculating the metric using PMU measurement is introduced in Section 2.5. The proposed method is validated using PSCAD/EMTDC in Section 2.6, and Section 2.7 presents case study results and discussions. Finial considerations are addressed in Section 2.8.

2.2 Motivation and System Description

2.2.1 The Panhandle Transmission System with Multiple Large Wind Farms

The main focus of this chapter is evaluating the strength of buses in a remote region having multiple large wind farms. The simplified 345 kV network of the region and the selected PMUs are presented in Fig. 2.1 and Table 2.1. PMUs shown in Table 2.1 are named as PMU#@MonitoredBus, where the monitored bus refers to the bus where PMU# is located. The remote location is the other end of the line that PMU# is monitoring. For example, PMU5@WINDMILL is located at Windmill and measures the voltage magnitude and angle of Windmill. It also monitors the power flowing from Windmill to Ogallala (see Fig. 2.1). This region is chosen as a study area because (a) it hosts a large number of wind projects, (b) it is relatively remote from the rest of the ERCOT network and the main load center, and (c) PMUs are already available at 345 kV buses throughout the region. There are over 8 GW of wind power plants installed in the Panhandle and Nearby Panhandle areas, and the wind power is transmitted to the main grid through Riley and Clear Crossing [45]. The first three selected PMUs are located at the northern edge of the network, while the last two PMUs are located closer to the center of the

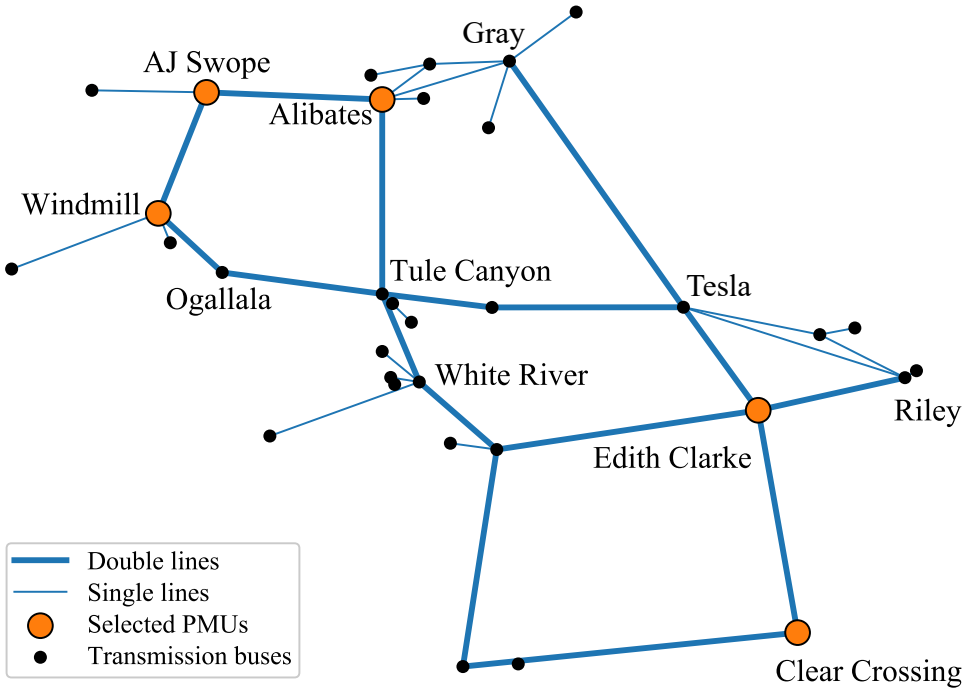

Figure 2.1: A simplified 345 kV network of the Panhandle region and locations of selected PMUs.

ERCOT system.

An example of a 12-hour long PMU measurement from PMUs at AJ Swope and Edith Clarke is shown in Fig. 2.2. These two buses are selected as representative of buses located far and near the load center. The PMU data contains voltage magnitude, voltage angle, and line power flow measured on a day in Spring 2019. The voltage magnitudes shown in Fig. 2.2(a) are the per-unit voltage magnitudes of AJ Swope and Edith Clarke. The voltage angles presented in Fig. 2.2(b) are the relative voltages angle with respect to the reference bus, Killeen, which is a stable bus located at the center of the system. The DC offset of voltage angles is removed to compare the fluctuation of voltage angles of remote and close buses. The power flowing from AJ Swope

Table 2.1: Selected PMUs Installed in the Panhandle Region.

PMU name	Monitored Bus	Remote Location
PMU5@WINDMILL	Windmill	Ogallala
PMU3@AJ Swope	AJ Swope	Alibates
PMU5@ALIBATES	Alibates	Tule Canyon
Riley1L901@EClk	Edith Clarke	Riley
EClk1@ClrCrossng	Clear Crossing	Edith Clarke

to Alibates and Edith Clarke to Riley are displayed in Fig. 2.2(c).

2.2.2 Motivation of the Proposed Metric and Defining System Strength in Terms of Voltage Phase Angle

From Fig. 2.2(a), it can be seen that voltage magnitudes of both AJ Swope and Edith Clarke do not vary significantly, and controlled at 1.03 pu and 1.025 pu, respectively. In contrast, the voltage angles (Fig. 2.2(b)) and line power flows (Fig. 2.2(c)) fluctuate as wind condition varies. Fig. 2.2(b) shows that voltage angle fluctuation is more severe at AJ Swope (blue curve) than Edith Clarke (orange curve). This behavior can be understood by observing the network topology and relative location of AJ Swope and Edith Clarke. It can be inferred that AJ Swope, which is located at the edge of the grid with large wind projects, has a relatively unstable voltage angle compared to Edith Clarke.

Considering the above-mentioned general understanding, we explore and propose a new metric to evaluate grid strength. The proposed metric only uses PMU measurement without system data, such as network topology and generator parameters. PMU data are used to determine the change of the bus's voltage angle for a given change of power flowing through the monitored ele-

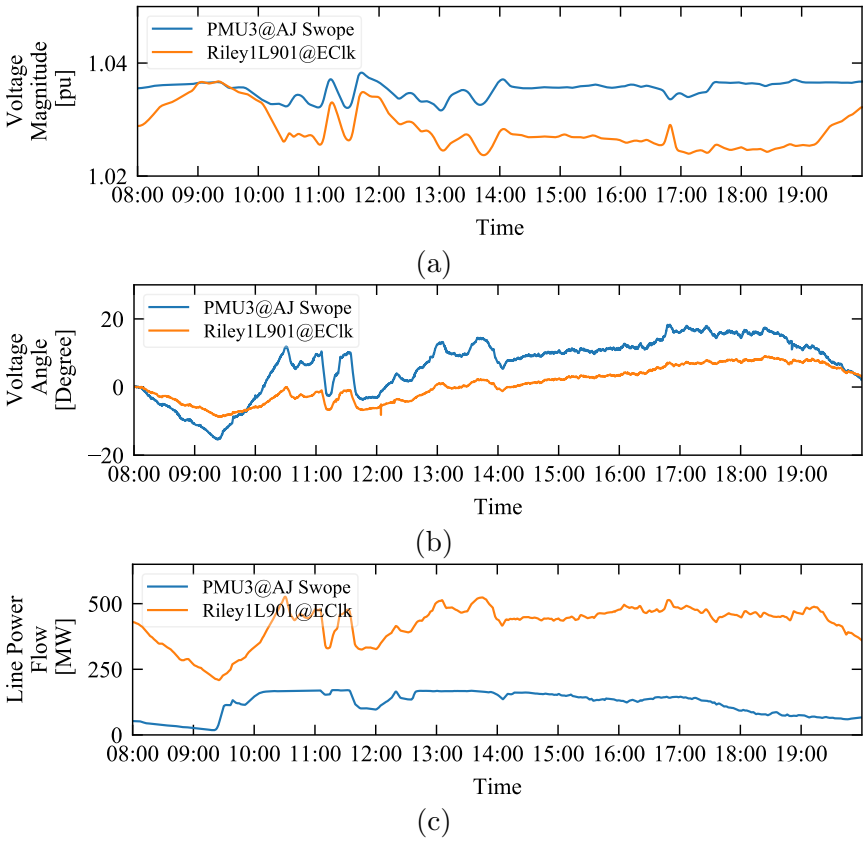

Figure 2.2: Example of PMU measurement collected from AJ Swope and Edith Clarke. (a) Voltage magnitude. (b) Voltage angle. (c) Line power flow.

ment. The metric attempts to measure the sensitivity of voltage phase angle to the change of power, i.e., $\Delta\delta/\Delta P$. If the metric returns a high value, the voltage phase angle is more responsive to the change of power, and thus it indicates a weaker bus. Put in another way, buses in a weaker grid tend to experience larger voltage phase angle variations compared to those in a stronger grid for the same level of power change.

2.3 Theoretical Background

This section presents formulas to understand the subtlety of system strength by examining system inertia and voltage angle stability. First, the relationship between inertia and voltage angle is presented. Then the system strength is defined in terms of the voltage angle stability.

2.3.1 Impact of Low Inertia on Voltage Phase Angle

The dynamics between voltage phase angle and system inertia can be derived from the swing equation shown in (2.1). The swing equation of multiple machines can be written using the concept of center of inertia (COI) [46]. The voltage phase angle and frequency of COIs can represent the behavior of generators in the area. In this chapter, we consider 345 kV transmission buses in the Panhandle region as COIs. The swing equation for COIs can be written as follows:

$$M_{COI}\frac{d^2\delta_{COI}}{dt^2} = \Delta P_{e,COI} - \Delta P_{m,COI}, \tag{2.1}$$

$$\delta_{COI} = \frac{1}{M}\sum_{i=1}^{N} M_i\delta_i, \tag{2.2}$$

$$M_{COI} = \sum_{i=1}^{N} M_i, \tag{2.3}$$

where M_{COI} is the sum of inertia moments of generators, δ_{COI} is the equivalent voltage angle, $P_{e,COI}$ is electrical power, and $P_{m,COI}$ is the mechanical power of generators. From (2.1), it can be seen that M_{COI} has a close relationship with the steadiness of voltage angle. Systems with high inertia moment will have stable voltage angles, while voltage angles of low inertia systems will have a larger variation.

Large-scale wind farms installed in the Panhandle region degrade the voltage angle dynamics because 1) wind farms do not contribute to inertia unless it has inertia supporting control [47] and 2) rapid wind power fluctuation introduces a large power mismatch. Thus, voltage angles of buses with wind farms are volatile compared to buses connected to SGs. In this article, the steadiness of voltage angle is used as a criterion to evaluate system strength.

2.3.2 Defining System Strength According to Voltage Angle Stability

The swing equation of COIs showed that low inertia contribution of wind farms induces a large fluctuation in voltage angle. In this section, behavior of voltage angle of weak and strong systems are analyzed. The relationship between system strength and voltage angle can be explained by (2.4) and P-δ curve shown in Fig. 2.3. The power flow between two buses is given as follows,

$$P_0 = P_{max} \sin \delta_0, \tag{2.4}$$

$$P_{max} = \frac{V_1 V_2}{X_{line}}, \tag{2.5}$$

where V_1 and V_2 are voltage magnitudes of each bus at the ends of the line; δ_0 is the voltage angle difference between two buses; P_0 is the line power flow; X_{line} is the reactance of the line. Two P-δ curves of System A and System B with different P_{max} are shown in Fig. 2.3. It can be seen that System A has a lower transmission limit compared to System B. Concerning transmission capability, we define System A as a weak system, and System B as a strong system.

When there is a change in electrical power, i.e., increased wind generation, the voltage phase angle shifts to the new operating point. In Fig. 2.3,

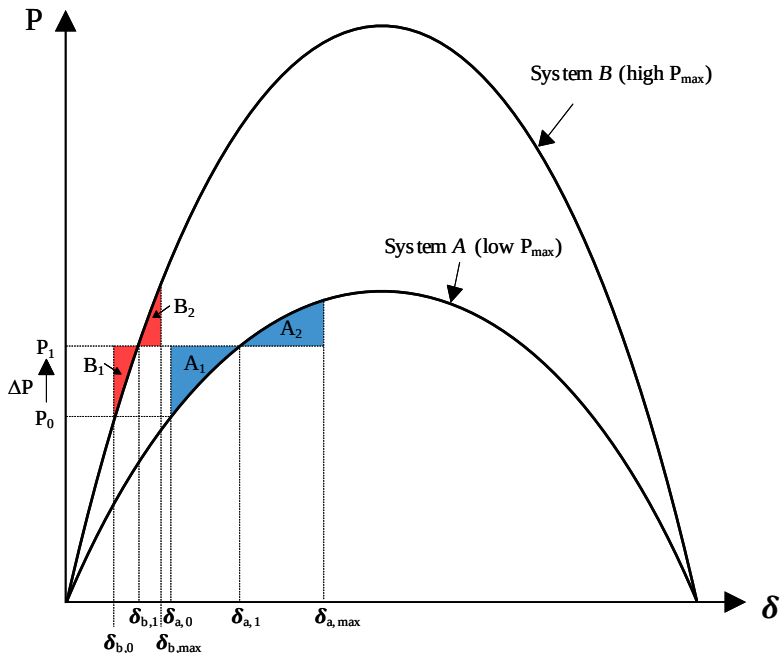

Figure 2.3: The P-δ curve of the two bus system.

when electrical power increases by ΔP from P_0 to P_1, δ_{ab}, which is aggregated voltage angles of System A and B, also increase from $\delta_{ab,0}$ to $\delta_{ab,1}$. However, the voltage angle cannot be adjusted immediately because of system inertia. The voltage angle oscillates between $\delta_{ab,0}$ and $\delta_{ab,max}$ until $\frac{d\delta}{dt}$ reaches 0.

The maximum voltage angle $\delta_{ab,max}$ during transient has to remain within $0 < \delta_{ab,max} < \frac{\pi}{2}$ to keep the voltage angle synchronized. Therefore, tracking $\delta_{ab,max}$ is important to maintain angle stability. Instead of solving (2.1), we can use equal area criterion to determine $\delta_{ab,max}$:

$$\int_{\delta_{ab,0}}^{\delta_{ab,1}} (P_1 - P_{ab,max} \sin\delta)\, d\delta = \int_{\delta_{ab,1}}^{\delta_{ab,max}} (P_{ab,max} \sin\delta \ - P_1)\, d\delta. \qquad (2.6)$$

The left side of (2.6) presents accelerating areas $A1$ and $B1$, and the right side shows decelerating areas $A2$ and $B2$ in Fig. 2.3. As shown in Fig. 2.3, the

amount of accelerating or decelerating power is different in weak and strong systems, and it results in different ranges of voltage angle oscillations. Maximum voltage angle $\delta_{a,max}$ is much larger compared to $\delta_{b,max}$ even though power change was the same in both systems. In other words, the voltage angle of the weak system oscillates more (more sensitive to power change) and has a higher chance of voltage angle divergence. Therefore, we can classify weak and strong buses according to the voltage angle sensitivity. Buses with high angle sensitivity, whose voltage angle could diverge easily, are defined as weak buses. On the contrary, buses which have a less sensitive voltage angle are considered as strong buses.

2.4 Proposed Method: Voltage Angle Sensitivity to Power Change

Formulas to calculate the voltage angle sensitivity to power change are developed in this section. The angle sensitivity of both line and bus could be calculated by choosing different remote ends as shown in Fig. 2.4. We calculate the angle sensitivity of lines using the voltage angle difference between the monitored element and the remote element. On the other hand, the angle sensitivity of buses is computed using the voltage angle difference calculated with respect to the voltage angle of the reference bus.

2.4.1 Calculating the Angle Sensitivity of Monitored Lines

We first develop equations for calculating the angle sensitivity of line shown in Fig. 2.4(a). The angle sensitivity can be computed by applying a

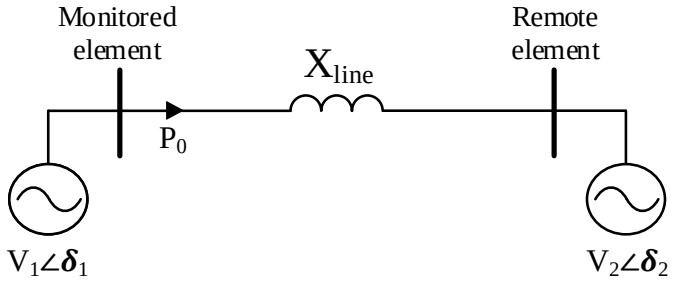

(a)

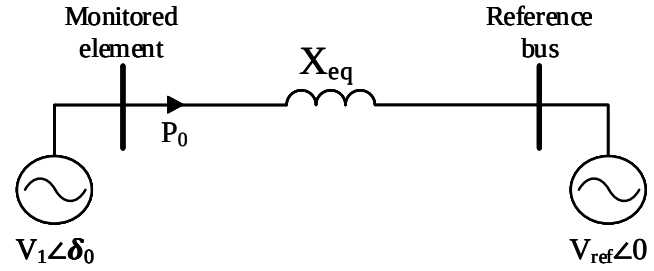

(b)

Figure 2.4: Equivalent two-bus systems with PMU observing (a) line. (b) bus.

small change of power (ΔP) and angle ($\Delta\delta$) to (2.4) as shown below,

$$P_0 + \Delta P = P_{max}\sin(\delta_0 + \Delta\delta), \tag{2.7}$$

$$= P_{max}(\sin\delta_0\cos\Delta\delta + \cos\delta_0\sin\Delta\delta). \tag{2.8}$$

Since $\Delta\delta$ is a small perturbation, $\cos\Delta\delta$ and $\sin\Delta\delta$ in (2.8) could be approximated to 1 and $\Delta\delta$, respectively. Also, P_0 is equal to $P_{max}\sin\delta_0$ as shown in (2.4). Therefore, (2.8) can be approximated to (2.10) as follows,

$$P_0 + \Delta P \approx P_{max}\sin\delta_0 + P_{max}\cos\delta_0\cdot\Delta\delta, \tag{2.9}$$

$$\frac{\Delta\delta}{\Delta P} = \frac{1}{P_{max}\cos\delta_0}. \tag{2.10}$$

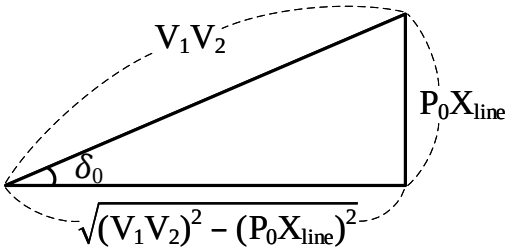

Figure 2.5: Pythagorean identity of power transfer equation.

By rearranging (2.4), we can draw a right triangle shown in Fig. 2.5. Using the Pythagorean identity, we represent $\cos\delta_0$ as (2.12).

$$\sin\delta_0 = \frac{P_0 X_{line}}{V_1 V_2}, \tag{2.11}$$

$$\cos\delta_0 = \frac{\sqrt{(V_1V_2)^2 - (P_0X_{line})^2}}{V_1V_2}. \tag{2.12}$$

By substituting P_{max} and $\cos\delta_0$ in (2.10) with $\frac{V_1V_2}{X_{line}}$ and (2.12), the angle sensitivity metric can be expressed as

$$\frac{\Delta\delta}{\Delta P} = \frac{X_{line}}{\sqrt{(V_1V_2)^2 - (P_0X_{line})^2}}. \tag{2.13}$$

From the above equation, it is clear that the angle sensitivity is influenced by voltage magnitudes at line ends (V_1 and V_2), the line reactance (X_{line}), and the power flows from Bus 1 to Bus 2, P_0. Note that line reactance, which cannot be obtained from PMU measurements, appears in (2.13). Therefore, we do not use (2.13) to compute the angle sensitivity. The method to calculate voltage angle sensitivity numerically using PMU measurements is described in Section 2.5.

2.4.2 Calculating Angle Sensitivity of Buses by Introducing Reference Bus

The formula to calculate the angle sensitivity of the line is proposed in (2.13). In other words, it gauges the strength of a line. By introducing a reference bus, (2.13) is modified to use bus quantities to evaluate bus strength. In this study, it is reasonable to choose a PMU installed at the strongest bus in the system. In our example, Killeen is chosen because Killeen is a strong bus located near the center of the system.

Fig. 2.4(b) illustrates a two-bus system with one end of the line replaced with a reference bus. The bus under consideration (monitored bus) has voltage phasor of $V_1\angle\delta_0$ while the reference bus has voltage phasor of $V_{ref}\angle 0$. Voltage phase angle δ_0 represents the angle difference between the bus under consideration and the reference bus, i.e., $\delta_0 = \delta_1 - \delta_{ref}$. Without loss of generality, δ_{ref} is set to 0. The reactance X_{eq} in Fig. 2.4(b) is an equivalent reactance between the monitored bus and reference bus. This equivalent reactance may comprise a parallel and series combination of equipment impedances between the monitored and reference buses. Please note that X_{eq} is not a line reactance but an equivalent reactance as if a line existed between the monitored bus and the reference bus. Additionally, it is important to note that P_0 is PMU-measured power quantity flowing through the equivalent reactance, from the monitored bus to the remote bus, which is the bus at the other end of the line. Given these assumptions, the angle sensitivity metric used for bus strength is modified as below,

$$\frac{\Delta\delta}{\Delta P} = \frac{X_{eq}}{\sqrt{(V_1 V_{ref})^2 - (P_0 X_{eq})^2}}. \tag{2.14}$$

2.4.3 Factors Affecting Angle Sensitivity

The equations for calculating the angle sensitivity of lines and buses are shown in (2.13) and (2.14). They consists of three variables which affect the angle sensitivity.

- Voltage magnitude: Voltage magnitude has an inverse relationship with the angle sensitivity. Buses with lower voltage magnitude than its nominal will likely have higher angle sensitivity.
- Reactance: Reactance appears in both numerator and denominator, but the reactance in the numerator is more dominant. Therefore, the voltage angle of the line with higher reactance or equivalent reactance will be more sensitive to power change.
- Line power flow: The power flowing in the line is also an important factor for angle sensitivity. The more power flows through the line, the higher the angle sensitivity value is.

Fig. 2.6 shows the relationship between the bus voltage angle sensitivity, power, and equivalent reactance. As shown in Fig. 2.2(a), voltage magnitude is assumed well-controlled at 1 pu. Each curve represents a system with different equivalent reactance, from 0.4 pu to 0.7 pu. The power flowing in the line varies from 0 to 1 pu, and each curve shows the corresponding angle sensitivities. It can be observed that the system which has higher equivalent reactance has higher angle sensitivity, and it is more affected by the increase of the line power flow. For example, in the case where the reactance is 0.4 pu, the angle sensitivity changes from 0.4 deg/MW to 0.44 deg/MW, i.e., by 10%. On the other hand, when the reactance is 0.6 pu, the angle sensitivity increases by 25% from 0.6 deg/MW to 0.75 deg/MW.

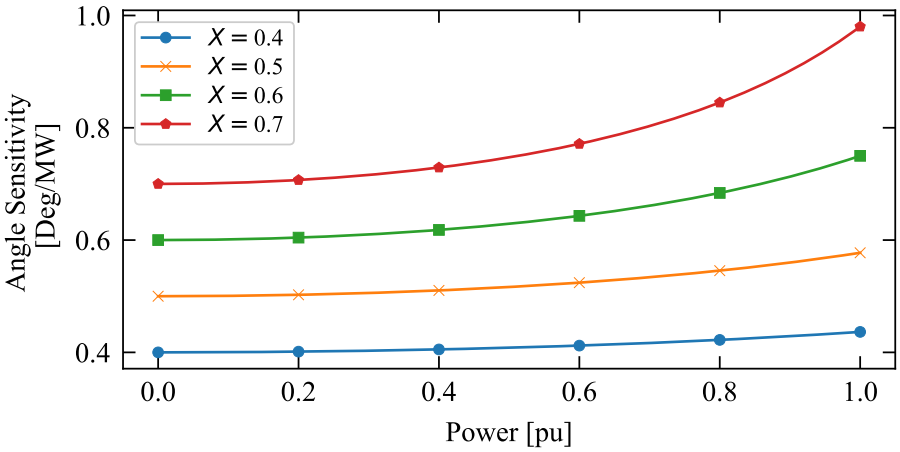

Figure 2.6: The line angle sensitivity with varying power and line reactance.

2.5 Computing Angle Sensitivity Using PMU Measurements

2.5.1 Calculating Angle Sensitivity of a Single Point

The simplest way to calculate the angle sensitivity would be using formulas developed in Section 2.4. However, reactance X_{line} and X_{eq} are not available from PMU measurement, and obtaining the reactance from other datasets will vitiate the benefit of using the proposed metric. Therefore, an alternative method which only uses measured voltage angle and line power flow is developed. Calculating the difference between two voltage angle samples $\delta(n)$ and $\delta(n + t \cdot n_s)$ would be the most straightforward method, where n_s is the sampling rate of PMU data and t is the time interval used to calculate the change in voltage angle. But the angle sensitivity calculated in this manner results in numerous discontinuous points and spikes because of noise in measurements. Hence, an approach using linear regression is introduced. Instead of directly calculating the voltage angle and power changes, slopes of regression lines are used to calculate the angle sensitivity. The regression lines

of voltage angle and power could be expressed as follow,

$$y_{angle} = A_0 + k_A t, \tag{2.15}$$

$$y_{power} = P_0 + k_P t, \tag{2.16}$$

where k_A and k_P are slopes of regression lines, and A_0 and P_0 are the y-intercepts. Angle sensitivity can be directly calculated from PMU measurements using the coefficients k_A and k_P as below.

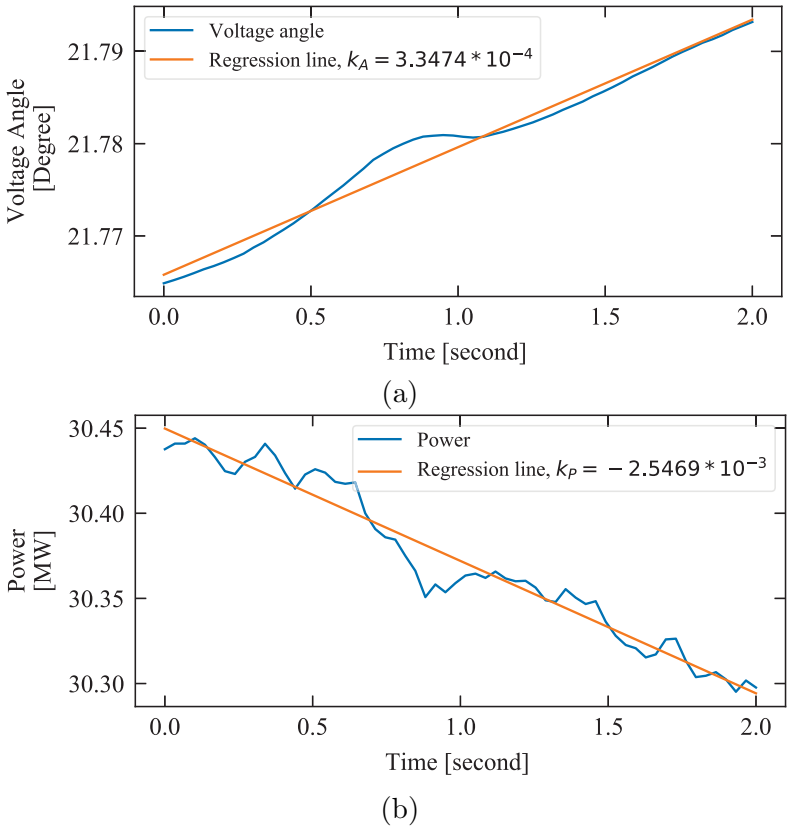

Figure 2.7: PMU measurements and their regression lines. (a) Voltage angle. (b) Line power flow.

$$\frac{\Delta\delta}{\Delta P} = \left| \frac{\delta(n) - \delta(n + t \cdot n_s)}{P(n) - P(n + t \cdot n_s)} \right|, \tag{2.17}$$

$$= \left| \frac{\frac{\delta(n)-\delta(n+t\cdot n_s)}{t}}{\frac{P(n)-P(n+t\cdot n_s)}{t}} \right| = \left| \frac{k_A}{k_P} \right|. \tag{2.18}$$

An example of the PMU measurements and their regression lines are shown in Fig. 2.7. The angle sensitivity for this example case is $\left|\frac{k_A}{k_P}\right| = \left|\frac{3.3474\cdot 10^{-4}}{-2.5924\cdot 10^{-3}}\right| = 0.1314$ deg/MW.

2.5.2 Analyzing Angle Sensitivity Using Hourly Dataset

Angle sensitivity samples calculated as described in the previous section result in time-series data. Although linear regression is applied, spurious values still exist, so they are discarded by imposing following criteria:

- Remove values obtained from small voltage angle and power changes: the angle sensitivities obtained from small voltage angle and power changes are discarded to remove worthless points and prevent dividing by 0 or a very small number. Angle sensitivities obtained from samples where $\Delta\delta < 0.005^\circ$ and $\Delta P < 0.25$ MW are discarded.

- Remove values obtained from regression with low R^2 scores: the data within the selected window not always resemble the regression line. For example, it could contain a change in the polarity of the slope. We discard the values when the R^2 score is lower than 0.9 because these cases indicate that a line is not a good approximation for the measurements.

After discarding spurious data, an additional filter is applied to better manage the large dataset consisting of hourly measurement. A moving average filter shown in (2.19) is used to better understand the tendency of angle

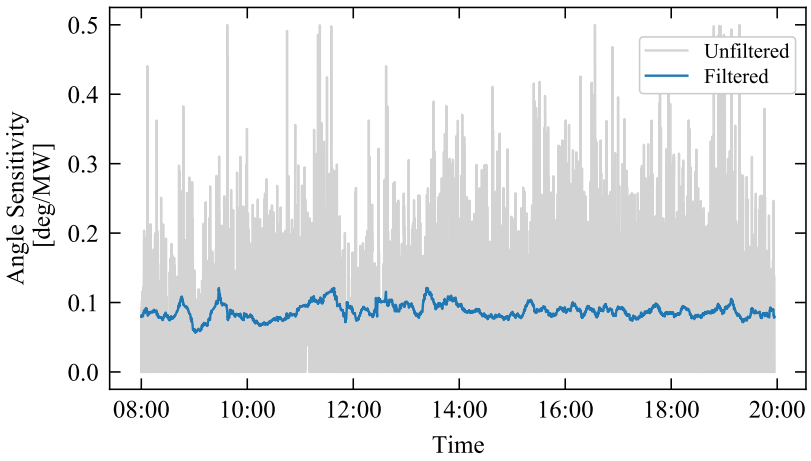

Figure 2.8: The calculated angle sensitivity before and after the filter is applied.

sensitivity.

$$\frac{\Delta\delta}{\Delta P}(i) = \frac{1}{n}\sum_{i=0}^{n-1}\frac{\Delta\delta}{\Delta P}(i). \tag{2.19}$$

An example of filtered and unfiltered angle sensitivity calculated using 12-hour long data obtained from Windmill is shown in Fig. 2.8. It can be seen that angle sensitivity becomes continuous after removing ineffective values. The process of calculating the angle sensitivity metric is summarized in Fig. 2.9.

2.6 Validation of the Proposed Metric

This section validates the performance of the proposed metric using time-domain PSCAD/EMTDC simulation. Voltage angle and power injected to each bus are simulated, and angle sensitivity is calculated using the method introduced in Section 2.5.

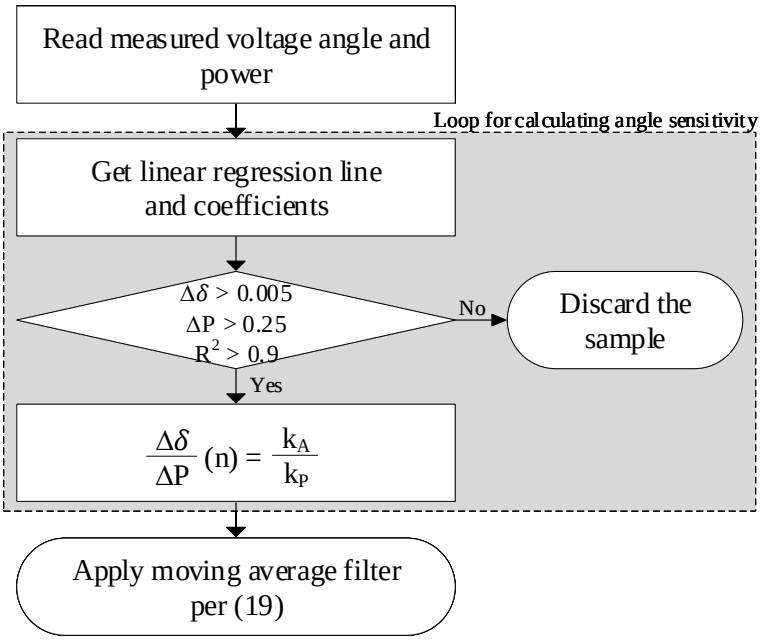

Figure 2.9: Flow chart of calculating the angle sensitivity.

2.6.1 System Description and Simulation Scenario

The modified IEEE 14-bus test system shown in Fig. 2.10 is chosen to be studied [48]. Types and locations of generators are adjusted as shown in Table 2.2. Two Type 4 wind turbines [49] are connected to Bus 1 and Bus 12, while SGs with high inertia are installed on Bus 2 and Bus 8. Loads are placed

Table 2.2: Generators in the Modified IEEE 14 Bus System

Unit	Generator model	Location	Rated capacity [MVA]	Inertia [s]
Gen 1	Sync. machine	Bus 2	1000	6
Gen 2	Sync. machine	Bus 8	750	6
Wind 1	Type 4	Bus 1	400	-
Wind 2	Type 4	Bus 12	200	-

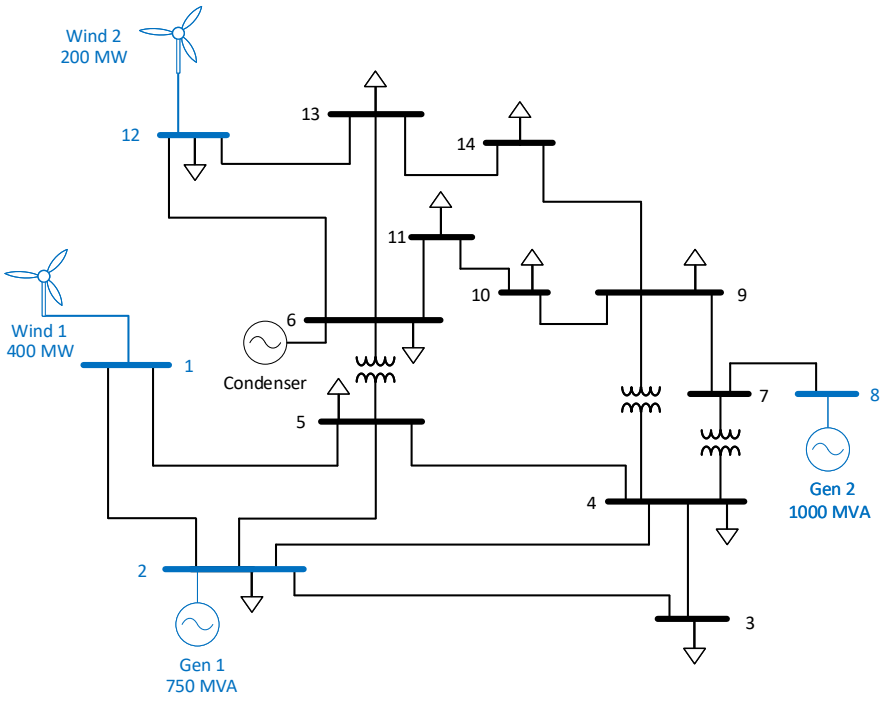

Figure 2.10: Modified IEEE 14 bus system with wind farms.

at the same locations, but the sizes are tripled to accommodate wind farms. Total load installed in the system has increased to 777 MW + 220.5 Mvar. A synchronous condenser at Bus 6 is kept to support the voltage of buses near wind farms.

Strength of buses with generators are selected to be analyzed. Locations, types, and rated capacities of selected buses are highlighted in blue in Fig. 2.10. Their strengths are evaluated by comparing angle sensitivities while wind power ramps up. Wind speed increase from 11 m/s to over 13 m/s in 10 seconds as shown in Fig. 2.11.

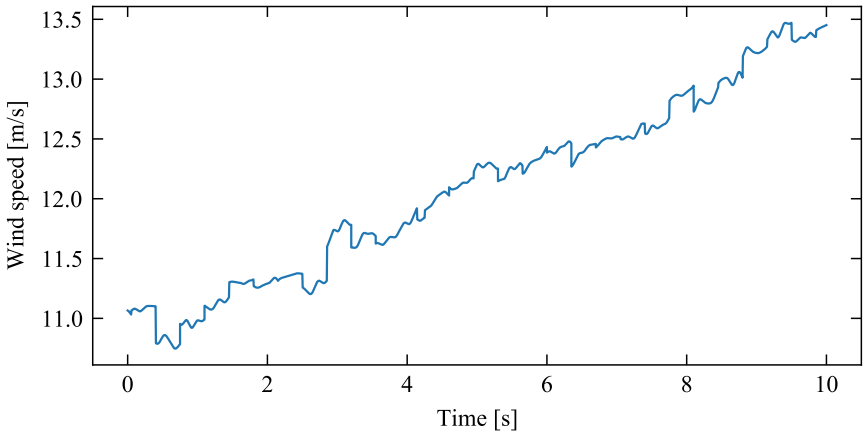

Figure 2.11: Simulation scenario: ramping wind condition

2.6.2 Simulation Results

Simulated voltage angles and injected power of selected buses are presented in Fig. 2.12. The simulation results of buses with SGs are illustrated with solid lines, and those of buses with wind turbines are displayed with dotted line and circle marks. From Fig. 2.12(b), it can be seen that power injected to Bus 1 increased from 393.6 MW to 435.73 MW, and the power generated from Bus 12 increased from 197.0 MW to 217.7 MW as wind speed ramps up. As a result, voltage angle of Bus 1 increased from 25.57° to 34.71° by 9.14°. However, voltage angle of Bus 8 with SG only increased by 6.39° from 17.14° to 23.53°. Therefore, their voltage angle sensitivities are computed to analyze their strength in detail.

Fig. 2.13 shows the distribution of angle sensitivities of selected buses. It can be seen that violin plots of Bus 1 and Bus 12 are located higher than the plots of Bus 2 and Bus 8. Violin plots indicate that buses with wind plants have much higher angle sensitivities, as explained in Section 2.3. The medians of

Bus 2 and Bus 8 were 0.141 deg/MW and 0.148 deg/MW, respectively. On the other hand, Bus 1 and Bus 12 had much higher median. Their medians were 0.424 deg/MW and 0.214 deg/MW. It can be noticed that the angle sensitivity of Bus 1, where the largest wind turbine is installed, has the highest median. Thus, we can conclude that the voltage angle of Bus 1 is the most sensitive to the increased wind power, and Bus 1 is the weakest bus in the system.

Moreover, violin plots in Fig. 2.13 suggest that angle sensitivities of strong buses are not affected by changing grid condition. Their angle sensi-

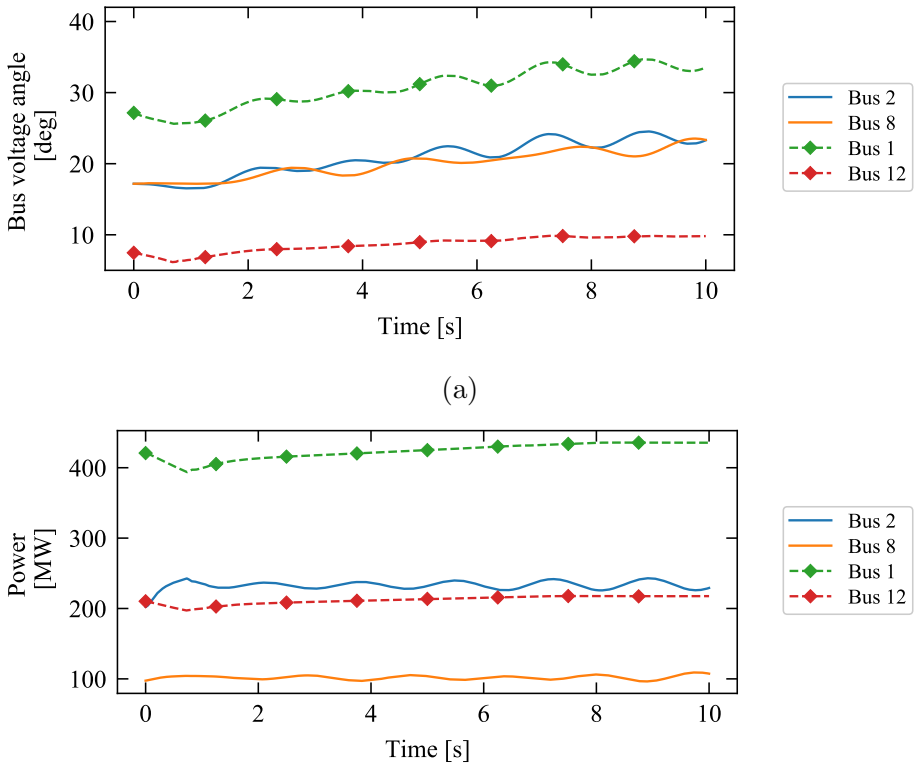

Figure 2.12: Simulation results from PSCAD/EMTDC. (a) Bus voltage angles. (b) Powers injected to buses.

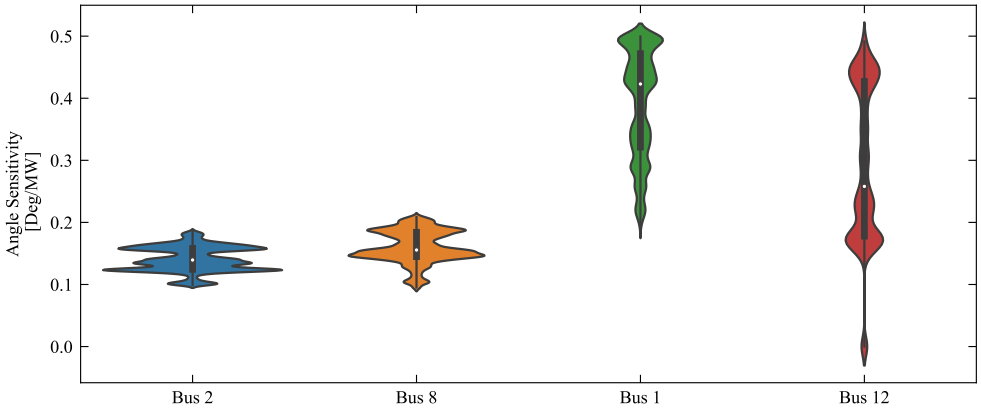

Figure 2.13: Distribution of angle sensitivities of selected buses represented with violin plots. The bout shows the probability density of data points. The median value is represented with a white dot, while its interquartile range with a gray bar.

tivities are distributed narrowly near their medians between 0.1 deg/MW and 0.2 deg/MW. On the contrary, violin plots of weak buses have longer bouts, and their angle sensitivities are mostly distributed within 0.2 deg/MW and 0.5 deg/MW. From the observation, we can infer that buses with SGs are strong and stable, but buses with wind generation are vulnerable to power change and significantly affected by wind generator ramps.

2.7 Case Studies Using Field Data

In this section, the proposed angle sensitivity metric is applied to the Panhandle region using the field data obtained from PMUs. The effectiveness of the proposed metric is demonstrated by examining angle sensitivity during different network conditions, and weak and strong parts in the Panhandle region are identified.

Table 2.3: Line Status on April 25th.

Line location	Line status
AJ Swope - Windmill	Double circuit out
Gray- Tesla	Single circuit outage recovered at 18:50

Table 2.4: The Lowest and Highest Wind Periods on April 25th.

Wind conditions	Time
Low wind period	09:30 - 10:00
High wind period	10:00 - 10:30

2.7.1 Dataset Description

A 12-hour long dataset collected on April 25th, 2019 is used to analyze the angle sensitivity of the Panhandle region. The dataset is composed of measurements from selected PMUs (See Fig.2.1 and Table 2.1). The grid conditions on April 25th are summarized in Table 2.3 and Table 2.4. On that day, there were two lines experienced outages. One of them, Tesla - Gray, returned to service at 18:50. Table 2.4 presents the high and low wind periods according to the line power flow of the line between Edith Clarke and Riley, which is one of the Panhandle interface lines. The power flowing in the line is displayed in Fig. 2.2(c).

2.7.2 Criterion for Determining Weak and Strong Buses

The concept of weak and strong buses and their relative strengths were discussed in Section 2.2 and 2.3. However, a criterion which can quantify a system's absolute strength is needed to evaluate system strength correctly. In this chapter, the angle difference limit used in a NERC transmission system [50] is used to quantify the system strength. In [50], the limit of angle

difference between two buses is set to 50° for transmission buses. Since voltage angle differences are usually between 20° and 30° during normal operation, the margin for voltage angle increase is then chosen to be 30°. The maximum possible wind power ramp was determined as 300 MW according to the power flow of Riley - Edith Clarke line presented in Fig. 2.2(c). From 09:30 to 10:30, power flowing in the line ramped up from 208 MW to 526 MW, i.e., by 318 MW. Therefore, a typical angle sensitivity during normal system condition is decided as 0.1 deg/MW (= 30 deg/300 MW) for the Panhandle region.

If angle sensitivities are higher than twice of the normal status (0.2 deg/MW), buses are considered as a weak bus. In this case, 300 MW of wind power ramp will increase voltage angle difference of 60°. An increase in voltage angle by 60° could result in voltage angle collapse as described in Section 2.3.2. Otherwise, buses are evaluated as strong if their angle sensitivities are half of the nominal value (0.05 deg/MW). These thresholds can certainly be adapted and determined more precisely based on the grid condition.

2.7.3 Case 1: Change in System Strength during Line Recovery

The effectiveness of the proposed metric is demonstrated by analyzing the change in angle sensitivity as line status changes. It is well-known that line outage weakens system strength in terms of both SCR and angle stability because of increased Thevenin equivalent impedance and reduced transmission capability [8]. On April 25$^{\text{th}}$, the tripped line between Gray and Tesla recovered at 18:50. We can assume that buses near Gray and Tesla became stronger after the line recovery because of reduced equivalent reactance, and angle sensitivity of those buses will decrease.

Fig. 2.14 shows angle sensitivity of Clear Crossing from 18:40 to 19:50

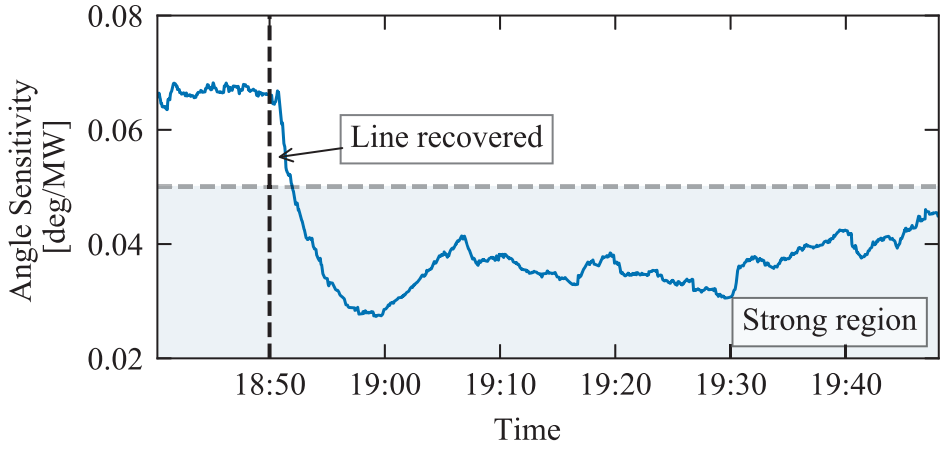

Figure 2.14: The change in angle sensitivity after line recovery at Tesla.

computed per Section 2.5. It can be seen that angle sensitivity reduced rapidly from 0.066 deg/MW to 0.028 deg/MW at 18:50 as the tripped line recovered. The angle sensitivity of Clear Crossing entered into the strong region after the line recovered, although it fluctuated between 0.028 deg/MW and 0.04 deg/MW. The result shows that line recovery strengthened the voltage angle of Clear Crossing, and the proposed metric properly reflected the change in Clear Crossing's strength.

2.7.4 Case 2: Examining System Strength during Different Wind Conditions

In the second case, strengths of lines and buses during different wind conditions are evaluated. The system strength during low and high wind periods shown in Table 2.4 are compared using the proposed angle sensitivity metric. The angle sensitivities of buses and lines observed by selected PMUs are shown in Fig. 2.15. The violin plots in the blue shade indicate the result of the high wind period, and plots in the orange shade show the result of the

low wind period.

By inspecting Fig. 2.15(a), it can be seen that angle sensitivities of the first three buses increased during the high wind period, but those of the last two buses remained constant. The median of AJ Swope rose from 0.106 deg/MW to 0.186 deg/MW, and that of Windmill increased from 0.083 deg/MW to 0.103 deg/MW. In contrast, angle sensitivities of Edith Clarke and Clear Crossing were not affected by increased wind power generation. Their medians remained the same at 0.046 deg/MW and 0.068 deg/MW even though the wind condition changed. Angle sensitivities of lines displayed in Fig. 2.15(b) show similar result. Lines on the northern side of the Panhandle region experienced a larger change in angle sensitivities. For example, median of PMU3@AJ Swope increased from 0.099 deg/MW to 0.114 deg/MW. However, medians of lines at Edith Clarke and Clear Crossing remained the same at 0.013 deg/MW and 0.021 deg/MW, respectively.

The increase in angle sensitivity was the largest at AJ Swope, which implies that strength of AJ Swope is affected the most by increased wind generation. Its maximum bus voltage angle sensitivity increased from 0.130 deg/MW to 0.213 deg/MW by 38.8%, and the line angle sensitivity increased from 0.128 deg/MW to 0.193 deg/MW by 50.8%. Angle sensitivity of AJ Swope indicates that it was not susceptible during the low wind period, but became weak as wind power output increased during the high wind period. According to (2.1) and (2.14), we can assume that AJ Swope has low inertia moment and high equivalent impedance because of its location and wind farms installed.

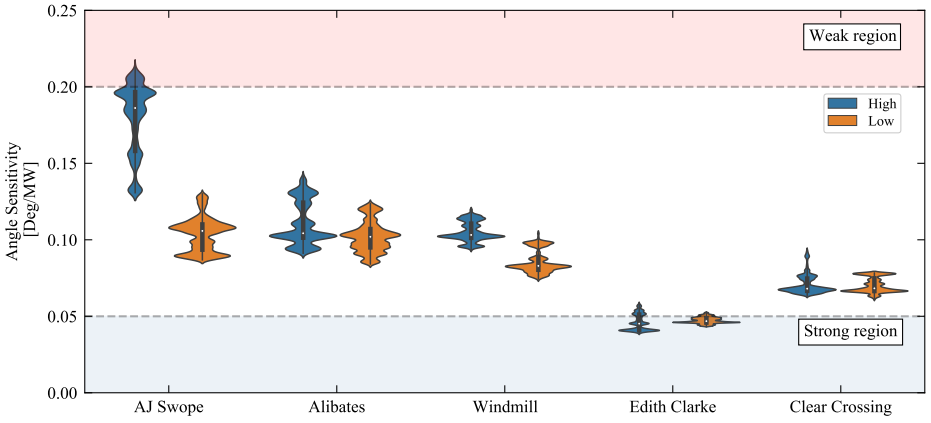

(a)

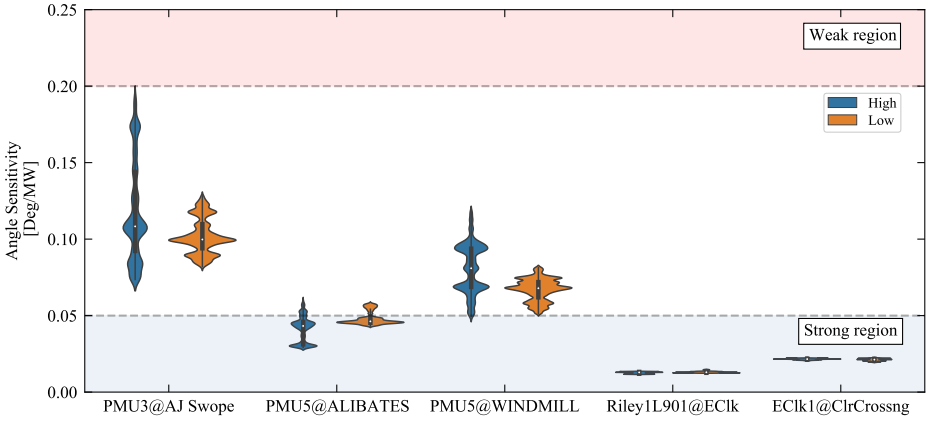

(b)

Figure 2.15: Angle sensitivities during different wind conditions. (a) Buses. (b) Lines.

2.7.5 Case 3: Evaluating System Strengths of the Panhandle Region

The strength of buses and lines observed by selected PMUs are evaluated by investigating the distribution of accumulated angle sensitivity samples. The distributions of angle sensitivities of selected buses and lines for 12 hours are shown in Fig. 2.16. From Fig. 2.16(a), we can see that AJ Swope and Al-

ibates have the highest angle sensitivity. Their medians were 0.108 deg/MW and 0.112 deg/MW, and the peak values were 0.269 deg/MW and 0.270 deg/MW, respectively. Their medians indicate that AJ Swope and Alibates were not weak throughout most of the day, but their peak angle sensitivities show that they became sensitive during unusual grid condition. For example, Case 2 showed that AJ Swope was weak during the high wind period shown in Table 2.4. We can assume that Alibates was also weak during another high wind period. On the contrary, Edith Clarke and Clear Crossing were identified as strong buses. The median of Edith Clarke was 0.048 deg/MW, which is in the strong range. The violin plot of Edith Clarke has the widest width near the median, which means its voltage angle is very stable. The median of Clear Crossing was 0.061 deg/MW, which is slightly higher to be evaluated as strong. However, as shown in Fig. 2.14, Clear Crossing also became strong after the line between Gray and Telsa came back.

The calculated angle sensitivities of chosen lines in the Panhandle are presented in Fig. 2.16(b). The line observed by PMU3@AJ Swope was the weakest line, and its peak angle sensitivity was 0.273 deg/MW. Lines observed by PMUs at Edith Clarke and Clear Crossing both had stable voltage angles during whole day. Their medians were 0.013 deg/MW and 0.021 deg/MW, respectively. By comparing Fig. 2.16(a) and (b), it can be noticed that the line observed by PMU5@ALIBATES is not as weak as the bus Alibates. It can be inferred that other lines at Alibates, such as the line connecting Alibates and Gray or AJ Swope, are sensitive to power change. Since PMU5@Alibates is measuring the line heading to the load center, it could be stronger than other lines located at the edges of the Panhandle region.

The result explains that buses and lines at the Panhandle region bound-

ary are weaker compared to the buses near the load center. As shown in (2.14), the equivalent reactance between selected buses and the reference bus at the load center affected the angle sensitivity a lot. The result is consistent with the analysis based on WSCR method, but the proposed metric was calculated using PMU measurements only.

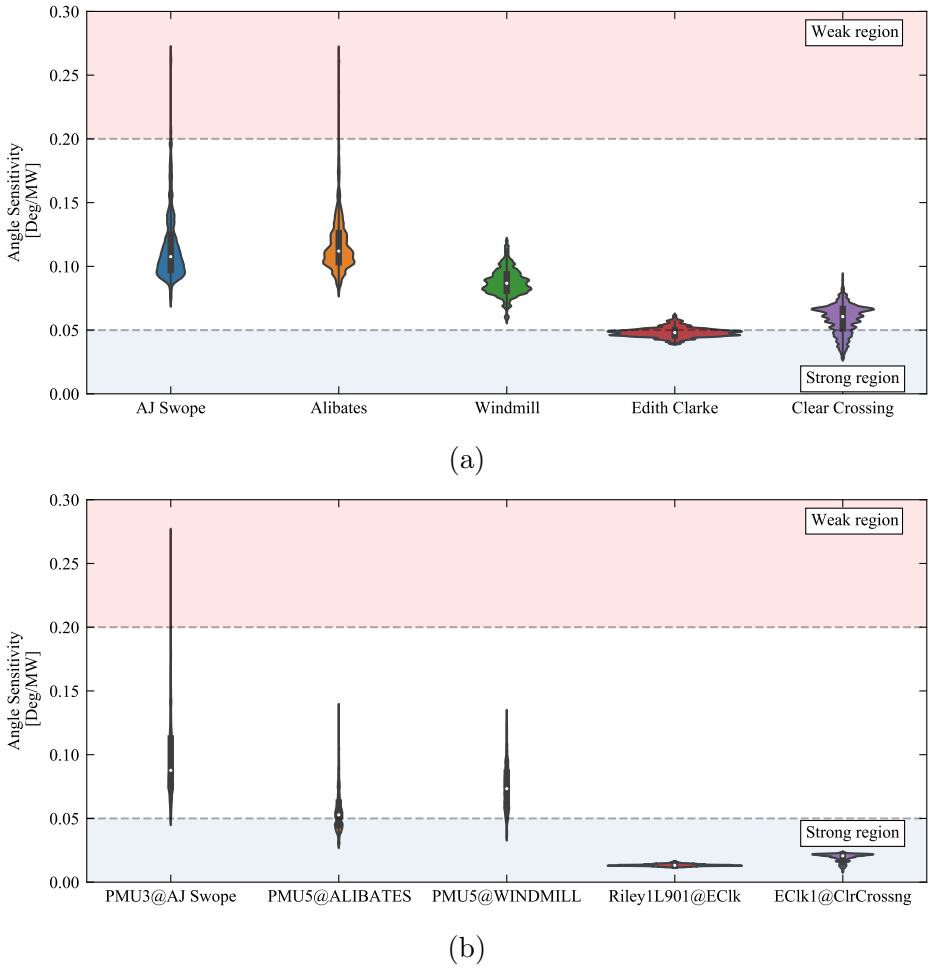

Figure 2.16: Distribution of angle sensitivity of the elements. (a) Buses. (b) Lines.

2.8 Final remarks

This chapter proposed a new method to evaluate the strength of transmission system with large scale wind projects. The proposed metric evaluates system strength by calculating voltage phase angle sensitivity to power change based on PMU data. The method can be applied without any other information about the system and to continuous data streams. Its feasibility and effectiveness are demonstrated through case studies using the PMU measurement from the Panhandle region.

Case studies confirm that the proposed method identifies weak and strong parts of the system properly. The result was consistent with previous works using an SCR method, i.e., buses at the remote region tend to be weaker than those closer to the center of the ERCOT grid. Case studies also showed that the proposed method could display the varying system strength affected by a change in grid condition, such as line recovery and varying wind power generation.

Chapter 3

Modeling and Simulation of Grid-Following and Grid-Forming Inverters and Their Steady-State Equivalent Circuits

3.1 Introduction

This chapter analyzes the modeling and simulation of grid-following and grid-forming inverters used in microgrids. Inverter models are built in PSCAD/EMTDC environment, and they can operate in both grid-following and grid-forming modes.

As addressed in Section 1.1, detailed inverter models require a large computational effort. Therefore, this chapter proposes equivalent models of grid-forming and grid-following inverters. Equivalent models are developed based on their control parameters, and a current limiting strategy is incorporated into the short-circuit analysis process. The accuracy of the steady-state short-circuit study is examined by comparing results obtained from OpenDSS and PSCAD/EMTDC.

This chapter is organized as follows. The control structures of the grid-following and grid-forming inverters are presented in Section 3.2. The steady-

Parts of the work presented in this chapter appear in the following published papers:
– **T. Kim**, N. Barry, W. Kim, S. Santoso, V. C. Cunha, W. Freitas, W. Wang, R. Dugan, D. Ramasubramanian, and A. Maitra, "Modeling and Simulation of Short-Circuit Faults in Inverter-Based Microgrids Using Steady-State Equivalent Circuits", in *IEEE Power and Energy Society General Meeting*, Denver, July 2022, *(Accepted)*.

state equivalent models of the inverters are shown in Section 3.3, and current limiting controls implemented for the steady-state solver are discussed in Section 3.4. The test system is introduced in Section 3.5, and simulation results are presented in Section 3.6. Final remarks are presented in Section 3.7.

3.2 Dynamic Model of the Inverter Operating in Grid-Following and Grid-Forming Modes

This section presents the control strategy of an inverter which can operate in both grid-forming and grid-following modes by simply changing the reference signals and controller parameters. The overall control strategy is shown in Fig. 3.1.

3.2.1 Reference Signals for Each Mode and Voltage and Current Control Loops

The inverter controller, shown in Fig. 3.1, consists of two cascaded PI controllers operating in the rotating dq-frame [20]. The outer loop generates current reference signals (I^*_{dq}) according to the control mode of the inverter. The inverter controls the active and reactive power injected into the grid when operating in a grid-following mode. Therefore, the frequency reference signal is obtained from the grid voltage using a PLL. The reference current is computed using the active and reactive power reference signals (P^* and Q^*). While in grid-forming mode, the inverter controls the voltage magnitude and frequency of the system. It does not require a PLL, and the voltage magnitude reference (V^*) and frequency reference (ω^*) are provided.

The reference signal for the inverter is generated in the rotating dq-frame. First, the outer current control loop generates current reference signals

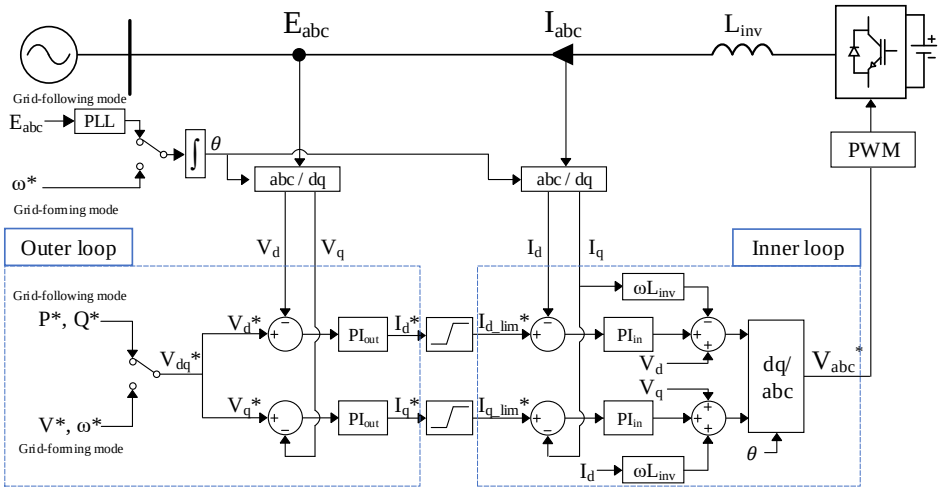

Figure 3.1: The control structure of the inverter capable of operating in both grid-forming and grid-following modes.

I_d^* and I_q^*. The difference between the voltage reference V_{dq}^* and measured voltage V_{dq} is regulated by the PI controller.

The inner loop regulates the inverter current based on the voltage relationship between the grid and inverter voltages as shown below,

$$E_d = L_{inv}\frac{dI_d}{dt} + j\omega L_{inv} I_q + V_d, \tag{3.1}$$

$$E_q = L_{inv}\frac{dI_q}{dt} + j\omega L_{inv} I_d + V_q, \tag{3.2}$$

where E_{dq} is the grid voltage in the dq-axis; L_{inv} is the equivalent reactance of the inverter; I_{dq} is the current in the dq-axis; ω is the angular frequency. The PI controller in the inner loop (PI_{in}) generates the voltage reference signal, and the voltage drop caused by L_{inv} is compensated. Characteristics of voltage and current control loops are included in the equivalent models of the inverters. The voltage and current controllers of the inverter developed in PSCAD/EMTDC are shown in Fig. 3.2 and Fig. 3.3.

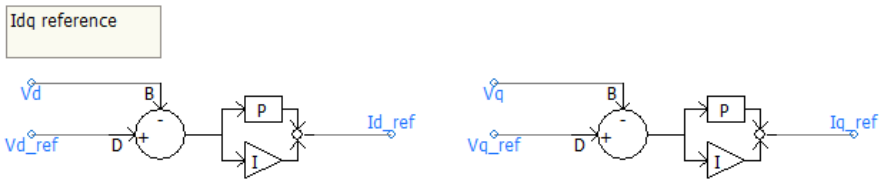

Figure 3.2: The outer current control loop of the inverter in PSCAD/EMTDC.

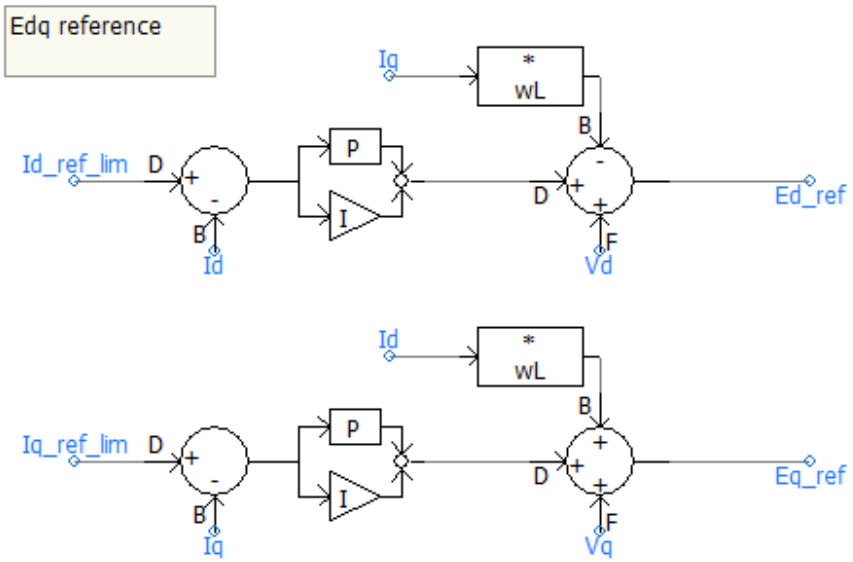

Figure 3.3: The inner voltage control loop of the inverter in PSCAD/EMTDC.

3.2.2 Current Limiting Strategy of the Inverter

A current limiting function of an inverter is important for short-circuit study of microgrids. Unlike SGs, inverters have a low thermal limit and require a current limiter to protect their switches from overcurrents. Current limiters are generally implemented in the dq-frame to limit the current reference I^*_{dq} to the current limit I_{lim}. First, the magnitude of the reference current I_{mag} is calculated as follows,

$$I_{mag} = \sqrt{I^{*2}_d + I^{*2}_q}. \tag{3.3}$$

When I_{mag} is smaller than I_{lim}, I^*_{dq} are used without modification. However, when I_{mag} is larger than I_{lim}, I^*_{dq} is adjusted by multiplying $\frac{I_{lim}}{I_{mag}}$ as below,

$$I^*_{dq\_lim} = \begin{cases} I^*_{dq,} & \text{when } I_{mag} < I_{lim}, \\ \frac{I_{lim}}{I_{mag}} I^*_{dq,} & \text{when } I_{mag} > I_{lim}. \end{cases} \tag{3.4}$$

The current limiter described in (3.4) works well during a balanced condition, but it may not perform well during an unbalanced fault condition [51]. Thus, the current limiter is modified to limit the current in the abc-frame rather than the dq-frame [52].

The current limiter implemented in the abc-frame is shown in Fig. 3.4. The dq-axis current references are transformed to the abc-frame current reference I^*_{abc}, and the current is limited based on their rms values. The current references are adjusted as follows:

$$I^*_{abc\_lim} = \begin{cases} I^*_{abc,} & \text{when } I_{rms} < I_{lim}, \\ \frac{I_{lim}}{I_{rms}} I^*_{abc,} & \text{when } I_{rms} > I_{lim}. \end{cases} \tag{3.5}$$

where $I^*_{abc\_lim}$ is the limited current reference; m is the current limiting coefficient; I_{lim} is the inverter current limit. When the inverter output current is smaller than I_{lim}, m is fixed at 1, and I^*_{abc} is used without modification. But

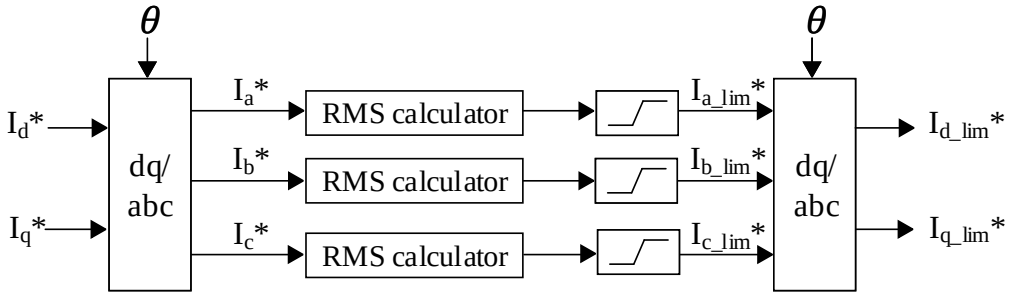

Figure 3.4: The current limiter implemented in the abc-frame for unbalanced circuits.

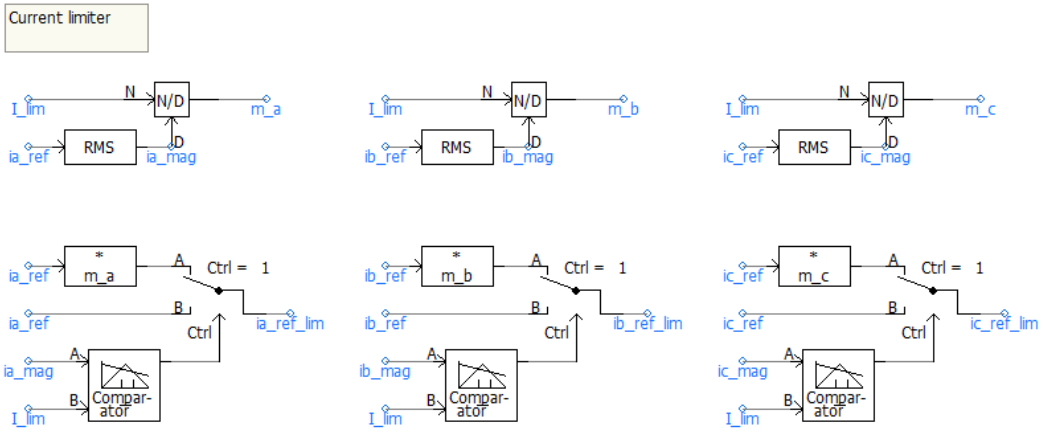

Figure 3.5: The current limiter of the inverter in PSCAD/EMTDC.

when the inverter current is larger than I_{lim}, m is adjusted to limit the inverter current to I_{lim}. The current limiting control of grid-forming and grid-following inverters are also included in the steady-state equivalent models.

3.3 Steady-State Equivalent Models of Inverters for Short-Circuit Studies

This section proposes steady-state equivalent models of inverters based on the controller introduced in Section 3.2. The grid-forming inverter is modeled as a voltage source with equivalent impedance developed in [26], while the grid-following inverter is represented as a current source which operates based on a complex power reference.

3.3.1 Steady-State Equivalent Model of the Grid-Forming Inverters

The grid-forming inverter is represented as a voltage source with positive- and negative-sequence impedances as shown in Fig. 3.6. During

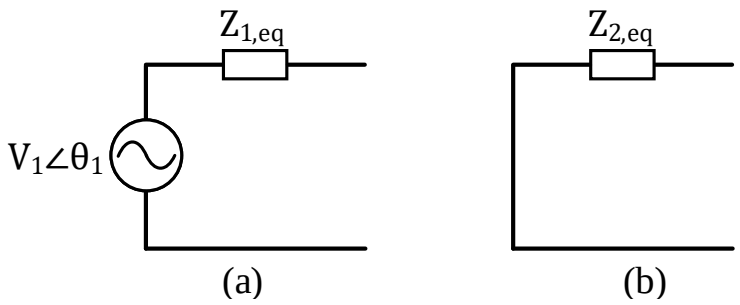

Figure 3.6: Steady-state equivalent model of the grid-forming inverter. (a) Positive-sequence circuit. (b) Negative-sequence circuit.

islanded operation, V_1 is set to the rated voltage of the system, and θ_1 is decided as 0° to act as a reference voltage angle. Since we use a three-phase three-leg inverter, its zero-sequence network is not considered. In [26], a virtual admittance was implemented in the outer control loop to improve the stability while operating in grid-forming mode [53]. In this work, it was replaced with a PI controller (PI_{out}), which helps the inverter to operate in both grid-forming and grid-following modes [20].

The equivalent positive- and negative-sequence impedances, $Z_{1,eq}$ and $Z_{2,eq}$, are calculated based on the inverter controller and filter impedance. They remain constant during normal operation but vary when the current limiter is activated. The equivalent impedances of the PI controller Z_{PI}, current limiter M, and filter impedance Z_f could be written in matrix form as follows [26],

$$Z_{PI} = \begin{bmatrix} k_p + \frac{1}{sT_i} & 0 \\ 0 & k_p + \frac{1}{sT_i} \end{bmatrix}, \tag{3.6}$$

$$M = \begin{bmatrix} m & 0 \\ 0 & m \end{bmatrix}, \tag{3.7}$$

$$Z_f = \begin{bmatrix} R_f + sL_f & 0 \\ 0 & R_f + sL_f \end{bmatrix}. \tag{3.8}$$

where k_p and T_i are the gains of the PI controller; m is current limiting coefficient; R_f and L_f are the filter resistance and inductance, respectively.

Using matrices (3.6) - (3.8), the voltage equation shown in (3.1) could be written in matrix form as below,

$$\begin{bmatrix} E_d \\ E_q \end{bmatrix} = \begin{bmatrix} V_d \\ V_q \end{bmatrix} + \underbrace{\begin{bmatrix} -k_{p,in} - \frac{1}{sT_{i,in}} & -\omega L_f \\ \omega L_f & -k_{p,in} - \frac{1}{sT_{i,in}} \end{bmatrix}}_{Z_\gamma} \begin{bmatrix} I_d \\ I_q \end{bmatrix} + Z_{PI,in} \begin{bmatrix} I^*_{d,lim} \\ I^*_{q,lim} \end{bmatrix}. \quad (3.9)$$

where $k_{p,in}$ and $T_{i,in}$ are gains of the inner PI control loop. By including the matrices of the current limiter M, the outer PI control loop $Z_{PI,out}$, and the filter impedance Z_f to (3.9), we can obtain the formula of the inverter controller as follows,

$$\begin{bmatrix} E_d \\ E_q \end{bmatrix} = \begin{bmatrix} V_d \\ V_q \end{bmatrix} + \underbrace{(Z_{PI,in} \cdot M \cdot Z_{PI,out})^{-1}(Z_f - Z_\gamma)}_{Z^{eq}_{dq}} \begin{bmatrix} I_d \\ I_q \end{bmatrix}, \quad (3.10)$$

where Z^{eq}_{dq} is the equivalent impedance of the voltage and current controller in the s-domain.

By transforming s to $j\omega$ and simplifying the matrix operations, we obtain the positive- and negative-sequence impedance as shown below.

$$Z_{1,eq}(j\omega) = \frac{R_f + k_{p,in} + \frac{1}{j\omega T_{i,in}}}{m(k_{p,in} + \frac{1}{j\omega T_{i,in}})(k_{p,out} + \frac{1}{j\omega T_{i,out}})}, \quad (3.11)$$

$$Z_{2,eq}(j\omega) = \frac{R_f + j2\omega L_f + k_{p,in} + \frac{1}{j\omega T_{i,in}}}{m(k_{p,in} + \frac{1}{j\omega T_{i,in}})(k_{p,out} + \frac{1}{j\omega T_{i,out}})}. \quad (3.12)$$

where $k_{p,out}$ and $T_{i,out}$ are gains of the outer PI control loop. Equations (3.11) and (3.12) show that the equivalent impedance of the grid-forming inverter has a close relationship with gains of PI controllers and filter impedance when the

current limiter is not activated ($m = 1$). During a fault, m becomes important, and $Z_{1,eq}$ and $Z_{2,eq}$ vary according to the fault impedance. The iterative process of calculating m is presented in the next section.

3.3.2 Steady-State Equivalent Model of the Grid-Following Inverter

The grid-following inverter is modeled as a three-phase current source as shown in Fig. 3.7. The initial set points for the current magnitude I_{mag} and angle θ_{pf} are calculated using reference powers P^* and Q^* as below,

$$I_{mag} = \frac{\sqrt{(P^*)^2 + (Q^*)^2}}{\sqrt{3} \cdot V_{FL}}, \tag{3.13}$$

$$\theta_{pf} = -\tan^{-1}\left(\frac{Q^*}{P^*}\right). \tag{3.14}$$

In (3.13), V_{FL} is the voltage of the node with fault where the grid-following inverter is installed. It is assumed to be 1 pu during normal operation. During short-circuit studies, V_{FL} is computed using OpenDSS, and I_{mag} and θ_{pf} are updated using the new V_{FL}. The fault current injected by the grid-following inverter is regulated by limiting I_{mag}.

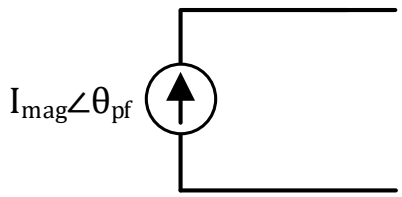

Figure 3.7: Steady-state equivalent model of the grid-following inverter.

3.4 Current Limiting Control of Multiple Inverters Operating in Different Modes

This section describes the current limiting process for the system with multiple inverters operating in different modes. We assume that one inverter operates in grid-forming mode, and the rest of the inverters operate in grid-following mode. The iterative method shown in Fig. 3.8 is used to determine the current limiting coefficient m for the grid-forming inverter and the current magnitude references for the grid-following inverters. In summary, the current magnitude references I^i_{mag} for all i-th grid-following inverters are determined first, and m is decided later considering the output of grid-following inverters. Details of each step are explained below:

1. **Calculate initial inputs:** The short-circuit study starts by calculating the initial inputs for the equivalent models of the grid-forming and grid-following inverters. The initial value of m and V^i_{FL} are assumed as 1 and 1 pu, respectively, which means there is no fault, and the current limiter is not activated. $Z_{1,eq}$ and $Z_{2,eq}$ for the grid-forming inverter and I^i_{mag} and θ^i_{pf} for all i-th grid-following inverters are computed.

2. **Current limiting of grid-following inverters:** The output currents of grid-following inverters are calculated first. I^i_{mag} is updated using V^i_{FL} obtained from OpenDSS and (3.13). If the updated I^i_{mag} is larger than the current limit of the i-th grid-following inverter $I^i_{lim,FL}$, the inverter current is limited to $I^i_{lim,FL}$ and exit the loop. Otherwise, we compare the reference complex power S^{i*} to the power obtained from OpenDSS (S^i_{FL}) because an updated I^i_{mag} causes a change in V^i_{FL}. The iterative process is repeated until S^i_{FL} is the same as S^{i*}, and then repeated for all grid-following inverters in the system.

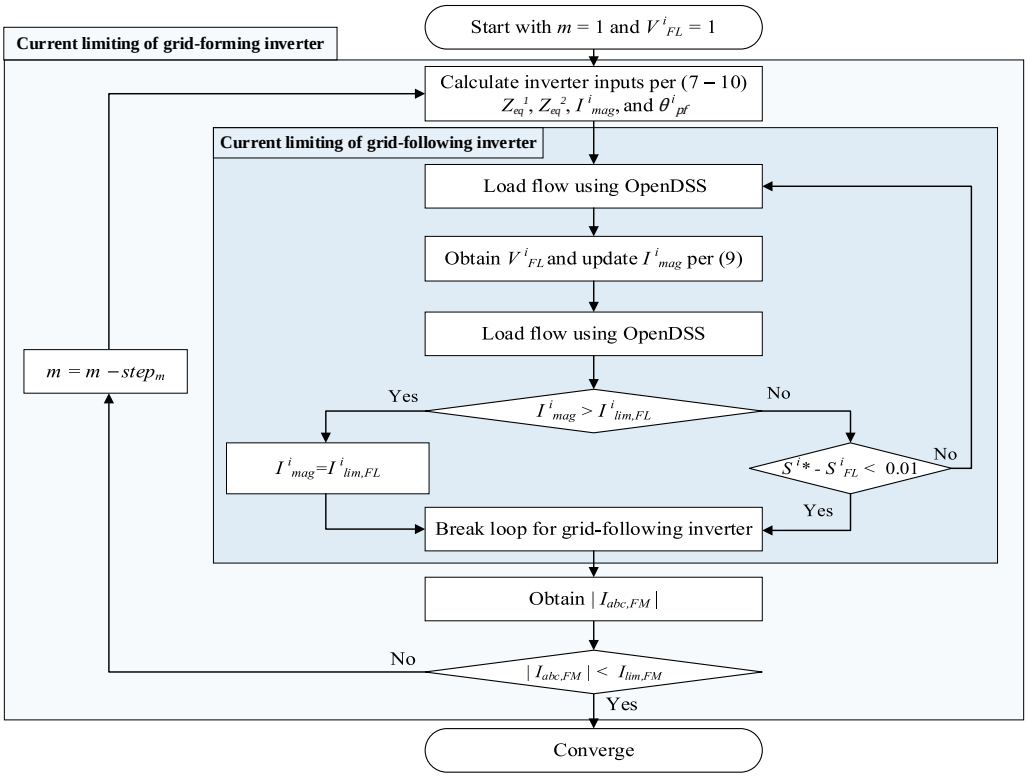

Figure 3.8: Flow chart for short-circuit study of microgrid with multiple inverters.

3. **Current limiting of grid-forming inverter:** The output current of the grid-forming inverter $I_{abc,FM}$ is controlled by adjusting the value of m. As shown in (3.11) and (3.12), reducing m increases the equivalent impedances and results in a lower fault current. If $I_{abc,FM}$ is smaller than the current limit of the grid-forming inverter $I_{lim,FM}$, the iteration process ends without adjusting m. When $I_{abc,FM}$ is larger than $I_{lim,FM}$, the iterative process is executed. m is adjusted by subtracting $step_m$ from m until $I_{abc,FM}$ is smaller than $I_{lim,FM}$. In this work, $step_m$ is set at 0.001. The equivalent impedances are calculated with the updated m, and the output currents of the grid-following inverters are also updated until the outputs of all inverters are below their current limits.

3.5 Test System and Simulation Scenario

3.5.1 Modified IEEE-34 Node Test Feeder with Inverters

The proposed steady-state equivalent models are tested on the modified IEEE 34-node test feeder shown in Fig. 3.9. The test system is islanded from

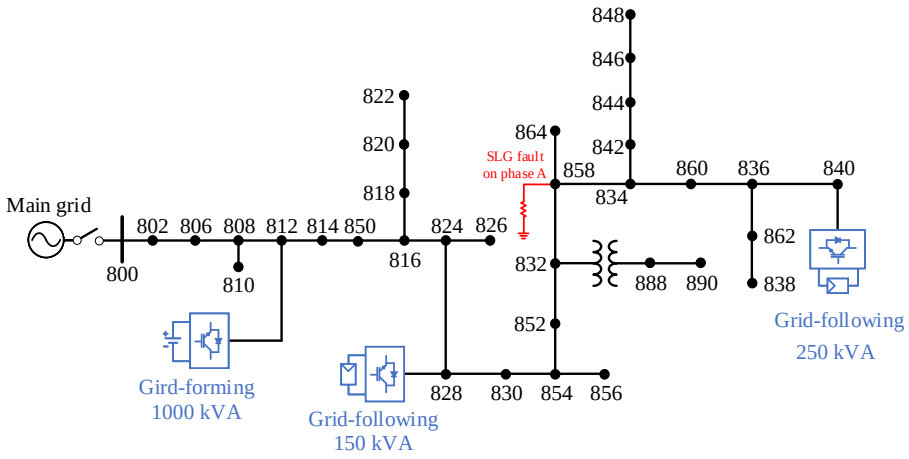

Figure 3.9: The modified IEEE 34-node test system with inverters.

the main grid at Bus 800 and supplied by one grid-forming inverter and two grid-following inverters. The locations, rated values, and reference signals for all inverters are shown in Table 3.1. The grid-forming inverter at Bus 812 controls the grid frequency and voltage. Grid-following inverters at Bus 840 and Bus 828 have different capacities and active power set points. Current limits for all inverters are set to 1.2 times the rated current. The parameters of the grid-forming inverters and the calculated equivalent impedances for normal operation are presented in Table 3.2. It can be seen that the negative-sequence impedance has negative resistance, but it is only for simulation purpose, not a physical element.

3.5.2 Simulation Scenario

A single line-to-ground (SLG) fault of 1 mΩ is applied at phase A of Bus 858. Short-circuit node voltages and line currents are calculated using the equivalent models and current limiting process introduced in Section 3.4. The load flow is solved using the steady-state software OpenDSS, and the current limiting procedure is implemented using Python. The accuracy

Table 3.1: Inverters in the System and Their Rated Values.

Control mode	Location	Rated capacity [kVA]	Rated voltage [kV]	Reference signals	Current limit [A]
Grid-forming	Bus 812	1000	0.6	60 Hz 0.6 kV	1154.73
Grid-following	Bus 840	250	0.6	200 KW 0 kvar	288.67
Grid-following	Bus 828	150	0.6	100 KW 0 kvar	173.21

Table 3.2: Parameters of the Grid-Forming Inverter.

Parameter	Value	Parameter	Value
R_f	2 mΩ	L_f	1 mH
$k_{p,out}$	1.2	$T_{i,out}$	0.001
$k_{p,in}$	1.3	$T_{i,in}$	0.0075
$Z_{1,eq}$	0.142 + j 0.313 Ω		
$Z_{2,eq}$	-0.048 + j 0.344 Ω		

of the proposed steady-state models is validated by comparing the results obtained from the steady-state simulation to those computed from EMT software PSCAD/EMTDC.

3.6 Simulation Results

The short-circuit node voltages and line currents were computed using both steady-state and EMT software. The voltages and currents from both software are compared in Fig. 3.10. The results from OpenDSS (V_{ss} and I_{ss}) are presented with solid lines with X markers, and those from PSCAD/EMTDC (V_{emt} and I_{emt}) are illustrated with a dotted line with circle markers. Fig. 3.10(a) shows the node voltage in per-unit, and Fig. 3.10(b) illustrates currents flowing in 24.9 kV lines.

First, the output currents of inverters are investigated. After applying an SLG fault, output currents of both grid-following inverters reached their limit because of voltage drop on phase A. Their output currents were set to their maximum current shown in Table 3.1, 288.67 A and 173.21 A, respectively. In contrast, the output current of the grid-forming inverter did not reach the limit, so m remained at 1. Thus, $Z_{1,eq}$ and $Z_{2,eq}$ shown in Table 3.2 were

used without modification.

Fig. 3.10 shows that voltages and currents from both software match well. The largest mismatch was 2.49 % observed at phase B of Bus 814. The voltage calculated with the proposed steady-state model was 1.165 pu, while the voltage from the time-domain simulation was 1.136 pu. The voltage increased higher than 1 pu because phase B was a healthy phase without fault.

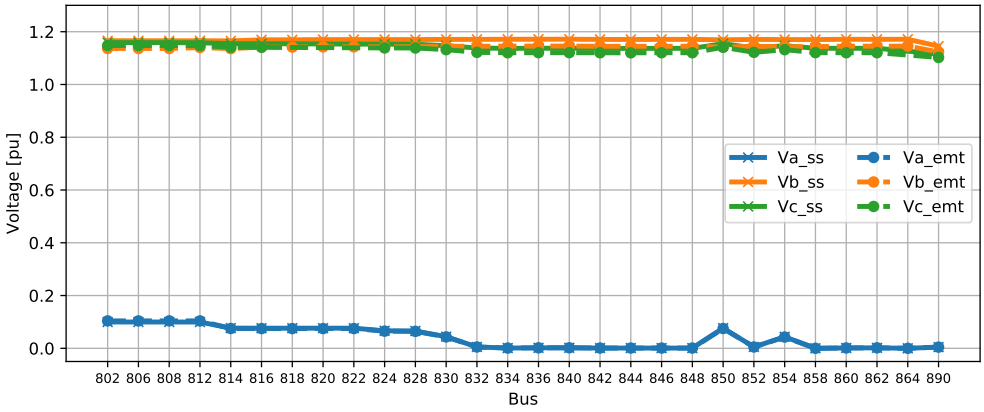

(a)

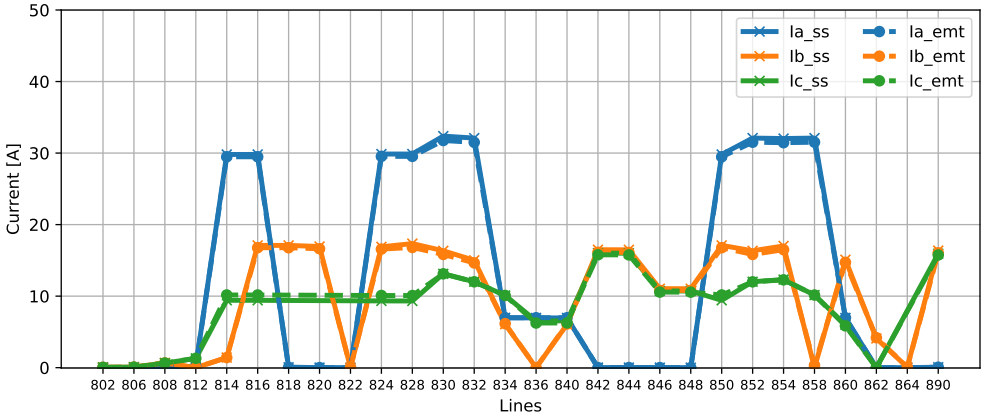

(b)

Figure 3.10: Simulations results from OpenDSS and PSCAD/EMTDC. Short-circuit (a) node voltages. (b) line currents.

Otherwise, errors were below 2.3% for all nodes. The results show that the proposed equivalent model and current limiting control proposed in Fig. 3.8 can precisely reproduce the response of the detailed model presented in Fig. 3.1 and 3.4. The proposed equivalent models had good accuracy and were able to reproduce the result from EMT software with less computational effort.

3.7 Final Remarks

This chapter presents a short-circuit analysis of inverter-based microgrid using steady-state equivalent models of grid-forming and grid-following inverters. The equivalent models of grid-forming and grid-following inverters and their current limiting strategy used in the steady-state solver were developed. The grid-forming inverter was modeled as a voltage source with equivalent impedances calculated based on the inverter control parameters. The grid-following inverter was represented with a current source, and operated based on the active and reactive power set points. The performance of the equivalent model was validated by comparing post-fault voltages and current in the IEEE 34-node test system. Simulation results showed that the proposed equivalent models perform well without losing accuracy and reduce computational efforts.

Chapter 4

Blackstart Operation of a Stand-Alone Microgrid Using Grid-Forming Inverter with Voltage Balancing Capability

4.1 Introduction

This chapter presents the blackstart operation of an islanded microgrid using a grid-forming inverter. Inverter described in Chapter. 3 performs well on a balanced three-phase systems, but its performance deteriorates when the system has an unbalanced configuration, which can be seen in most of the distribution networks. This chapter presents the model of an inverter that controls the negative-sequence component of voltage to mitigate voltage imbalance.

The inverter's performance is evaluated by blackstarting a stand-alone microgrid with an unbalanced load and an induction motor. The inverter's voltage balancing function is evaluated by analyzing the steady-state voltage after energizing unbalanced loads, and current limiting control is demonstrated by supplying a large amount of reactive power while starting the motor.

This chapter is organized as follows. The control structure of the grid-forming inverter is presented in Section 4.2. The implementation of current

---

Parts of the work presented in this chapter appear in the following published papers:
– **T. Kim**, V. C. Cunha, S. Santoso, W. Wang, R. Dugan, D. Ramasubramanian, and A. Maitra, "Blackstart of Unbalanced Microgrids Using Grid-Forming Inverter with Voltage Balancing Capability", in *2022 IEEE Transmission and Distribution Conference and Exposition*, New Orleans, April 2022, *(Accepted)*.

limiter that performs better in unbalanced circuits is shown in Section 4.3. The test system is introduced in Section 4.4, and simulation results are presented in Section 4.5. Final remarks are presented in Section 4.6.

4.2 Control of Grid-Forming Inverters with Voltage Balancing Capability

This section presents the control strategy of grid-forming inverter with voltage balancing capability. The inverter controls sequence components of grid voltage to maintain balanced voltage. Since we use a three-phase three-leg inverter that does not have a ground connection, a zero-sequence controller is unnecessary.

The overall control structure of the sequence-based controller is shown in Fig. 4.1 [36]. Throughout the paper, the voltage and current notations with a subscript 1 (e.g., V_1 or I_1) denote the positive-sequence components, while those with a subscript 2 denote the negative-sequence components. The positive-sequence controller (in blue) controls the magnitude and frequency of the positive-sequence voltage $V_{1,dq}$, where V_{dq} is the grid voltage in the rotating direct-quadrature (dq) frame. The rated voltage (V^*) and frequency (ω^*) are reference signals for the positive-sequence controller. Otherwise, the negative-sequence controller (in red) controls the negative-sequence voltage $V_{2,dq}$ at a negligible level to maintain balanced voltage. Frequency reference $-\omega^*$ is given to obtain the negative-sequence components of voltage and current in the dq-frame. The negative-sequence voltage reference is set to zero volt to remove the negative-sequence voltage.

The inverter controls the grid voltage in the rotating dq-frame. When the grid voltage is balanced, its dq components V_{dq} consists of constant sig-

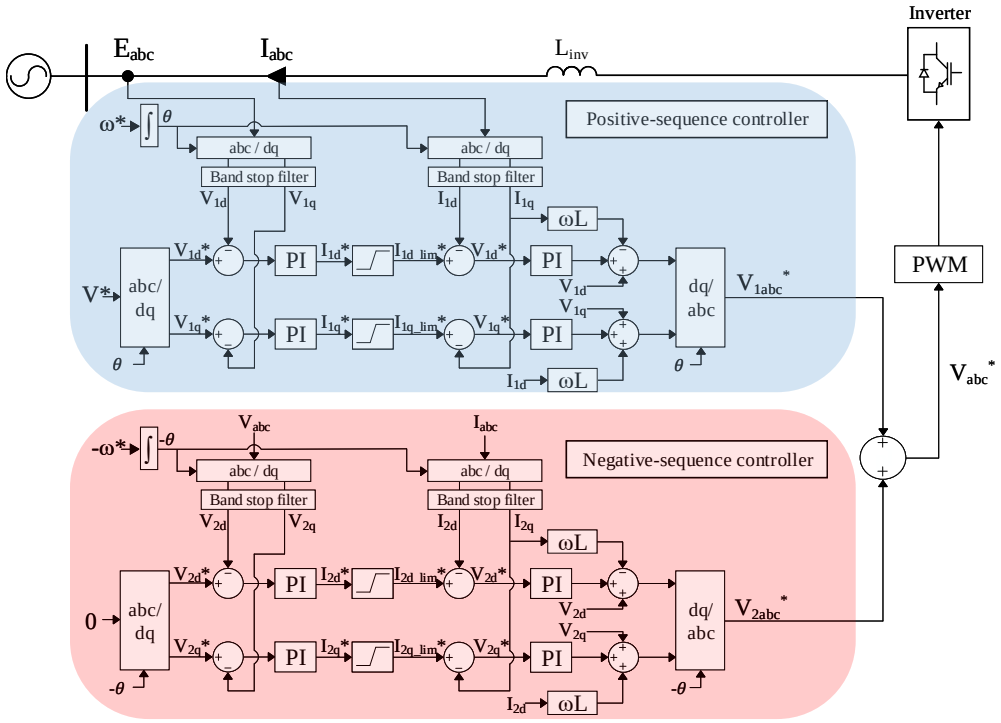

Figure 4.1: Sequence-based controller of grid-forming inverter for unbalanced circuit.

nals. However, as the grid voltage becomes unbalanced, dq components include oscillatory terms with a frequency of 2ω as shown below,

$$\begin{bmatrix} V_d \\ V_q \end{bmatrix} = \frac{2}{3}[T_{dq}] \begin{bmatrix} V_a \\ V_b \\ V_c \end{bmatrix} = \begin{bmatrix} V_{d,DC} + M_d \cos(2\omega t + \theta_d) \\ V_{q,DC} + M_q \cos(2\omega t + \theta_q) \end{bmatrix}, \tag{4.1}$$

$$[T_{dq}] = \begin{bmatrix} \cos\theta & \cos\left(\theta - \frac{2\pi}{3}\right) & \cos\left(\theta + \frac{2\pi}{3}\right) \\ \sin\theta & \sin\left(\theta - \frac{2\pi}{3}\right) & \sin\left(\theta + \frac{2\pi}{3}\right) \end{bmatrix}, \tag{4.2}$$

where V_{abc} are grid voltage in the abc-frame; $V_{dq,DC}$ are DC components of voltage in the dq-frame; M_{dq} are magnitudes of oscillatory terms; $[T_{dq}]$ is Park's transforming matrix without a zero-sequence component. Because of the oscillation, PI controllers' output could not converge, and the controller cannot

regulate the voltage precisely. Therefore, band-stop filters are added to remove the oscillatory terms of dq components [54].

The sequence components of inverter voltage and current could be written as below.

$$V_{dq} = e^{j\omega t} V_{1,dq} + e^{-j\omega t} V_{2,dq}, \tag{4.3}$$

$$I_{dq} = e^{j\omega t} I_{1,dq} + e^{-j\omega t} I_{2,dq}. \tag{4.4}$$

The voltage and current control are achieved by employing two cascaded PI controllers based on the voltage equation between the grid and inverter. The voltage relationship between the grid voltage U_{dq} and inverter voltage V_{dq} could be written as,

$$E_{dq} = V_{dq} + L_{inv} \frac{dI_{dq}}{dt}, \tag{4.5}$$

where L_{inv} is the equivalent inductance of the inverter. By substituting (4.3) and (4.4) to (4.5), equations for positive- and negative-sequence voltage could be obtained.

$$E_{1,dq} = L_{inv} \frac{dI_{1,dq}}{dt} + j\omega L_{inv} I_{1,dq} + V_{1,dq}, \tag{4.6}$$

$$E_{2,dq} = L_{inv} \frac{dI_{2,dq}}{dt} + j\omega L_{inv} I_{2,dq} + V_{2,dq}. \tag{4.7}$$

It can be seen that (4.6) and (4.7) are decoupled. Therefore, we could control positive- and negative-sequence voltages separately with different control targets. At last, the sequence components of voltage reference $E_{1,dq}$ and $E_{2,dq}$ are merged and transformed back to E_{abc} using the inverse of $[T_{dq}]$ shown in (4.2). The voltage and current control loop developed in PSCAD/EMTDC are presented in Fig. 4.2.

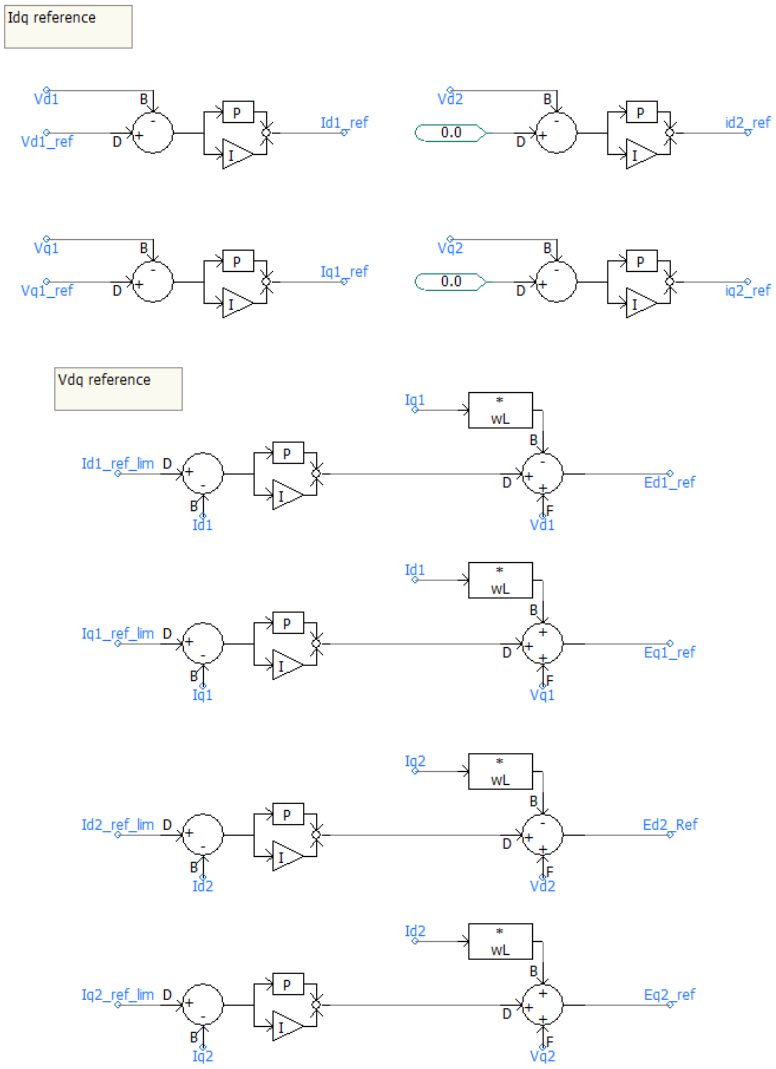

Figure 4.2: The current and voltage control loop of the inverter in PSCAD/EMTDC

4.3 Current Limiter Implemented in the ABC-Frame for Unbalanced Currents

Current limiter for inverters used in balanced circuit which control positive-sequence components was presented in Section 3.2. It works well in a balanced condition, but it may not perform well during an unbalanced fault condition [51]. Since the inverter used in this chapter controls both positive- and negative-sequence current, the reference current signal has to be modified to include both sequence components of the inverter current.

The current limiter implemented in the abc-frame is shown in Fig. 4.3. The positive- and negative-sequence components of dq-axis current references are added and transformed to the abc-frame current reference I^*_{abc}. The inverter output current is limited based on their rms values. The current references are adjusted as follows:

$$I^*_{abc\_lim} = \begin{cases} I^*_{abc,} & \text{when } I_{rms} < I_{lim}, \\ \frac{I_{lim}}{I_{rms}} I^*_{abc,} & \text{when } I_{rms} > I_{lim}. \end{cases} \tag{4.8}$$

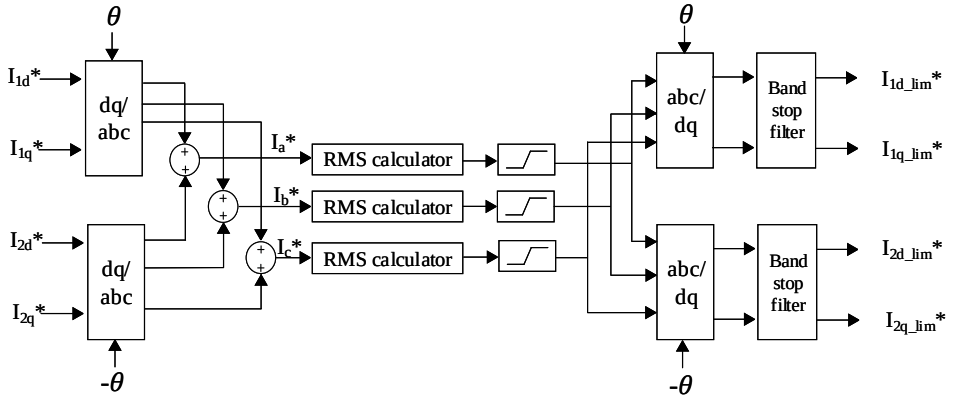

Figure 4.3: Current limiter that limits the current in the abc-frame.

In (4.8), $\frac{I_{lim}}{I_{rms}}$ is multiplied to I^*_{abc} when their rms values are larger than I_{lim}. The limited current reference signal $I^*_{abc\_lim}$ in the abc-frame is transformed back to the positive- and negative-sequence current reference $I^*_{1dq\_lim}$ and $I^*_{2dq\_lim}$ in the dq-frame. Band-stop filters are added to remove the oscillatory terms as explained in (4.1).

The advantage of having a current limiter operating in the abc-frame is demonstrated by comparing fault currents during a single line-to-ground (SLG) fault. The SLG fault is applied at 4 seconds on phase A at Bus 2, the wye side of the feeder transformer (see Fig. 4.5). The fault currents limited by current limiters implemented in dq-frame and abc-frame are presented in Fig. 4.4(a) and (b), respectively. Solid lines show the rms value of currents flowing in each phase, and the shaded curves show the instantaneous currents. The red dotted line indicates the current limit, which is 1.2 times of the rated current.

It can be seen that the current shown in Fig. 4.4(a) with the current limiter performing in the dq-domain is not limited successfully. The magnitude of phase A current presented in the blue curve was 1.41 pu. Although the peak values of instantaneous currents were limited at 1.2 pu, their waveforms are distorted and resulted in a higher rms value.

In contrast, the fault currents shown in Fig. 4.4(b) with the current limiter operating in the abc-frame are limited well in all phases. It can be seen that currents in phase A and B reached their limit because of the delta-wye configuration of the feeder transformer. Although the limiter needed 2 cycles to calculate the rms values, the fault currents are reduced effectively below the limit. Moreover, the waveforms of instantaneous currents are not distorted because the current limiter operates in the abc-frame and it has a band-stop filter removing the oscillating terms. During the blackstart, the transformer

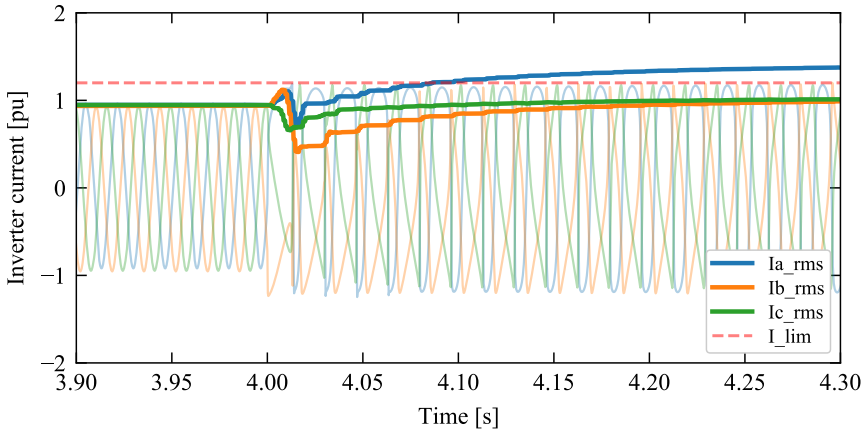

(a)

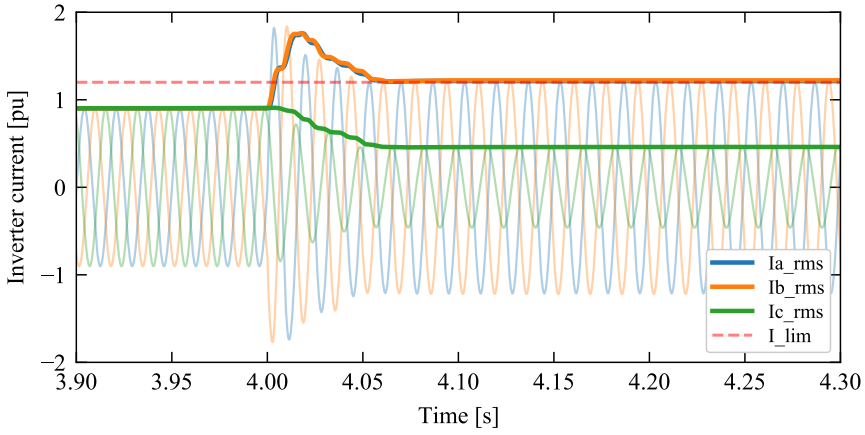

(b)

Figure 4.4: Performance of current limiters during unbalanced faults: current limiter operating in the (a) dq-frame (b) abc-frame.

inrush current and the current consumed by the motor while starting has to be limited. Therefore, we use a current limiter operating in the abc-frame to limit the unbalanced currents.

4.4 Test System and Simulation Scenario

4.4.1 Test System: Islanded Distribution Microgrid

The test system shown in Fig. 4.5 is an islanded microgrid with an unbalanced configuration. The grid-forming inverter located at Bus 1 controls the grid voltage and supplies power to the loads. The test system is composed of a grid-forming inverter, balanced and unbalanced three-phase loads, a single-phase load, and a three-phase induction motor. The rated size and power factor of the loads are summarized in Table. 4.1. Three-phase components are illustrated with black lines, and single-phase elements are displayed in blue.

4.4.2 Simulation Scenario

The blackstart operation of a stand-alone microgrid is simulated using the grid-forming inverter developed in PSCAD/EMTDC software. The grid-forming inverter aims to control the voltage balanced at 1 pu, and limit its

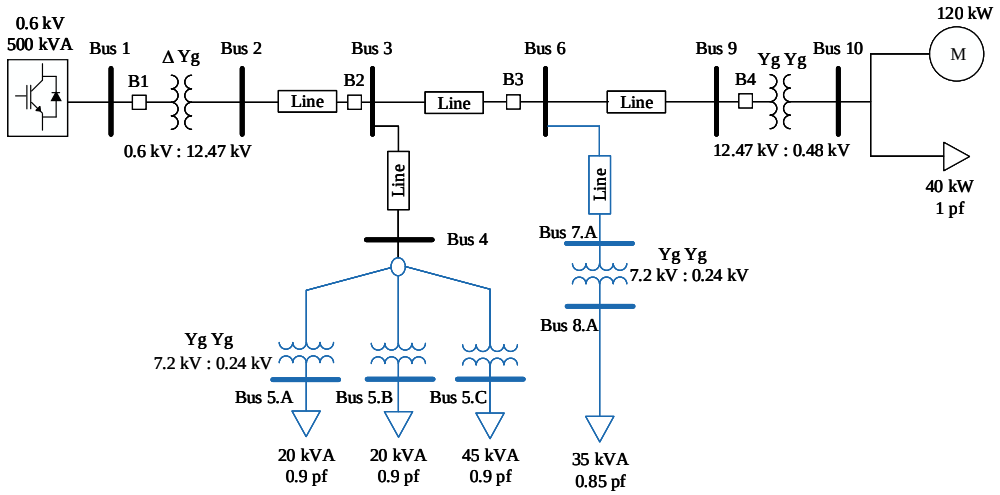

Figure 4.5: Test circuit: Unbalanced microgrid with a motor load.

Table 4.1: Loads installed in the test system

Load	Location	Phase	Size [kVA]	Power factor
Unbalanced load	Bus 5	3	A: 20 B: 20 C: 45	A: 0.9 B: 0.9 C: 0.9
Single-phase load	Bus 7	1	A: 35	A:0.85
Balanced load	Bus 10	3	13.33/ph	1
Induction motor	Bus 10	3	120	-

output current. During the blackstart, each component is energized sequentially, as shown below.

- t = 0s: Start the grid-forming inverter.
- t = 2s: Close B1, connect the delta-wye grounded (Yg) transformer at Bus 1.
- t = 5s: Close B2, energize three Yg-Yg transformers and unbalanced three-phase load at Bus 4 and 5.
- t = 8s: Close B3, energize the Yg-Yg transformer and single-phase load at bus 7 and 8.
- t = 11s: Close B4, connect the Yg-Yg transformer at Bus 9, energize the three-phase balanced load, and start accelerating the motor without a load applied.
- t = 17s: Apply full load to the motor.

4.5 Simulation Results

The simulation result of a blackstart using the grid-forming inverter is presented in this section. The output voltage and current of the inverter are analyzed to evaluate the blackstarting capability of the inverter.

4.5.1 Grid Voltage and Inverter Current During the Blackstart

The grid voltage and inverter output current during the blackstarting are investigated. The simulated voltage and current measured at the inverter side (Bus1) are presented in Fig. 4.6, and the motor speed is displayed in Fig. 4.7. Although there were transient voltages when new transformers and loads connect, Fig. 4.6(a) shows that the grid voltage was controlled at 1 pu at the steady-state after all loads are energized. There was a voltage sag from t = 11 to 13.5 seconds while the inverter was supplying reactive power to accelerate the motor. But according to IEEE Standard 3002.7 [55], voltage sag of 0.8 pu is acceptable during the motor start process. The grid voltage dropped to 0.78 pu at the beginning of the motor start, but it recovered to 0.8 pu within 0.8 seconds.

The inverter output current shown in Fig. 4.6(b) indicates that the inverter current was maintained below the current limit (1.2 pu). The inrush currents of transformers were smaller than the limit, and the large current supplied to the motor was limited well by the current limiter. Fig. 4.7 shows that the motor was accelerated from t = 11 seconds and reached its rated speed at t = 13.5 seconds. The motor maintained its speed at 0.98 pu after the full load was applied to the motor.

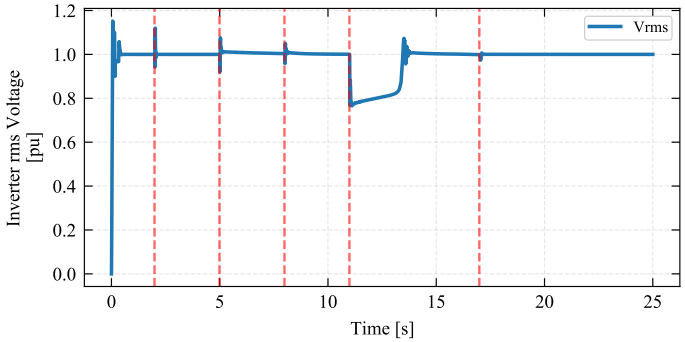

(a)

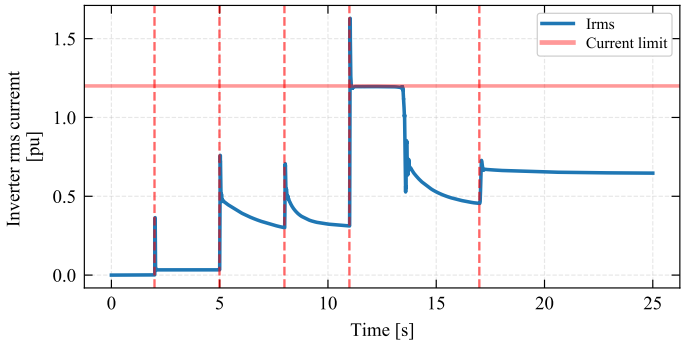

(b)

Figure 4.6: The rms value of the inverter (a) voltage (b) current.

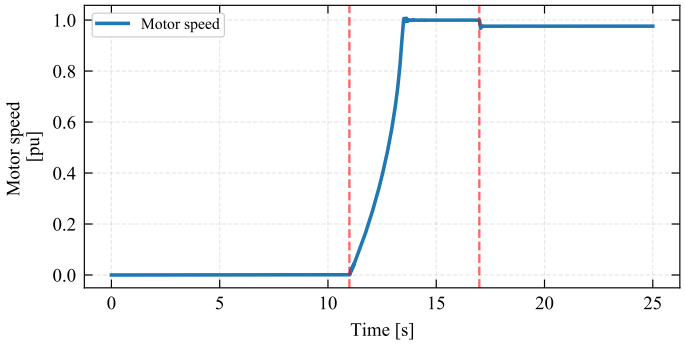

Figure 4.7: The motor speepd during the blackstart.

4.5.2 Voltage Balancing Capability of the Grid-Forming Inverter

The voltage balancing capability of the grid-forming inverter is evaluated in this section. The sequence components of the inverter voltage and current with and without the negative-sequence voltage controller are compared in Fig. 4.8. The sequence components of voltage and current with the sequence-based controller are displayed with solid curves, and those without negative-sequence controller are presented in shaded curves with arrow markers. Fig. 4.8(a) shows that the positive-sequence voltages were controlled properly at 1 pu by both inverters with and without the negative-sequence voltage controller. However, the difference could be observed in the negative-sequence voltages. The negative-sequence voltage with the sequence-based controller suggests that the inverter was able to limit the negative-sequence voltage at 0 pu, and the grid voltage was kept balanced because it only consists of positive-sequence voltage.

However, the negative-sequence voltage was non-zero when the inverter did not control sequence components. The negative-sequence voltage was the largest from t = 5 to 11 second when the first two unbalanced loads were energized. From t = 5 to 11 seconds, the negative-sequence voltage was 0.12 pu, and it reduced to 0.04 pu at the steady-state after balanced loads were also energized.

The sequence components of the inverter current shown in Fig.4.8(b) imply that inverter controls the negative-sequence current to balance the voltage. It can be noticed that the inverter injects more negative-sequence current when it is capable of balancing voltage. At the steady-state, the inverter injects a negative-sequence current of 0.06 pu when it controls the negative-sequence components, but a negative-sequence current of 0.03 pu was supplied when

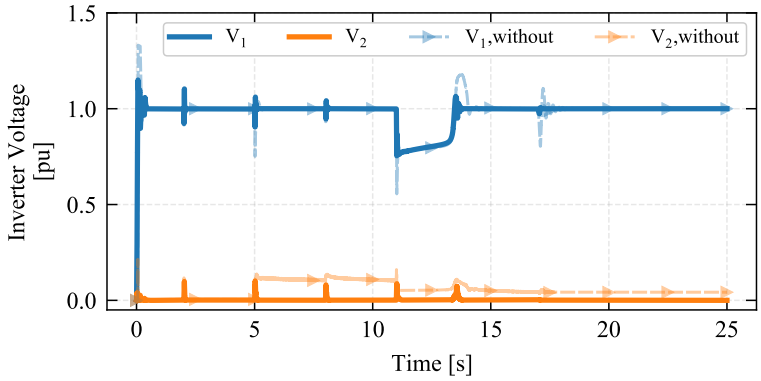

(a)

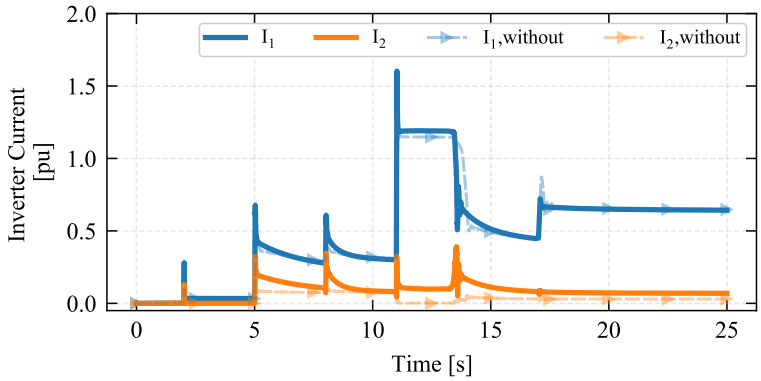

(b)

Figure 4.8: Sequence components of the inverter (a) voltage (b) current with and without the negative-sequence voltage controller.

the inverter does not control the sequence components.

The steady-state instantaneous voltages with all loads energized are shown in Fig. 4.9. The voltage with a negative-sequence controller is illustrated in Fig. 4.9(a). It can be seen that the peak values of the voltages are equal and controlled at 1 pu. In contrast, the voltages shown in Fig. 4.9(b) without controlling the negative-sequence voltage have different peak values. Phase

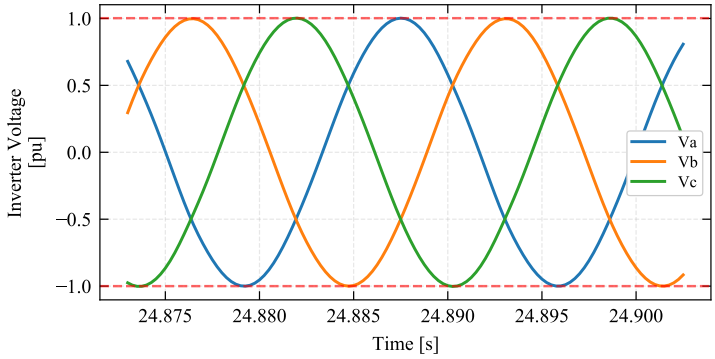

(a)

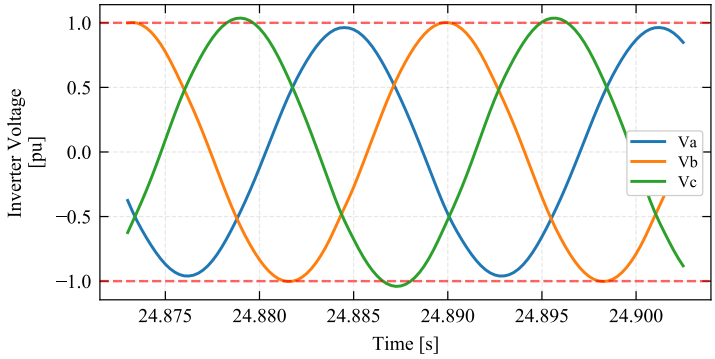

(b)

Figure 4.9: Steady-state instantaneous voltages (a) with (b) without the negative-sequence voltage controller.

C voltage was 1.03 pu, but the phase A voltage was 0.99 pu. The results demonstrate that having the sequence-based voltage controller in the grid-forming inverter could make the voltage balanced while supplying unbalanced loads and improves the power quality of the microgrid.

4.6 Final Remarks

The blackstart operation of islanded microgrids using the grid-forming inverter is analyzed in this paper. The inverter is equipped with a sequence-based voltage controller to balance the grid voltage, and a current limiter is implemented on the abc-frame to improve its performance when used on unbalanced systems. The simulation result demonstrates that the inverter is capable of blackstarting the islanded microgrid by generating the grid voltage. The inverter was able to limit its output current while starting an induction motor. Moreover, the grid voltage was maintained balanced while energizing unbalanced loads. The steady-state voltage shows that the inverter with sequence-based control ensured better power quality of the microgrid.

Chapter 5

Voltage Balancing Capability of Grid-Forming Inverters

5.1 Introduction

The operation region of the grid-forming inverter with voltage balancing capability is analyzed in this chapter. Simulation studies in Chapter 4 showed that grid-forming inverters can compensate for voltage imbalance while supplying unbalanced loads by injecting negative-sequence current. However, inverters cannot supply infinite negative-sequence current because of their relatively low rated capacity. Thus, their steady-state operation limit is investigated in this chapter.

First, the range of negative-sequence current the inverter can supply is analyzed. The I_2/I_1 ratio the inverter can manage is examined based on symmetrical components. Moreover, formulas used to determine the required inverter capacity to supply unbalanced loads are derived. The formulation includes delta-Yg connection of transformers as discussed in Section 1.1. The inverter's size can be computed using only the load size and power factor without requiring analytical methods.

Parts of the work presented in this chapter appear in the following published papers:

– **T. Kim**, N. Barry, W. Kim, S. Santoso, W. Wang, R. Dugan, D. Ramasubramanian, and A. Maitra, "Voltage Balancing Capability of Grid-Forming Inverters", in *IEEE Open Access Journal of Power and Energy (Submitted)*.

The chapter is organized as follows. In Section 5.2, the sequence-based control of grid-forming inverter and the relationship between transformer connection and voltage unbalance is analyzed. In Section 5.3, the range of positive- and negative-sequence current the inverter can supply is identified. The equations for computing the inverter size are derived in Section 5.4. Section 5.5 presents example cases of using the proposed equations. Final remarks are discussed in Section 5.6.

5.2 Voltage Balancing Control of Grid-Forming Inverter Based on Symmetrical Components

This section presents a control strategy for a three-phase three-legged grid-forming inverter based on the symmetrical components of voltage and current. The inverter maintains balanced grid voltage by controlling positive- and negative-sequence components separately. The zero-sequence current, which is also important for balancing the load side voltage, originates from the interconnection transformer. Thus, the voltages on both sides of the transformer with different connections are also investigated.

5.2.1 Control Strategy of Grid-Forming Inverter

The overall control structure of the grid-forming inverter was presented in Section 4.2. Since the inverter is modeled as a three-phase three-leg inverter that does not have a ground connection, zero-sequence components are not included in the inverter controller. The relationship between zero-sequence components and transformer connections are discussed in the following section.

In Chapter 3 and Chapter 4, current limiter was used to regulate transient currents during fault and motor start. In this chapter, the current limiter

is used to control the long-term steady-state current according to inverter's rated current. When the sum of positive- and negative-sequence current exceeds the rated current, the inverter cannot supply enough current and fails to control grid voltage. Therefore, I_{lim} is determined the same as the rated current in this chapter.

5.2.2 Interconnection Transformer Connection and Zero-Sequence Current

The three-leg inverter with the controller presented in Fig. 4.1 can control the positive- and negative-sequence components of voltage and current. However, a zero-sequence current is also needed balance the load side voltage. Therefore, the interconnection transformer interfacing the inverter must supply zero-sequence current. Among possible transformer connections, the commonly used delta-wye grounded (Yg) and Yg-Wye (Y) are chosen to be studied [56, 57]. (transformer naming convention is inverter side - load side throughout this chapter) The sequence components of voltages and currents on both sides of the transformer with different connections are analyzed using PSCAD/EMTDC.

Equivalent networks of delta-Yg and Yg-Y transformers are shown in Fig. 5.1 and Fig. 5.2. The inverter on the primary side and the load on the secondary side are replaced by equivalent impedance Z_{inv} and Z_{load}, respectively, and Z_t indicates the transformer impedance. The inverter is a three-phase three-leg inverter rated at 0.6 kV and 500 kVA. The load is an unbalanced load composed of 200 kW, 100 kW, and 100 kW on each phase with rated voltage of 12.47 kV.

Fig. 5.1 shows that the inverter side of the delta-Yg transformer does not have a zero-sequence connection. Yet, there is a zero-sequence path on the

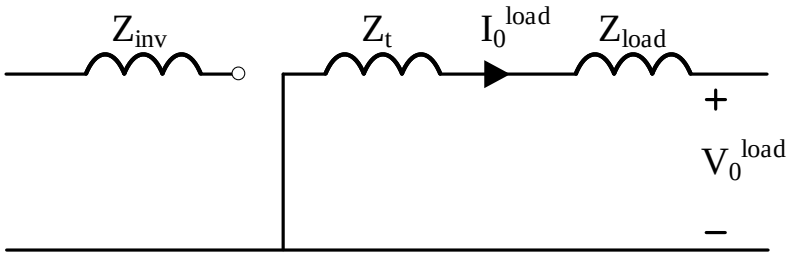

Figure 5.1: Equivalent zero-sequence network of delta-Yg transformer.

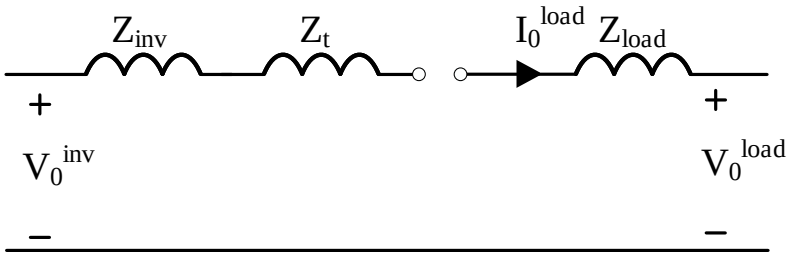

Figure 5.2: Equivalent zero-sequence network of Yg-Y transformer.

load side because of the grounding on the Yg side. Thus, the interconnection transformer can supply zero-sequence current to the load, and the inverter can balance the voltage on both sides by controlling positive- and negative-sequence components.

The performance of the inverter's voltage balancing control when interfaced with a delta-Yg transformer is demonstrated in Fig. 5.3. Fig. 5.3(a) and (b) show the inverter side voltage and current, and Fig. 5.3(c) and (d) present those measured on the load side. Both voltage and current are per-unitized to compare primary and secondary side measurements.

Fig. 5.3(a) and (c) show that both inverter and load voltages consist only of the positive-sequence component without negative- and zero-sequence voltage. Fig. 5.3(b) and (d) indicate that the inverter does not

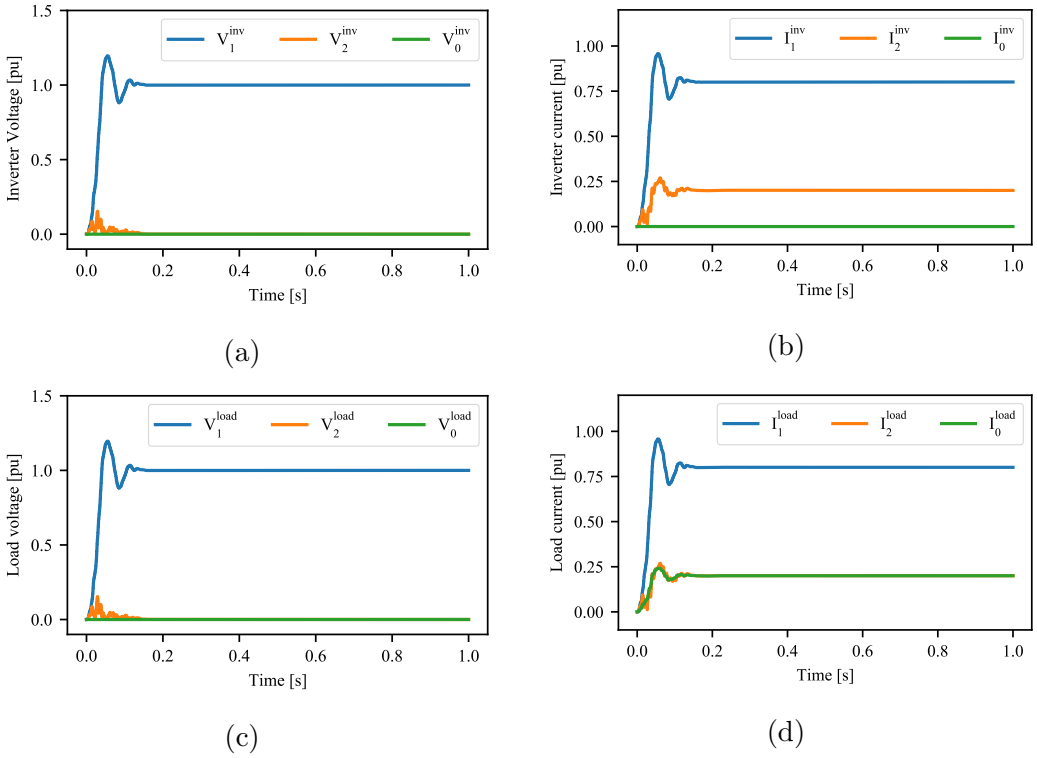

(a) (b) (c) (d)

Figure 5.3: Sequence components of voltage and current with delta-Yg transformer. (a) Inverter voltage. (b) Inverter current. (c))Load voltage. (d) Load current.

supply zero-sequence current, but the transformer grounding path does inject zero-sequence current to the loads. Simulation results show that the inverter can balance both voltages by installing the inverter with delta-Yg transformer and sufficiently low grounding impedance.

However, the equivalent circuit of the Yg-Y transformer presented in Fig. 5.2 shows that both the primary and secondary sides are not connected to ground. Also, the zero-sequence networks of the inverter and the load are not connected. In this case, the inverter side, which does not have a ground connection, does not require zero-sequence current. In contrast, the load is con-

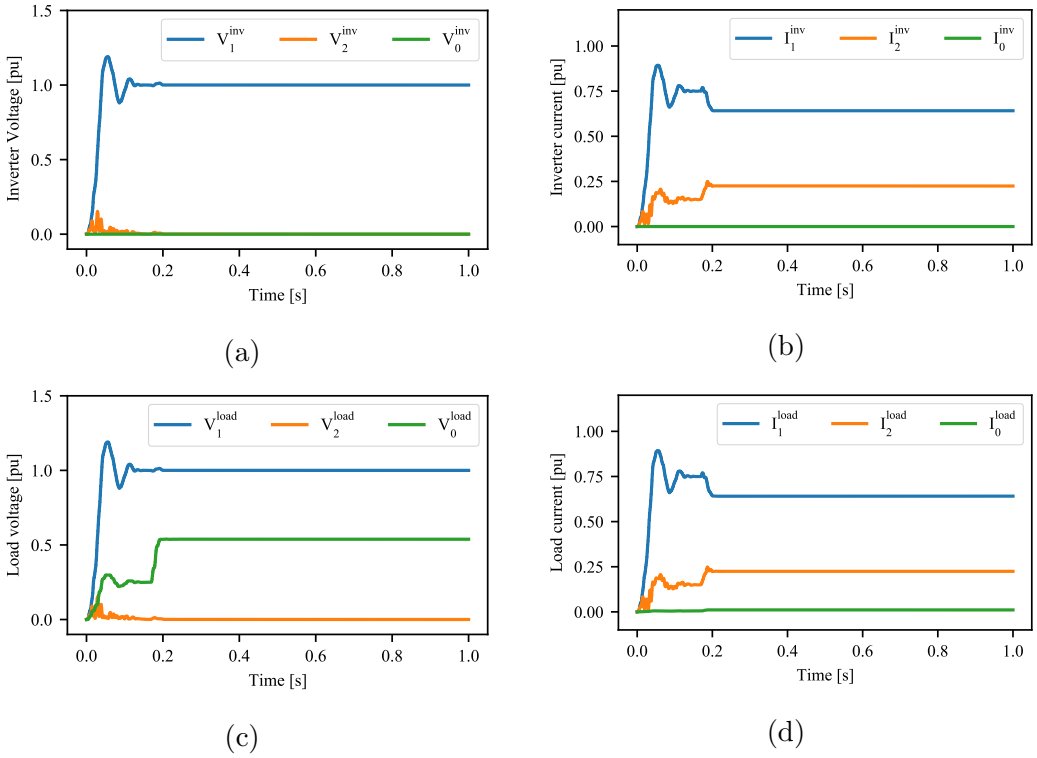

(a) (b) (c) (d)

Figure 5.4: Sequence components of voltage and current with Yg-Y transformer. (a) Inverter voltage. (b) Inverter current. (c) Load voltage. (d) Load current.

nected to the ground and requires zero-sequence current to make the voltage balanced.

The simulation results with a Yg-Y transformer are shown in Fig. 5.4. Fig. 5.4(a) indicates that there is only a positive-sequence voltage of 1 pu, which shows that the inverter side voltage is controlled well and balanced. On the other hand, the load voltage shown in Fig. 5.4(c) shows that the secondary side voltage has a zero-sequence component and is not balanced. By comparing Fig. 5.3 (d) and Fig. 5.4 (d), it can be noticed that zero-sequence current is not supplied to the load in the case with Yg-Y transformer because neither the

inverter nor the transformer can supply zero-sequence current, as shown in Fig. 5.4(b) and (d). As a result, even if the inverter controls the negative-sequence voltage, the load side voltage remains unbalanced.

The results shown in Fig. 5.3 suggest that without a separate grounding transformer, a three-phase three-leg inverter must be interfaced with a delta-Yg transformer to balance voltages on both sides of the transformer. As presented in Fig. 5.4, other transformer connections cannot supply zero-sequence current and the secondary side load voltage becomes unbalanced.

5.3 Operation Region of Grid-Forming Inverters Used in Unbalanced Systems

This section analyzes the range of positive- and negative-sequence current the inverter can supply while maintaining balanced voltage. The range of negative-sequence current the inverter can inject could be used to understand how much imbalance the inverter can handle. Negative-sequence current injection is limited by the rated capacity of the inverter, which is given as an RMS value. The relationship between the negative-sequence current and the rated capacity could be investigated using the transformation matrix shown in (5.1).

$$\begin{bmatrix} \mathrm{I_a}\angle\theta_\mathrm{a} \\ \mathrm{I_b}\angle\theta_\mathrm{b} \\ \mathrm{I_c}\angle\theta_\mathrm{c} \end{bmatrix} = \frac{1}{3}\begin{bmatrix} 1 & 1 & 1 \\ 1 & a^2 & a \\ 1 & a & a^2 \end{bmatrix}\begin{bmatrix} \mathrm{I_0}\angle\theta_0 \\ \mathrm{I_1}\angle\theta_1 \\ \mathrm{I_2}\angle\theta_2 \end{bmatrix}. \tag{5.1}$$

In (5.1), $\mathrm{I_{abc}}\angle\theta_\mathrm{abc}$ represents the inverter currents in each phase, and $\mathrm{I_{012}}\angle\theta_{012}$ indicates the symmetrical component of the inverter current. However, it can be seen that six parameters (three angles and three magnitudes) are needed to calculate the range of current the inverter can supply.

Therefore, we use an alternative method which requires only the RMS values of the currents in each phase [58]. The magnitude of the positive- and negative-sequence currents could be calculated as follows,

$$I_1 = \sqrt{\frac{A_m^2 + \frac{4A_s^2}{\sqrt{3}}}{2}},\ I_2 = \sqrt{\frac{A_m^2 - \frac{4A_s^2}{\sqrt{3}}}{2}}. \tag{5.2}$$

where A_m^2 and A_s^2 are defined below.

$$A_m^2 = \frac{I_a^2 + I_b^2 + I_c^2}{3}, \tag{5.3}$$

$$A_s^2 = \sqrt{p(p - I_a)(p - I_b)(p - I_c)}, \tag{5.4}$$

$$p = \frac{I_a + I_b + I_c}{2}. \tag{5.5}$$

Equation (5.2) shows that only three RMS values are needed to calculate the positive- and negative-sequence components of the inverter current. Thus, we can visualize the feasible combinations of positive- and negative-sequence currents using three axes and one color map, as shown in Fig. 5.4.

The range of the positive- and negative-sequence currents and the ratio of those the inverter can supply are shown in Fig. 5.4. Each axis in the figure represents the inverter current in each phase from 0 to 1 pu, and the color map shows the range of (a) positive-sequence current magnitude I_1 and (b) negative-sequence current magnitude I_2.

Fig. 5.4(a) shows that the inverter can supply a positive-sequence current from 0 to 1 pu, and its maximum value is 1 pu at the center of the three-dimensional figure when currents are balanced (when $I_a = I_b = I_c = 1$ pu).

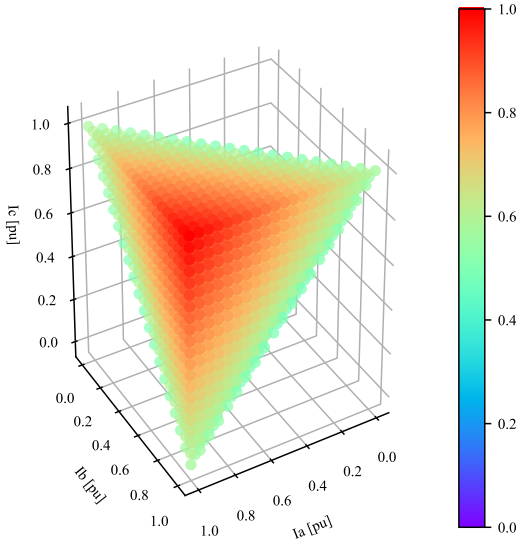

(a)

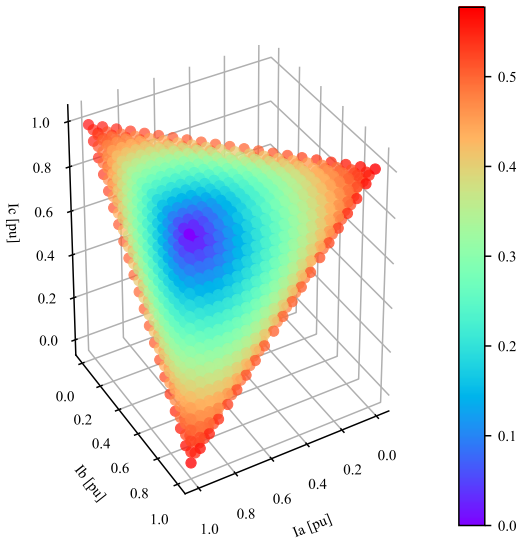

(b)

Figure 5.4: Range of (a) positive-sequence current (b) negative-sequence current the inverter can supply.

However, Fig. 5.4(b) shows that the maximum negative-sequence current inverter can deliver is 0.577 ($= \frac{1}{\sqrt{3}}$) pu at the triangular surface's vertices. The coordinates of vertices, I_2 (1,1,0), I_2 (1,0,1), and I_2 (0,1,1), show that negative-sequence current is the largest when 1 pu current is flowing in two phases and no current flows in the remaining phase. It can be seen that the positive-sequence current on the vertices of the triangular surface of Fig. 5.4(a) are also 0.577 pu. Therefore, the maximum $\frac{I_2}{I_1}$ ratio the inverter can provide is 100% and the minimum $\frac{I_2}{I_1}$ ratio is 0%, when currents are balanced.

5.4 Formulas to Determine the Minimum Capacity of the Inverter Required to Balanced the Voltage

The range of unbalanced current the inverter can supply was analyzed in the previous section. This section proposes equations to determine the minimum capacity of the inverter when maintaining balanced voltage and operating within the range investigated in Section 5.3.

When the system is balanced we can simply calculate the required inverter size by aggregating all the loads in the system. However, calculating the capacity required to supply an unbalanced load is not straightforward. Moreover, due to the delta-Yg transformer requirement to supply zero-sequence current, it becomes challenging to estimate the required inverter size. When interfaced using a delta-Yg transformer, the current supplied to the delta side will not be proportional to the size of load on the Yg side, especially when the phase angles of currents in each phase are unbalanced. Thus, equations to estimate the required size of the inverter on the delta side are derived using the size of load on the Yg side.

The equation used to determine the current that has to be supplied

from phase A of the inverter (delta-side) could be computed using the currents required on the Yg side. Line-to-neutral quantities in per units are used to derive the proposed equation. The current on the delta side could be calculated as shown below,

$$\mathrm{I_a}\angle\theta_\mathrm{a} = \mathrm{I_{aY}}\angle\theta_\mathrm{aY} - \mathrm{I_{cY}}\angle\theta_\mathrm{cY}. \tag{5.6}$$

In (5.6), $\mathrm{I_a}$ and θ_a represent the magnitude and angle of the current on the delta side, and $\mathrm{I_{aY}}$ and θ_{aY} are those measured on the Yg side. Separating the real and imaginary parts to calculate the magnitude of the current required on phase A results in,

$$Re\{\mathrm{I_a}\angle\theta_\mathrm{a}\} = \mathrm{I_{aY}}\cos(\theta_\mathrm{aY}) - \mathrm{I_{cY}}\cos(\theta_\mathrm{cY}), \tag{5.7}$$

$$Im\{\mathrm{I_a}\angle\theta_\mathrm{a}\} = \mathrm{I_{aY}}\sin(\theta_\mathrm{aY}) - \mathrm{I_{cY}}\sin(\theta_\mathrm{cY}). \tag{5.8}$$

Next (5.7) and (5.8) are used to derive an equation used to determine the required inverter current to supply the loads on the Yg side. The proposed equation for phase A is presented below,

$$|I_a| = Re\{\mathrm{I_a}\angle\theta_\mathrm{a}\}^2 + \mathrm{Im}\{\mathrm{I_a}\angle\theta_\mathrm{a}\}^2 \tag{5.9}$$

$$= \mathrm{I_{aY}^2} + \mathrm{I_{cY}^2} - 2\mathrm{I_{aY}I_{cY}}\cos(\theta_\mathrm{aY} - \theta_\mathrm{cY}). \tag{5.10}$$

It can be noticed that the right side of (5.10) consists only of the wye side quantities. Using (5.10), we can estimate the magnitude of current inverter has to supply.

The inverter's rated current should be higher than the current magnitude calculated using (5.10). Thus, inequalities can be used to decide the

minimum rated current of a grid-forming inverter. Inequalities for all three phases could be written as below,

$$\mathrm{I}_{\mathrm{aY}}^2 + \mathrm{I}_{\mathrm{cY}}^2 - 2\mathrm{I}_{\mathrm{aY}}\mathrm{I}_{\mathrm{cY}}\cos(\theta_{\mathrm{aY}} - \theta_{\mathrm{cY}}) \leq I_{lim,a}^2, \tag{5.11}$$

$$\mathrm{I}_{\mathrm{bY}}^2 + \mathrm{I}_{\mathrm{aY}}^2 - 2\mathrm{I}_{\mathrm{bY}}\mathrm{I}_{\mathrm{aY}}\cos(\theta_{\mathrm{bY}} - \theta_{\mathrm{aY}}) \leq I_{lim,b}^2, \tag{5.12}$$

$$\mathrm{I}_{\mathrm{cY}}^2 + \mathrm{I}_{\mathrm{bY}}^2 - 2\mathrm{I}_{\mathrm{cY}}\mathrm{I}_{\mathrm{bY}}\cos(\theta_{\mathrm{cY}} - \theta_{\mathrm{bY}}) \leq I_{lim,c}^2, \tag{5.13}$$

where $I_{lim,a}$, $I_{lim,b}$, and $I_{lim,c}$ are current limits of each phase.

Assuming that both the inverter and load side voltage magnitudes are controlled at 1 pu with balanced phase angles, current magnitudes in (5.11) - (5.13) could be substituted with load sizes S_{abcY}. Inequalities written in load sizes and power factor angles are given as,

$$\mathrm{S}_{\mathrm{aY}}^2 + \mathrm{S}_{\mathrm{cY}}^2 - 2\mathrm{S}_{\mathrm{aY}}\mathrm{S}_{\mathrm{cY}}\cos(\theta_{\mathrm{aY}} - \theta_{\mathrm{cY}}) \leq S_{lim,a}^2, \tag{5.14}$$

$$\mathrm{S}_{\mathrm{bY}}^2 + \mathrm{S}_{\mathrm{aY}}^2 - 2\mathrm{S}_{\mathrm{bY}}\mathrm{S}_{\mathrm{aY}}\cos(\theta_{\mathrm{bY}} - \theta_{\mathrm{aY}}) \leq S_{lim,b}^2, \tag{5.15}$$

$$\mathrm{S}_{\mathrm{cY}}^2 + \mathrm{S}_{\mathrm{bY}}^2 - 2\mathrm{S}_{\mathrm{cY}}\mathrm{S}_{\mathrm{bY}}\cos(\theta_{\mathrm{cY}} - \theta_{\mathrm{bY}}) \leq S_{lim,c}^2, \tag{5.16}$$

where $S_{lim,a}$, $S_{lim,b}$, and $S_{lim,c}$ are required powers in each phase. Assuming the load has a unity power factor, we can remove cosine terms in (5.14) - (5.16) and simplify to have only the load size terms as follows,

$$\mathrm{S}_{\mathrm{aY}}^2 + \mathrm{S}_{\mathrm{cY}}^2 + \mathrm{S}_{\mathrm{aY}}\mathrm{S}_{\mathrm{cY}} \leq S_{lim,a}^2, \tag{5.17}$$

$$\mathrm{S}_{\mathrm{bY}}^2 + \mathrm{S}_{\mathrm{aY}}^2 + \mathrm{S}_{\mathrm{bY}}\mathrm{S}_{\mathrm{aY}} \leq S_{lim,b}^2, \tag{5.18}$$

$$\mathrm{S}_{\mathrm{cY}}^2 + \mathrm{S}_{\mathrm{bY}}^2 + \mathrm{S}_{\mathrm{cY}}\mathrm{S}_{\mathrm{bY}} \leq S_{lim,c}^2. \tag{5.19}$$

The range of loads that satisfies all three inequalities presented in (5.17) - (5.19) are illustrated in Fig. 5.5. If the coordinate of the unbalanced load is located below the curved surface, the inverter can deliver power without losing

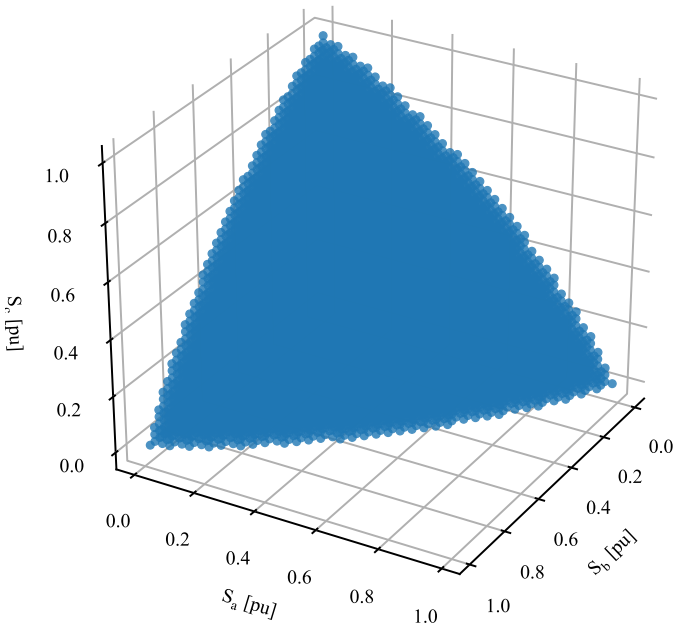

Figure 5.5: Possible combinations of wye side currents which the inverter can supply

the balanced voltage. On the other hand, given a load demand, the inverter capacity calculated using the proposed equation is the minimum required capacity for maintaining balanced voltage at steady-state and does not account for contingencies.

The inverter capacity required in each phase could be determined by solving (5.14) - (5.16). If three single-phase inverters are installed in each phase, their sizes will be $S_{lim,a}$, $S_{lim,b}$, and $S_{lim,c}$, respectively. When the inverter has three-phase configuration, we determine its capacity as shown below,

$$S_{lim,3\phi} = 3 \cdot \max\{S_{lim,a}, S_{lim,b}, S_{lim,c}\}. \tag{5.20}$$

We choose the largest value among the calculated values, and multiply by 3

to determine the three-phase capacity.

5.5 Case Studies and Validation of the Proposed Equation

This section demonstrates the implementation of the proposed inequality and validates the solution by running a PSCAD/EMTDC simulation. The required inverter capacities for each case are calculated using the proposed equations. The performance of the inverter with the computed capacity is examined using a detailed model with controller shown in Fig. 4.1.

5.5.1 Case 1: Calculating the Minimum Required Inverter Capacity for Given Load Size

The first case, we determine the inverter capacity needed to maintain balanced voltage while supplying an unbalanced load installed in the test system. The test sytem shown in Fig. 5.6 consists of a grid-forming inverter, a delta-Yg transformer, and total 300 kVA unbalanced load. The size and power factor of the unbalanced load are:

- phase A: 150 kVA, pf = 0.9,
- phase B: 100 kVA, pf = 0.8,
- phase C: 50 kVA, pf = 0.7.

First the phase angle of each load is calculated using the given power factor. Phase shifts of 240° and 120° are applied to phase B and C. For example, the phase angle of phase A is calculated as,

$$\theta_{aY} = -\cos^{-1}(0.9) = -25.84^{\circ}, \tag{5.21}$$

By substituting load sizes and phase angles into (5.14) - (5.16), required inverter capacities are computed for each phase as,

$$95.93\,\text{kVA} \leq S_{lim,a}, \tag{5.22}$$

$$131.74\,\text{kVA} \leq S_{lim,b}, \tag{5.23}$$

$$78.97\,\text{kVA} \leq S_{lim,c}. \tag{5.24}$$

It can be seen that each phase requires different capacities because of the unbalanced load and they are not proportional to the load size on each phase. Since the objective is to determine the size of a three-phase inverter, we calculate the three-phase capacity using (5.20).

$$S_{lim,3\phi} = \sqrt{3} \cdot \max\{S_{lim,a}, S_{lim,b}, S_{lim,c}\} = 395.70\,\text{kVA}. \tag{5.25}$$

Equation (5.25) shows that the inverter must be larger than 395.70 kVA, which is much larger compared to the load size, 300 kVA. The calculated inverter capacity is validated using PSCAD/EMTDC. Since the calculated values do not consider losses in the system, inverters with slightly larger capacities were used for validation. Inverters with sizes of 395 kVA and 400 kVA were selected and voltage and current measured on the inverter side were analyzed.

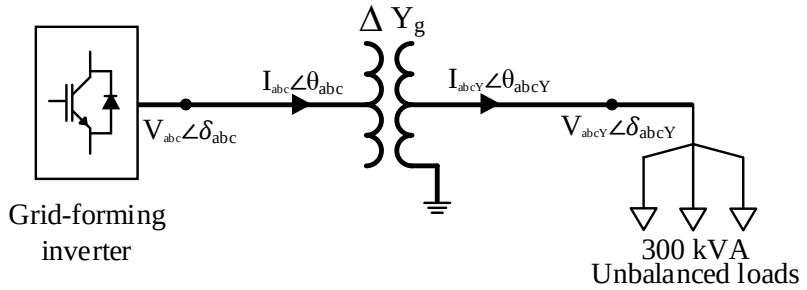

Figure 5.6: Small test system with delta-Yg transformer and unbalanced loads.

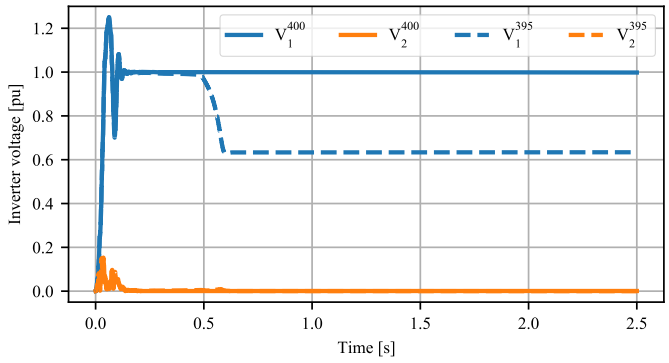

(a)

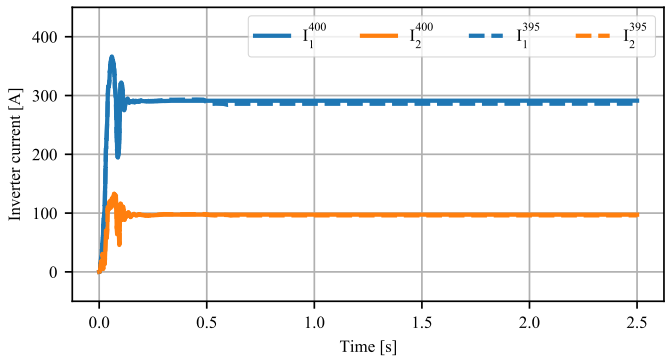

(b)

Figure 5.7: Sequence components of (a) voltage and (b) current with inverter sizes of 400 kVA (solid line) and 395 kVA (dashed line).

The voltage and current measured on the delta side of the interconnection transformer with different sized inverters are presented in Fig. 5.7. The blue curve displays the positive-sequence component, and the orange curve shows the negative-sequence components. Superscripts for voltages and currents indicate the inverter size.

The voltage presented with solid line in Fig. 5.7(a) shows that the 400 kVA inverter can successfully control the voltage. The positive sequence-voltage was controlled at 1 pu, and the negative-sequence current was regulated

to 0 pu. In contrast, the dotted curve shows that the voltage is not controlled when the inverter size is reduced to 395 kVA, which is smaller than the calculated value shown in (5.25). The positive-sequence voltage dropped to 0.6 pu, and the negative-sequence voltage is not limited at 0 pu.

This is because the rated current of 395 kVA inverter is lower than required. The current limiter is activated at t = 0.5s, and the voltage starts to drop sequentially. Simulation results prove that the required capacity lies between 395 kVA and 400 kVA, which matches well with the computed value shown in (5.25).

5.5.2 Case 2: Calculating the Minimum Required Inverter Capacity for Given Current Requirements

The second example case shows how to determine the inverter size when system requirements are given as the wye-side current magnitude and the I_2/I_1 ratio. The current magnitude that the inverter has to supply is specified, for example, 10 A with I_2/I_1 of 20% for this case. We use the same test system presented in Fig. 5.6.

However, wye-side current magnitude and the I_2/I_1 ratio are not sufficient to calculate the minimum inverter size. The phase angle of the negative-sequence current is also required to calculate the inverter size accurately. Hence, the range of inverter size is determined with negative-sequence phase angle varying from -180° to 180°. The sequence components of current are transformed to the abc-frame using the matrix shown in (5.1) and solve (5.14) - (5.16).

Fig. 5.8 presents the required inverter size with different negative-sequence current angles. The red dotted line shows the maximum of the three

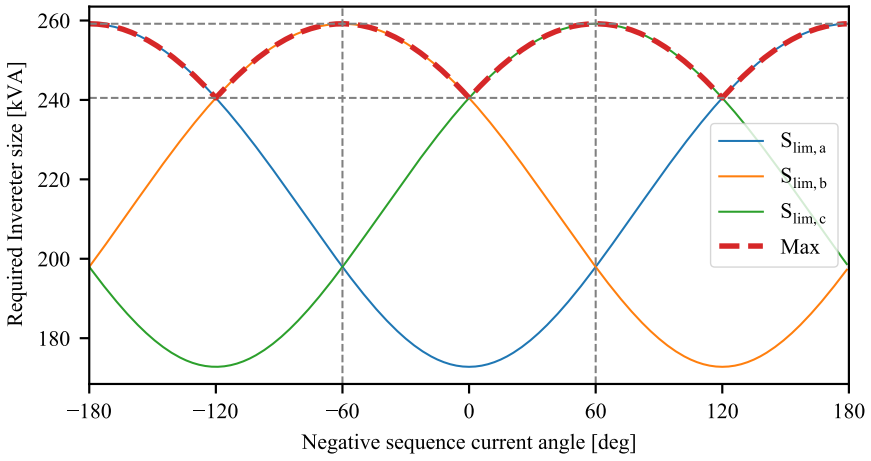

Figure 5.8: Required inverter capacity with varying negative-sequence current angle.

curves. For example, when the angle is 0°, the inverter has to be larger than 240.51 kVA. When the phase angle is -60° or 60°, the required inverter size increases to 259.18 kVA. Thus, we choose 259.18 kVA to meet the current requirement at all phase angles.

The calculated minimum inverter capacity when the negative-sequence current angle is 60° is validated using PSCAD/EMTDC. Angle of 60° is chosen because the required capacity becomes the largest as shown in Fig. 5.8. Current requirements are converted to corresponding constant PQ loads to be used in PSCAD/EMTDC. The load size is specified as follows:

- Phase A: 79.2 kW – 12.47 kvar
- Phase B: 79.2 kW + 12.47 kvar
- Phase C: 57.6 kW

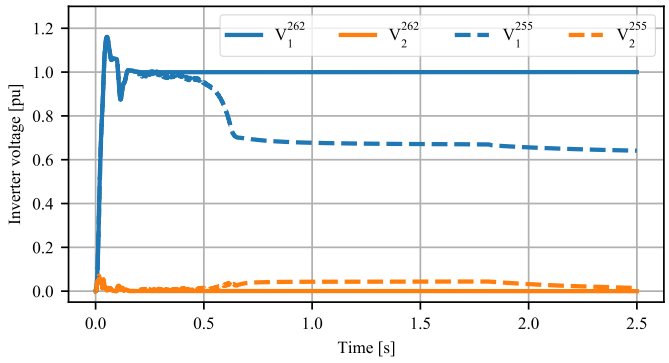

(a)

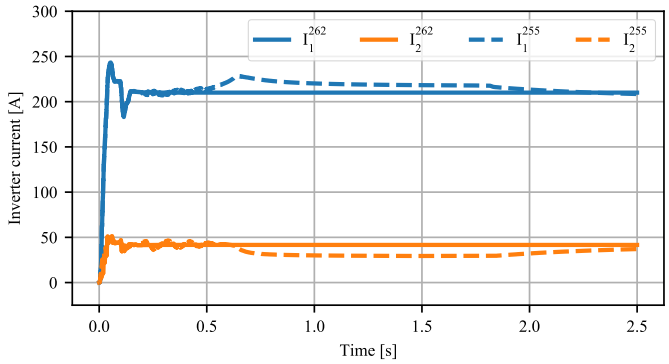

(b)

Figure 5.9: Sequence components of (a) voltage and (b) current with inverter sizes of 262 kVA (solid line) and 255 kVA (dashed line).

Inverter sizes of 255 kVA and 262 kVA are chosen to validate the limit we calculated in Fig. 5.8. The voltage and current measured on the delta side of the transformer are presented in Fig. 5.9. Similar to Fig. 5.7, the superscripts indicate the inverter size and the subscripts represent the positive- and negative-sequence components.

The solid curve in Fig. 5.9(a) shows that the voltage is well controlled when the inverter size is 262 kVA. Both positive- and negative-sequence voltages are controlled at their desired values, 1 pu and 0 pu, respectively. However,

reducing the inverter size to 255 kVA resulted in unstable voltage.

Since the 255 kVA inverter cannot supply enough current to maintain balanced voltage, both positive- and negative-sequence voltages are not controlled. Therefore, we can assume that the inverter size requirement is between 255 kVA and 262 kVA. The result validates the solution presented in Fig. 5.8.

5.5.3 Case 3: Applying the Proposed Equations to a Larger System

This case presents the implementation of the proposed inequalities in a larger system, the modified IEEE 34 node test feeder presented in Fig. 5.10. The voltage source at Bus 800 is replaced by a grid-forming inverter and interfaced using a delta-Yg transformer. The inverter size is determined by running an hourly quasi-static time series (QSTS) simulation for 24 hours using OpenDSS. The hourly load profiles for each phase are presented in Fig.5.11. The size of loads installed in each phase are:

- Phase A: 606 kW + 357 kvar = 703.34 kVA
- Phase B: 584 kW + 344 kvar = 677.78 kVA
- Phase C: 579 kW + 343 kvar = 672.97 kVA

The required inverter size is calculated every hour using (5.14) - (5.16) and the maximum value during peak load hours is determined as the required inverter size. The complex power and power factor angle needed on the Yg side of the interconnection transformer are used to compute the required inverter capacity for each phase. The inverter output current is obtained from OpenDSS and used to validate the calculated inverter capacity.

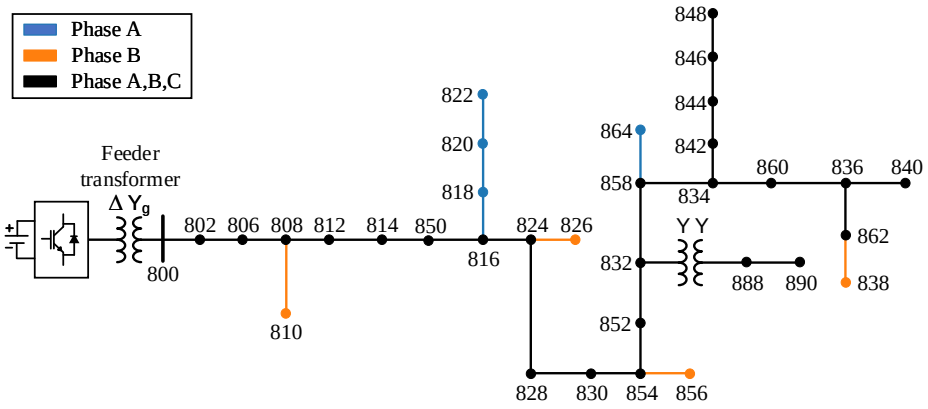

Figure 5.10: IEEE 34 node feeder modified to unbalanced islanded microgrid.

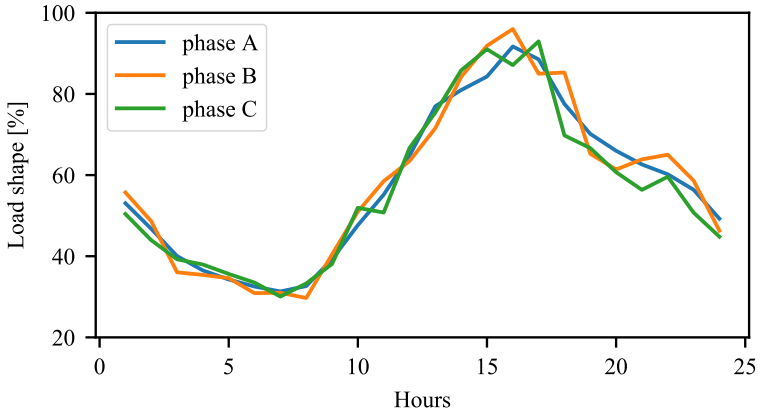

Figure 5.11: Hourly load profile for 24 hours.

The computed inverter size and current flowing in each phase are displayed in Fig. 5.12. The required inverter size is shown as a bar graph, and current is presented using a curve. The maximum inverter capacity required was 2172.19 kVA on phase A at 16:00, and the peak current was 2074.09 A in phase B.

Fig. 5.12 shows that the maximum current was flowing in phase B, but

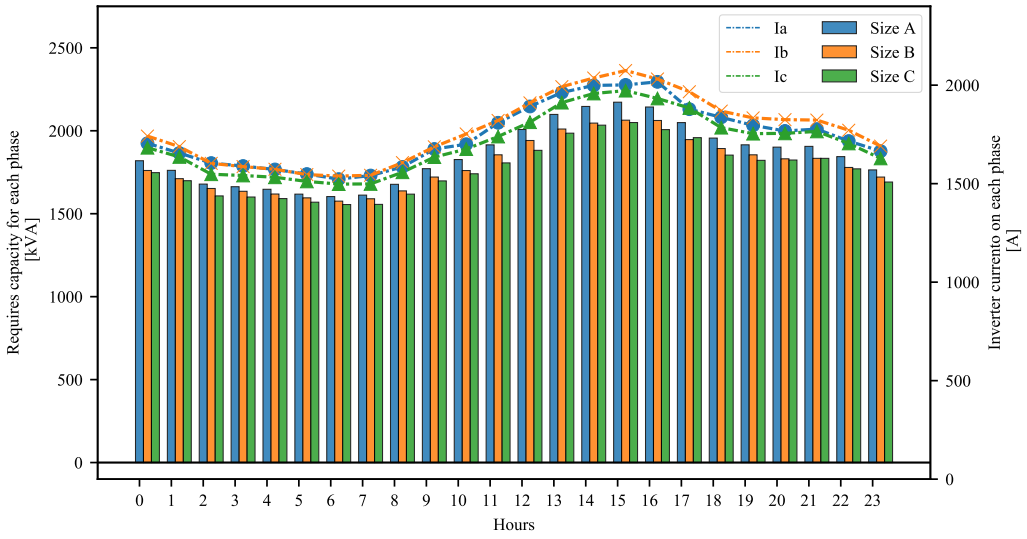

Figure 5.12: Required inverter sizes to supply IEEE 34 node test system.

phase A is the phase which needs the largest capacity due to the delta-Yg transformer. Phase A of the delta side, which supplies current to phase A and B on the Yg side, requires the largest capacity because phase A and B are heavily loaded compared to phase C. Therefore, 2172.19 kVA is selected as the inverter size.

The calculated minimum inverter capacity is validated by comparing the current limits of inverters obtained from different methods. Equations (5.26) and (5.27) show the equations for calculating the inverter size in a balanced three-phase system. $S_{lim,sum}$ in (5.26) is calculated using only the rated load size, while $S_{lim,loss}$ in (5.27) considers both load size and system loss.

$$S_{lim,sum} = \sqrt{(\sum P_{load})^2 + (\sum Q_{load})^2} \tag{5.26}$$

$$S_{lim,loss} = \sqrt{(\sum P_{load} + P_{loss})^2 + (\sum Q_{load} + Q_{loss})^2} \tag{5.27}$$

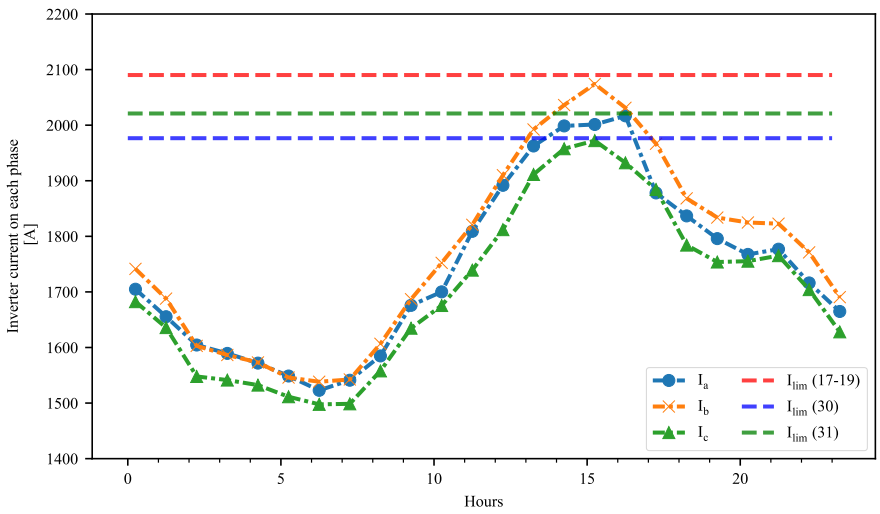

Figure 5.13: Required currents from the system and inverter current limit calculated with different methods.

The inverter output current obtained from OpenDSS and the current limit of inverters with different sizes are shown in Fig. 5.13. The inverter sizes are calculated using (5.14) - (5.16), (5.26), and (5.27). The current limits of each inverter are illustrated with horizontal lines. It can be seen that the current limits calculated by (5.26) and (5.27) are much lower than the largest inverter current on phase B at 16:00. The current required on phase B was 2074.09 A, but the rated currents calculated using (5.26) and (5.27) were only 1976.55 A and 2021.02 A, respectively.

In contrast, the rated current of the inverter with a size calculated using (5.14) - (5.16) is large enough to deliver the peak current required on phase B. The computed current limit was 2090.19 A, which is slightly larger than the current needed on phase B. The simulation result shows that the proposed equation could be applied to large systems, and the current limit shown in Fig. 5.13 verifies the solution obtained from proposed inequalities.

5.6 Final remarks

This chapter analyzed the grid-forming inverter's voltage balancing capability based on the range of unbalanced current the inverter can supply. The range of possible negative-sequence is investigated considering inverter's rated current. Also, equations to determine inverter size needed to maintain a balanced voltage while supplying unbalanced loads are proposed. Case studies showed that the proposed equations could be applied to both small and large systems. Simulation results using a detailed model verified that inverters with calculated capacities can effectively control both positive- and negative-sequence voltages.

Chapter 6

Power Sharing of Grid-Forming Inverters in Unbalanced Microgrids

6.1 Introduction

The operation of a stand-alone microgrid with a single grid-forming inverter was analyzed in Chapter 4 and Chapter 5. This chapter focuses on an islanded microgrid with multiple inverters and the power-sharing control of grid-forming inverters.

The positive-sequence components of currents supplied by each inverter are commonly shared using P - ω and Q - V droop controls. However, P - ω and Q - V droop controls do not contribute to controlling the negative-sequence current supplied by each inverter. The magnitude of negative-sequence current supplied by each inverter is determined by the equivalent negative-sequence impedance inverters. Therefore, a varying negative-sequence virtual impedance controller is added to adjust the equivalent negative-sequence impedance of inverters and allocate the negative-sequence current appropriately.

The chapter is organized as follows. In Section 6.2, controllers added to improve positive- and negative-sequence current sharing are described. In Section 6.3, case studies with and without the proposed virtual negative-sequence controller are presented. Final remarks are discussed in Section 6.4.

6.2 Power-Sharing Control of Grid-Forming Inverters

6.2.1 Voltage and Current Control of Grid-Forming Inverters

This section presents a power-sharing control strategy for grid-forming inverters used in stand-alone microgrids. The inverter controller is presented in Fig. 6.1. It can be seen that the controller consists of two parts, power-sharing controller (left) and voltage and current control loop (right).

The voltage and current control loop has the same structure as the controller introduced in Chapter 4. However, the PI controller in the current control loop is replaced with a virtual admittance controller to improve the reactive-power sharing capability of grid-forming inverters [43]. The virtual admittance control of a grid-forming inverter for both positive- and negative-sequence controllers are displayed in Fig. 6.2. Current reference signals $I^*_{abc,dq}$

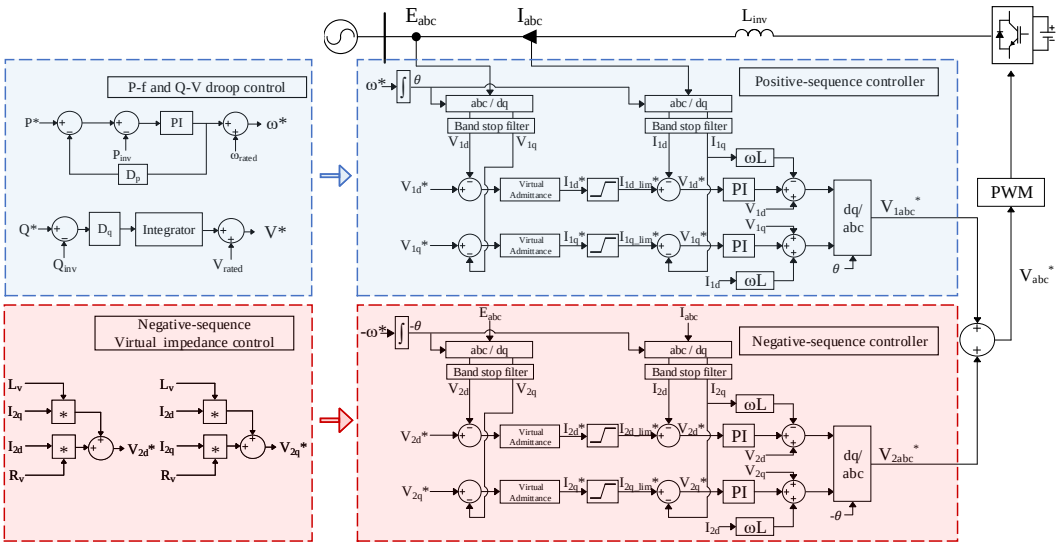

Figure 6.1: The control structure of grid-forming inverters with power-sharing control.

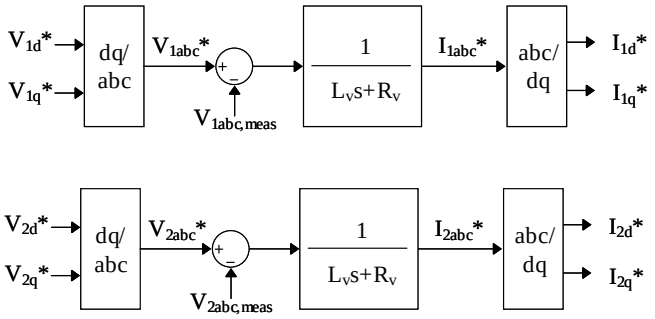

Figure 6.2: The virtual admittance controller of the grid-forming inverter.

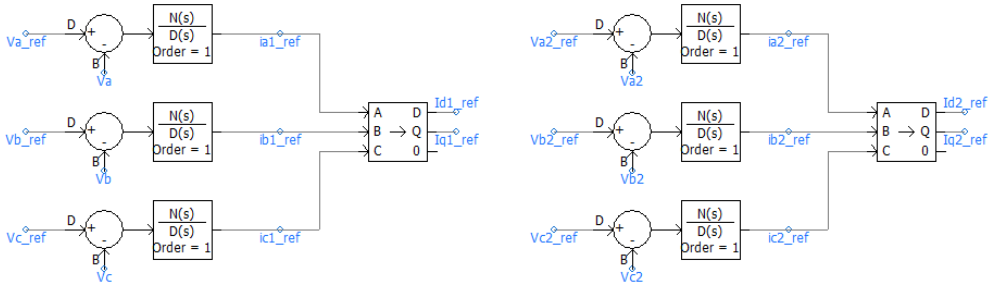

Figure 6.3: The virtual admittance controller implemented in PSCAD/ EMTDC.

are generated from the voltage error and transformed to the dq-axis as below,

$$I^*_{abc} = (V^*_{abc} - V_{abc}) \cdot \frac{1}{L_{vY}s + R_{vY}}, \tag{6.1}$$

where R_{vY} and L_{vY} are virtual resistance and reactance, respectively. The virtual admittance controller implemented in PSCAD/EMTDC is shown in Fig. 6.3.

6.2.2 Positive-Sequence Droop Controls of Grid-Forming Inverters

The positive-sequence current and power supplied by inverters could be controlled by implementing P - ω and Q- V droop control. The power injected

by inverters is regulated by providing different reference signals. When there is only one grid-forming inverter, V^* and ω^* are set to the rated values of one pu (0.6 kV) and 60 Hz, respectively.

The reference signals must be modified to allocate the output power of inverters having different capacities. New frequency and voltage magnitude references are determined by the active and reactive power setpoints and droop constants as follows,

$$\omega^* = \omega_{rated} + D_p(P^* - P_{inv}), \tag{6.2}$$

$$V^* = V_{rated} + D_q(Q^* - Q_{inv}), \tag{6.3}$$

where D_p and D_q are droop constants for active and reactive power; P^* and Q^* are nominal power setpoints of the inverter; P_{inv} and Q_{inv} are the measured power outputs of the inverter. By choosing appropriate values of D_p, D_q, P^* and Q^*, we can control the output powers of inverters.

In this work, inverters aim to share power proportionally to their rated capacities. Thus, P^* and Q^* are set proportionally to inverters' capacities and D_p and D_q are chosen inversely proportional to the ratings of each inverter. The block diagram of the inverter droop controllers developed in PSCAD/EMTDC is presented in Fig. 6.4.

6.2.3 Negative-Sequence Virtual Impedance Control of Grid-Forming Inverters

The negative-sequence currents supplied by the grid-forming inverters are determined by the equivalent negative-sequence impedances of each inverter if the inverter has only a positive-sequence droop controller. Therefore, we add a virtual negative-sequence impedance controller that generates

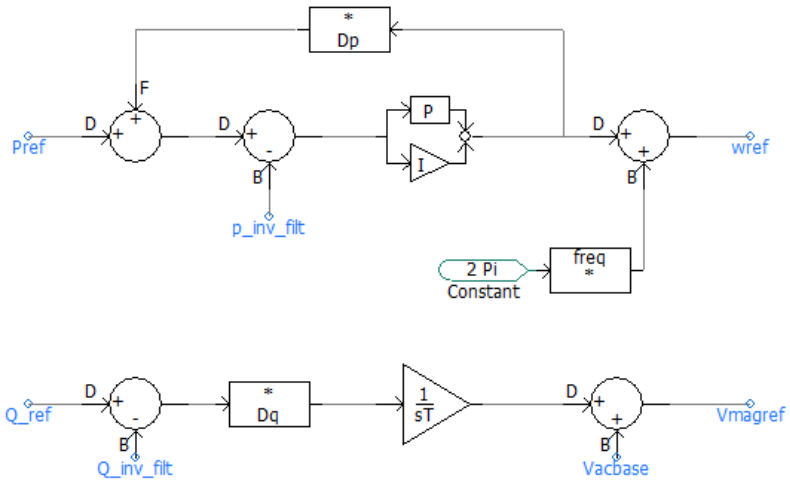

Figure 6.4: P- ω and Q - V droop controls of grid-forming inverters developed in PSCAD/EMTDC.

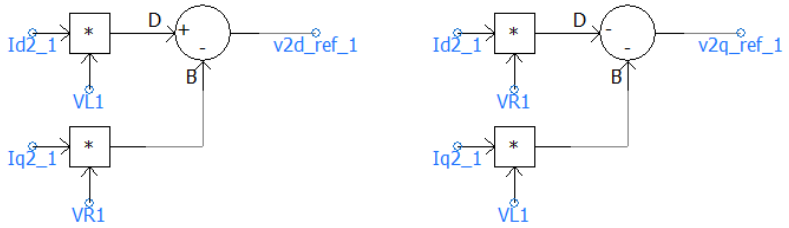

Figure 6.5: Negative-sequence virtual impedance implemented in PSCAD/EMTDC.

a negative-sequence voltage references V^*_{2dq}. The negative-sequence virtual impedance controller built in PSCAD/EMTDC is shown in Fig. 6.5. Formulas for calculating the negative-sequence voltage drop on the dq-axis is shown below,

$$V^*_{2d} = I_{2d} \cdot R_v + I_{2q} \cdot L_v, \tag{6.4}$$

$$V^*_{2q} = I_{2d} \cdot L_v - I_{2q} \cdot R_v, \tag{6.5}$$

where L_v and R_v are negative-sequence virtual impedances.

Without a virtual negative-sequence impedance ($R_v = L_v = 0$), the setpoints for V^*_{2dq} will be 0 V as described in Chapter 4. However, adding a virtual impedance applies a small negative-sequence voltage drop as shown in (6.4) and (6.5). Negative-sequence currents supplied by each inverter will be determined based on the magnitude of voltage drop.

The values of R_v and L_v are determined by the droop curve presented in Fig. 6.6. Fig. 6.6 shows droop curves of inverters having different capacities. In this example, we assume Inverter 1 has twice larger capacity compared to Inverter 2. The initial values of the two droop curves are the same, but their slopes are decided as 0.25 (ohm/A) and 0.5 (ohm/A), respectively. The $\frac{X}{R}$ ratio, initial setpoint, and slope are determined based on simulation studies. Control parameters are affected by load and line impedance.

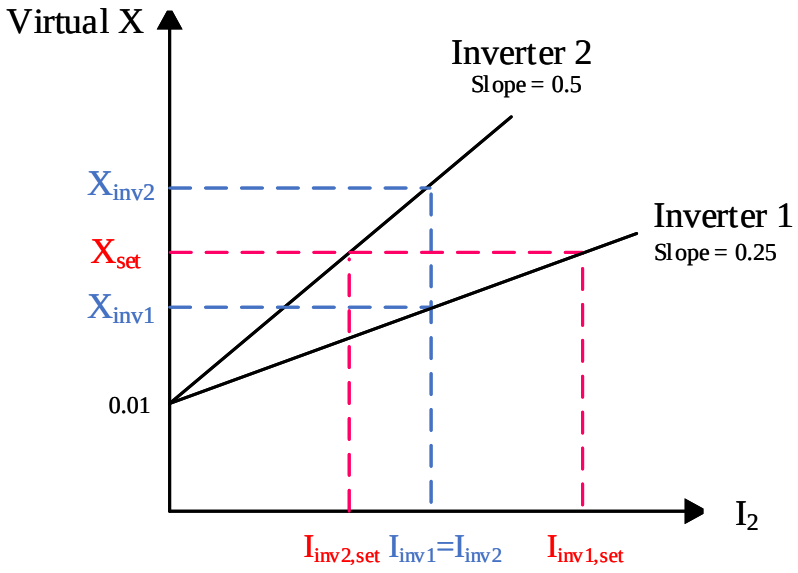

Figure 6.6: Adaptive negative-sequence virtual impedance controller with different slopes.

In the beginning, Inverter 1 and Inverter 2 supply the same amount of negative-sequence current as shown in the blue-dotted line because their initial setpoints are the same. Next, the magnitude of virtual impedances is adapted accordingly to the droop curve of each inverter until both inverters have the same negative-sequence impedance as shown in the red-dotted curve. As a result, Inverter 1 supplies more current compared to Inverter 2 ($I_{inv1,set} > I_{inv2,set}$). The ratio of negative-sequence current could be modified by choosing different slopes for droop curves.

6.3 Case Studies: Islanded Microgrid with Two Grid-Forming Inverters with Different Capacities

This section demonstrates the performance of positive-sequence droop controllers and shows the need for a negative-sequence power-sharing controller. We analyze the power and current supplied by inverters with different capacities. The inverter and test system are developed in PSCAD/ETMDC environment.

6.3.1 Test System and Simulation Scenario

An islanded microgrid with two grid-forming inverters supplying unbalanced loads is shown in Fig. 6.7. The size of unbalanced and balanced loads will be described in each simulation studies. In the first case, the load sizes are given as below:

- Balanced loads: 33.33 kW + 33.33 kvar per phase.
- Unbalanced loads,
  - Phase A: 100 kW + 100 kvar,

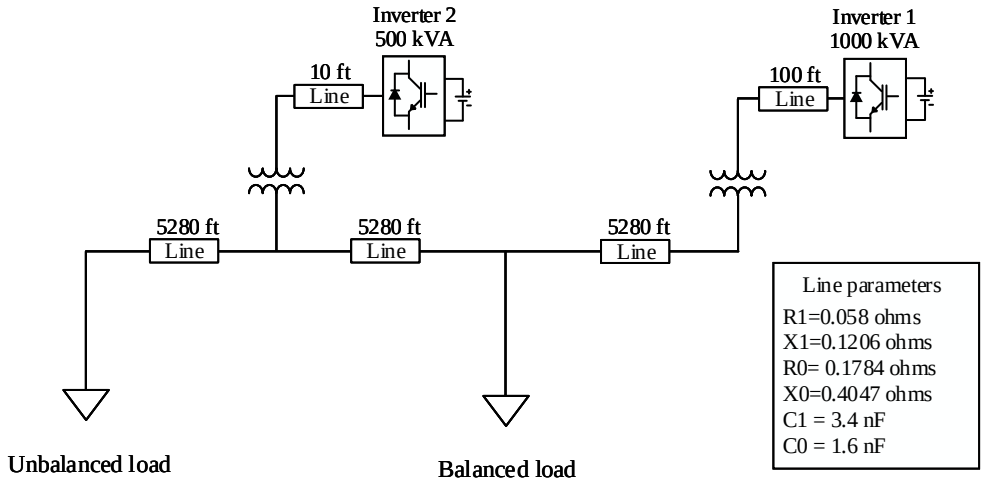

Figure 6.7: An isalanded microgrid with two grid-forming inverters having different capacities.

- Phase B: 100 kW + 100 kavr,
- Phase C: 200 kW + 150 kvar.

The two grid-forming inverters in the test system have different electrical distances to the balanced and unbalanced loads. The inverter located on the right (Inverter 1) is 1000 kVA, while the inverter on the left (Inverter 2) is 500 kVA. Since the rated capacity of Inverter 1 is twice that of Inverter 2, the power supplied by Inverter 1 is controlled to be twice that of Inverter 2. The result of power-sharing control is evaluated by comparing the ratio of power and current supplied by two inverters as shown below,

$$ratio = \frac{Measurements\ from\ Inverter1}{Measurements\ from\ Inverter2} \tag{6.6}$$

In this chapter, the objective is to control the ratio of active power, reactive power, positive-sequence current magnitude, and negative-sequence

current magnitude. Since Inverter 1 is twice larger than Inverter 2, the ratio should be controlled at 2.

6.3.2 Case 1: Grid-Forming Inverters with Positive-sequence Droop Controls Only

The first case shows the simulation results of grid-forming inverters with only positive-sequence droop controllers. The measured power and currents from both inverters are summarized in Table 6.1, and the waveforms from PSCAD/EMTDC are presented in Fig. 6.8 to 6.12. The measured voltage, current, active power, reactive power, and their ratio are presented.

The sequence components of the voltages measured at both inverters are shown in Fig. 6.8. The blue curves indicate that positive-sequence voltage of the two inverters was controlled well at 0.95 pu and 0.93 pu, respectively. The negative-sequence voltage at both inverters was both controlled at 0.01 pu, which is nearly 0 pu. The results indicate that grid voltage was regulated well with the Q -V droop and the virtual admittance controller.

Fig. 6.9 presents the sequence components of currents supplied by both inverters. Table 6.1 shows that the positive sequence current was shared properly as desired. The positive-sequence current from Inverter 1 was 1.94 times larger than that of Inverter 2. However, it can be seen that the negative-sequence currents supplied by inverters are not shared proportionally to their rated capacities. Inverter 2, which is located closer to the unbalanced load supplied more negative-sequence because we did not control the negative-sequence current injection. The improvement after adding the negative-sequence virtual impedance is presented in the next section.

It can be seen that active and reactive power presented in Fig. 6.10 and

Table 6.1: Measurements and ratios of powers and currents in Case 1.

Measurement	Inverter 1	Inverter 2	Ratio
Positive-sequence voltage[pu]	0.92	0.91	-
Negative-sequence voltage[pu]	0.01	0.01	-
Active power[kW]	336.23	166.74	2.00
Reactive power [kvar]	329.56	163.21	2.00
Positive-sequence current [A]	495.09	252.36	1.96
Negative-sequence current [A]	56.67	64.45	0.88

Fig. 6.11 are controlled accordingly to the inverter capacity. The ratios shown in Table 6.1 shows that reactive power is also controlled properly even though inverters had different electrical distances.

The ratios presented in Fig. 6.12 suggests that active power, reactive power, and positive-sequence current are distributed well to each inverter, but the negative-sequence current sharing has to be improved. From Table 6.1, it can be seen that the ratio of negative-sequence current supplied by Inverter 1 and Inverter 2 was only 0.88, which suggests that additional control for negative-sequence current sharing is needed to achieve complete power-sharing.

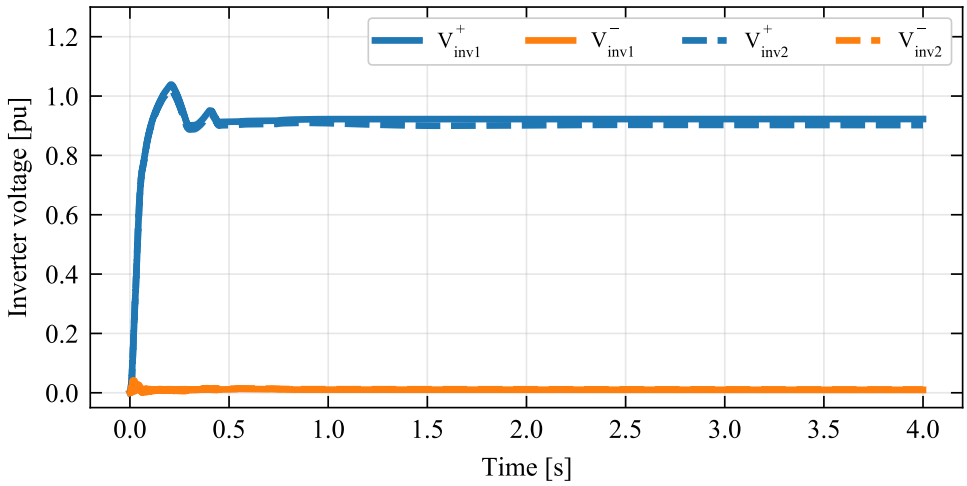

Figure 6.8: Simulation result: Positive-sequence (blue) and negative-sequence (orange) voltage of Inverter 1 (solid line) and Inverter 2 (dotted line).

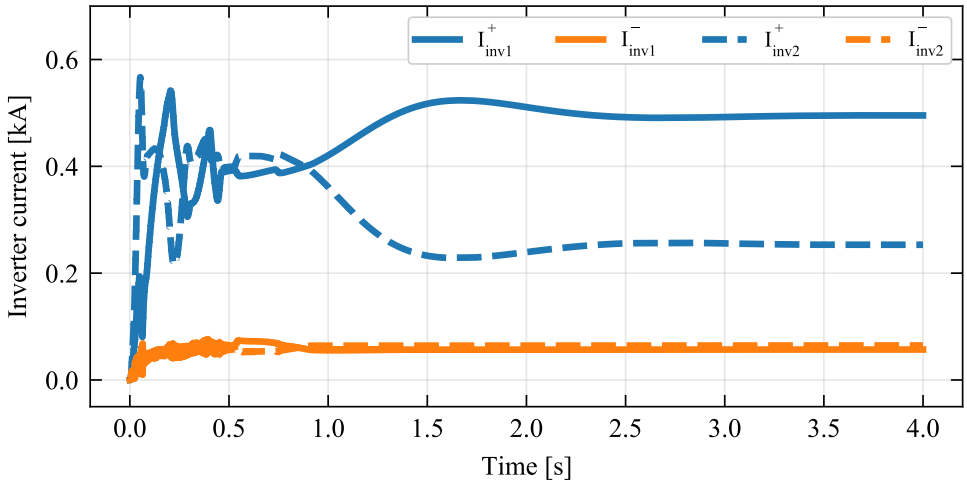

Figure 6.9: Simulation result: Positive-sequence (blue) and negative-sequence (orange) current of Inverter 1 (solid line) and Inverter 2 (dotted line).

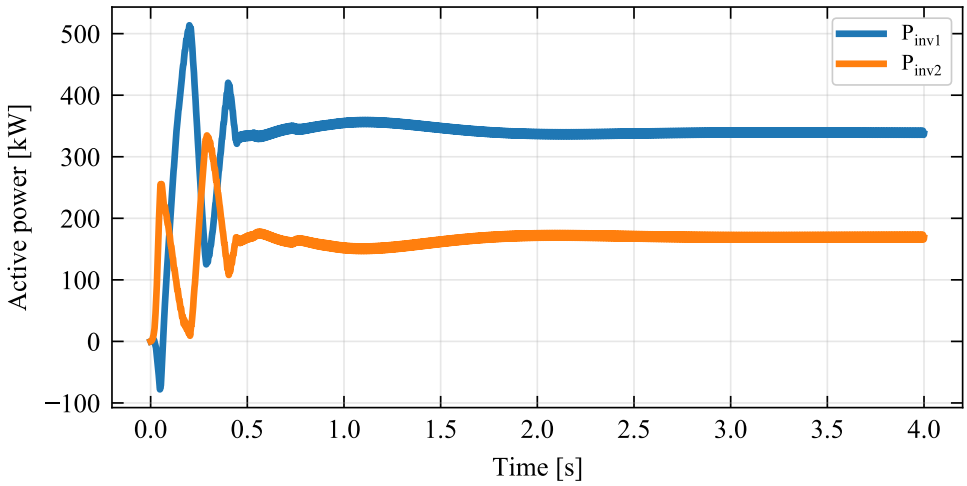

Figure 6.10: Simulation result: Measured active powers from Inverter 1 (blue) and Inverter 2 (orange).

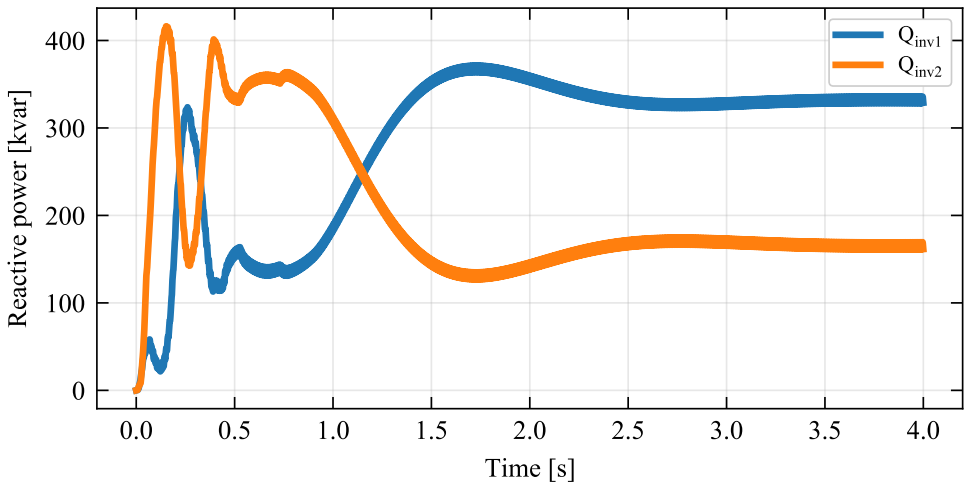

Figure 6.11: Simulation result: Measured reactive powers from Inverter 1 (blue) and Inverter 2 (orange).

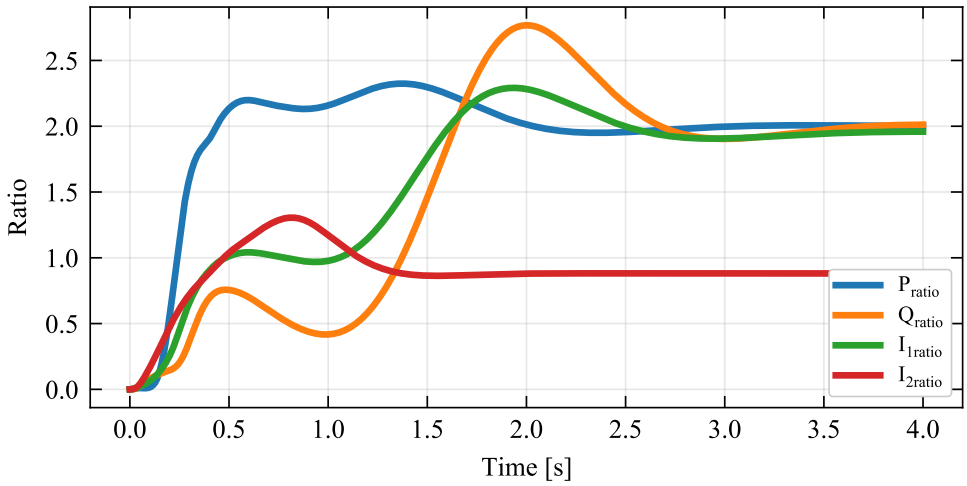

Figure 6.12: Simulation result: Ratio of measured power and currents.

6.3.3 Case 2: Grid-Forming Inverters with Negative-Sequence Adaptive Virtual Impedance Control Supplying Less Unbalanced Loads

The previous case study analyzed currents injected by each inverter without the negative-sequence current sharing controller. The simulation result showed that negative-sequence current was not controlled and determined by equivalent impedances between inverters and loads.

This case and the next case demonstrate the improvements achieved by adding an adaptive virtual impedance controller. We conduct two simulation studies with different unbalanced loads to analyze the performance of the adaptive controller presented in Fig. 6.6.

The test system displayed in Fig. 6.7 is used in this case with loads having the same rated capacities described in Section 6.3.2. At t = 0s, we start the inverters without negative-sequence virtual impedance activated. At t = 5s, the negative-sequence power sharing control is activated.

The simulation results are summarized in Table 6.2, and simulation results from EMT simulation are presented in Fig. 6.13 to 6.18. The measured voltage, current, active power, reactive power, and ratio of those are presented, respectively.

Fig. 6.13 presents the sequence components of voltages measured at both inverters. It can be seen that positive-sequence voltages observed at both inverters are controlled well at 0.92 pu and 0.91 pu, respectively. The negative-sequence voltages were also controlled successfully. Table 6.2 shows that negative-sequence voltages were both controlled at 0.01 pu. Fig. 6.13 also suggests that the voltage is not affected by the negative-sequence virtual impedance. The voltage remained steady after we activated the controller at t = 5s.

Fig. 6.14 presents the sequence components of currents supplied by both inverters. By comparing the currents presented in Fig. 6.9 and Fig. 6.14, we can observe that positive-sequence currents supplied by Inverter 1 and Inverter 2 remained constant after a short transient. However, Table 6.2 shows that the negative-sequence current sharing capability has improved a lot. The negative-

Table 6.2: Measurements and ratios of powers and currents in Case 2.

Measurement	Inverter 1	Inverter 2	Ratio
Positive-sequence voltage[pu]	0.92	0.91	-
Negative-sequence voltage[pu]	0.01	0.01	-
Active power[kW]	336.23	166.74	2
Reactive power [kvar]	329.56	163.21	1.93
Positive-sequence current [A]	495.67	253.02	1.94
Negative-sequence current [A]	89.00	45.08	1.97
Virtual Impedance [ohm]	0.032	0.035	

sequence current supplied by Inverter 1 increased from 56.57 A to 89.00 A, and the current from Inverter 2 reduced by 19.37 A from 64.45 A to 45.08 A. As a result, the ratio of negative-sequence current has increased a lot to 1.97.

The negative-sequence virtual impedances applied to each inverter are presented in Fig. 6.15. It can be seen that the virtual impedances added to Inverter 1 and Inverter 2 are almost the same, 0.032 ohm and 0.035 ohm, respectively. Even though the droop curves for adaptive control had different initial values and slopes, they were adjusted to induce the same negative-sequence voltage drop as shown in Fig. 6.6

The ratios presented in Fig. 6.18 suggests that active power, reactive power, positive-sequence current, and negative-sequence current are shared well after activating the negative-sequence virtual impedance controller. It also shows that positive-sequence components are not affected by the newly added controller.

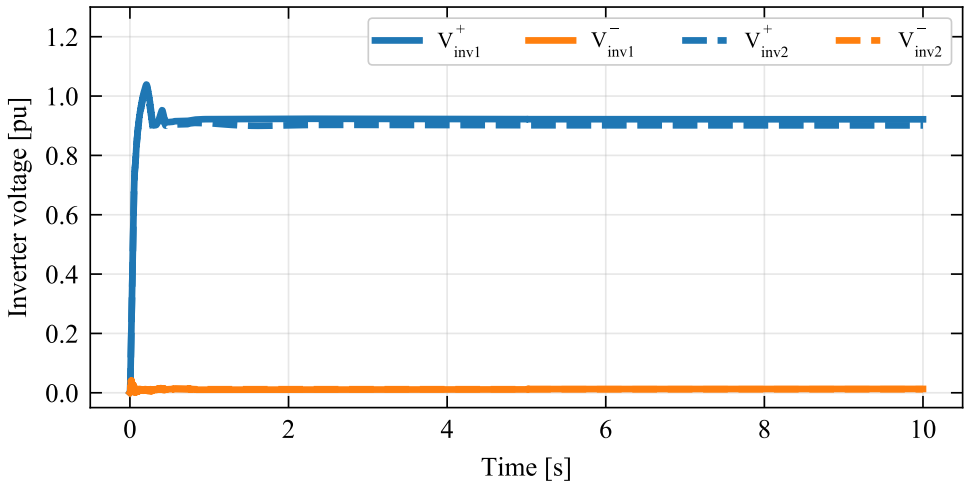

Figure 6.13: Simulation result: Positive-sequence (blue) and negative-sequence (orange) voltage of Inverter 1 (solid line) and Inverter 2 (dotted line).

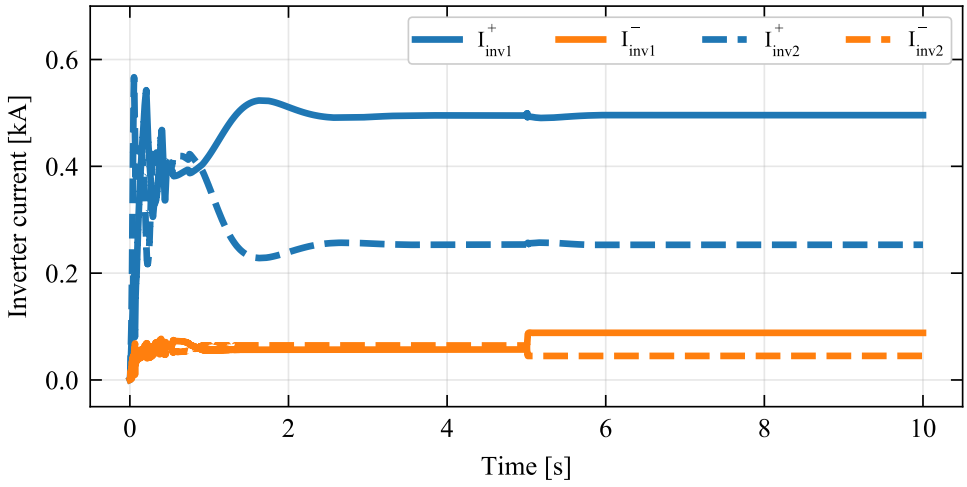

Figure 6.14: Simulation result: Positive-sequence (blue) and negative-sequence (orange) current of Inverter 1 (solid line) and Inverter 2 (dotted line).

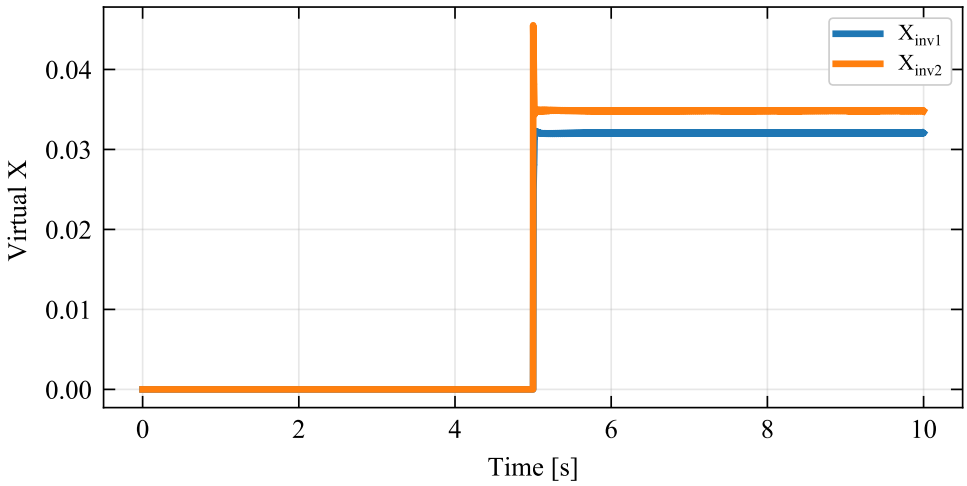

Figure 6.15: Simulation result: Virtual negative-sequence impedance added to Inverter 1 and Inverter 2.

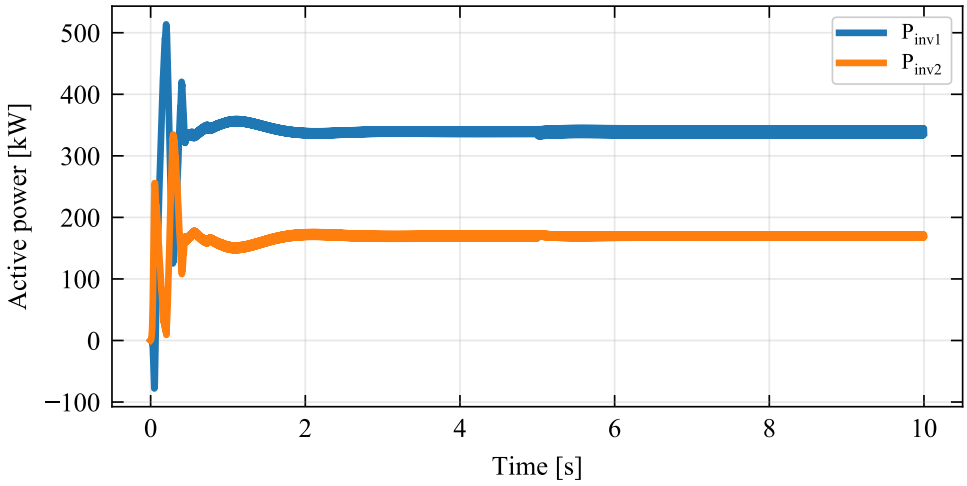

Figure 6.16: Simulation result: Measured active powers from Inverter 1 (blue) and Inverter 2 (orange).

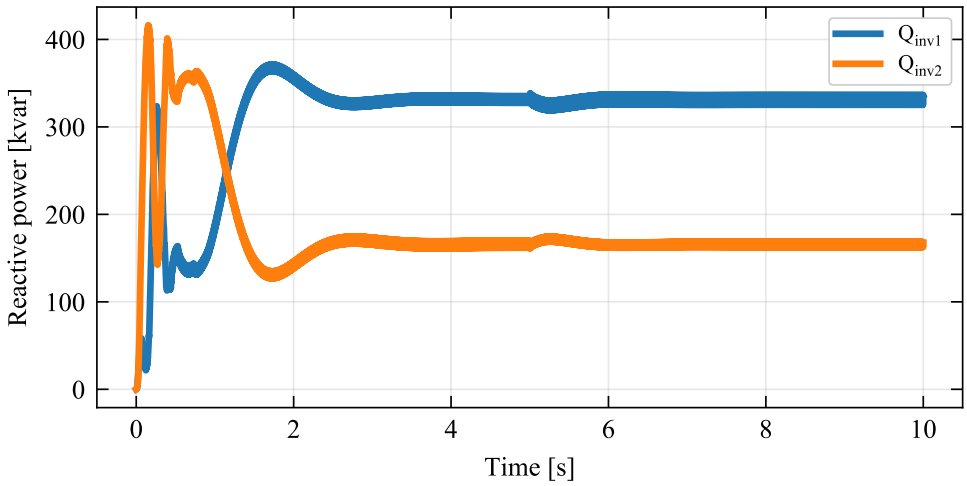

Figure 6.17: Simulation result: Measured reactive powers from Inverter 1 (blue) and Inverter 2 (orange).

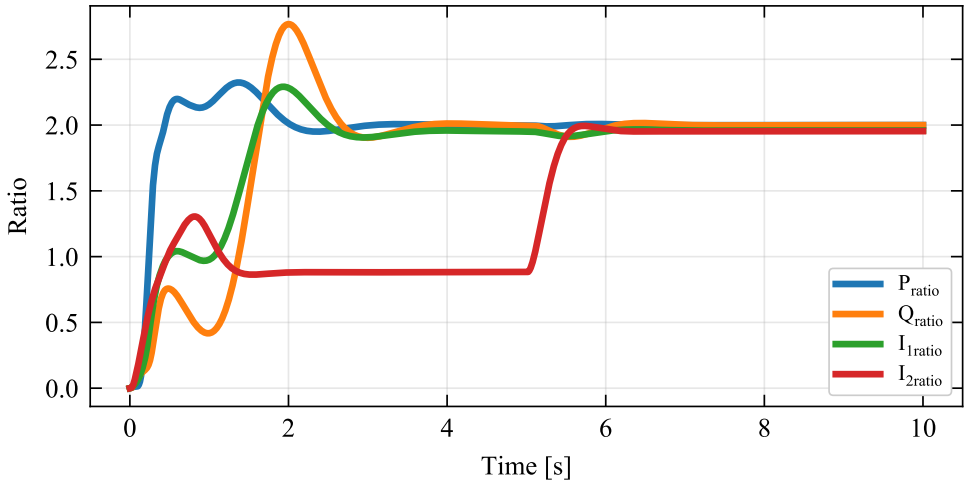

Figure 6.18: Simulation result: Ratio of measured power and currents.

6.3.4 Case 3: Grid-Forming Inverters with Negative-Sequence Adaptive Virtual Impedance Control Supplying Severely Unbalanced Loads

In Case 3, the performance of the adaptive negative-sequence controller while serving severely unbalanced load is examined. The rated sizes of unbalanced loads in the test system are adjusted as follow:

- Phase A: 50 kW + 25 kvar,
- Phase B: 50 kW + 25 kavr,
- Phase C: 200 KW + 150 kvar.

It can be seen that loads in phase A and B are smaller than the previous case. As a result, the negative-sequence current supplied by inverters and the magnitude of virtual negative-sequence impedance increased. The simulation results with more unbalanced loads are summarized in Table 6.3 and Fig. 6.19 to 6.24. Table 6.2 and Table 6.3 shows that the total negative-sequence current supplied by inverters has increased from 121.12 A to 206.32 A before the virtual impedance controller is applied.

Fig. 6.19 presents the sequence components of voltages measured at both inverters. Measured positive-sequence voltages at both inverters are 0.94 pu and 0.93 pu, respectively. The positive-sequence voltage increased slightly because the reactive power consumption of the loads decreased.

The negative-sequence voltage presented in Table 6.3 also increased slightly to 0.03 pu, as the negative-sequence current delivered by inverters increases. As a result, negative-sequence virtual impedance applied to both

Table 6.3: Measurements and ratios of powers and currents in Case 3.

Measurement	Inverter 1	Inverter 2	Ratio
Positive-sequence voltage[pu]	0.94	0.93	-
Negative-sequence voltage[pu]	0.03	0.03	-
Active power[kW]	270.83	136.37	2
Reactive power [kvar]	227.245	123.22	1.93
Positive-sequence current [A]	364.06	183.11	1.96
Negative-sequence current [A]	194.62	96.76	2.00
Virtual Impedance [ohm]	0.058	0.063	

inverters increased as explained in Fig. 6.6, and the negative-sequence voltage drop increased according to (6.4) and (6.5). Fig. 6.21 indicates that the virtual impedances of 0.058 ohm and 0.063 ohm are added to Inverter 1 and Inverter 2, respectively, which are 1.8 times larger compared to the previous case. However, the negative-sequence voltages are still within the acceptable range suggested in the ANSI C84.1 standard.

The sequence components of current supplied by each inverter are presented in Fig. 6.20. It can be seen that both positive- and negative-sequence currents are shared proportionally to the inverters' capacities. The simulation result proposes that the performance of the negative-sequence virtual impedance controller was not deteriorated even though inverters supply a large amount of negative-sequence currents. The negative-sequence current delivered by Inverter 1 increased from 89.00 A to 194.62 A, and that from Inverter 2 rose from 45.08 A to 96.76 A.

The ratios of measurements illustrated in Fig. 6.24 shows that all powers and currents were controlled according to our objective, which is sharing the current proportionally to the rated sizes of inverters.

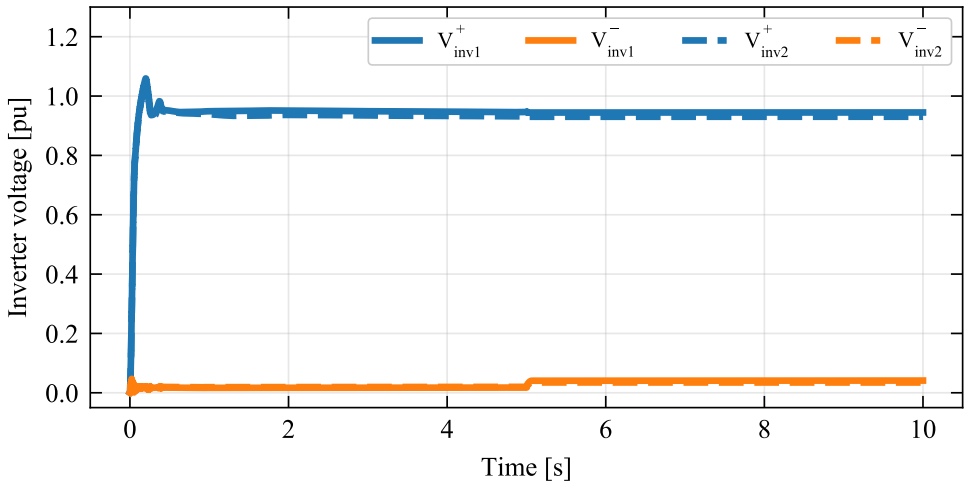

Figure 6.19: Simulation result: Positive-sequence (blue) and negative-sequence (orange) voltage of Inverter 1 (solid line) and Inverter 2 (dotted line).

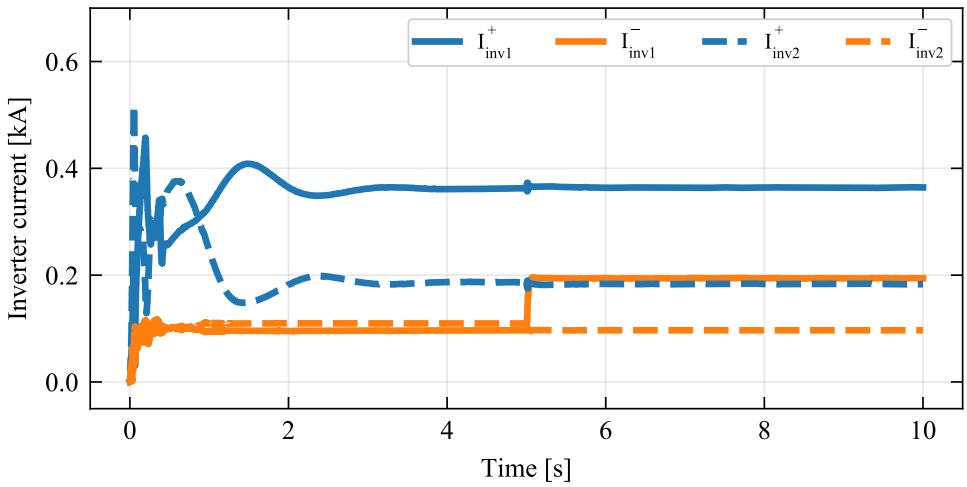

Figure 6.20: Simulation result: Positive-sequence (blue) and negative-sequence (orange) current of Inverter 1 (solid line) and Inverter 2 (dotted line).

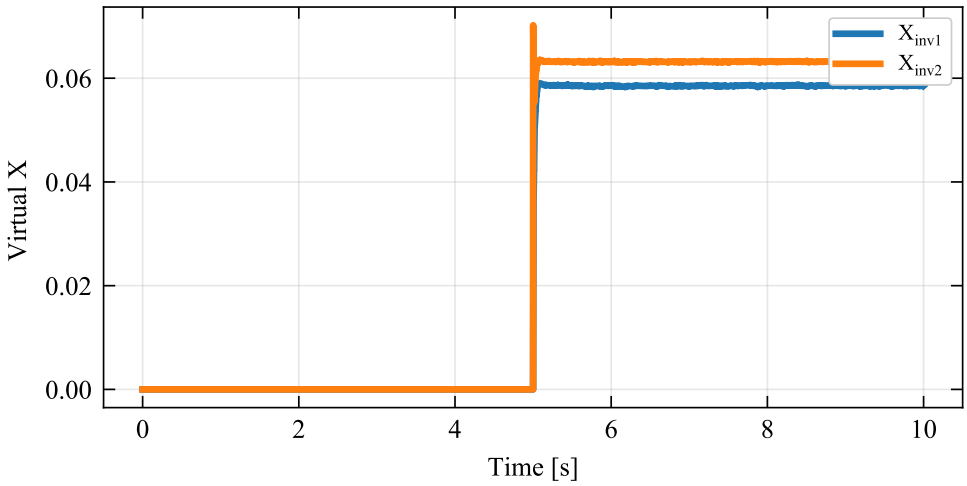

Figure 6.21: Simulation result: Virtual negative-sequence impedance added to Inverter 1 and Inverter 2.

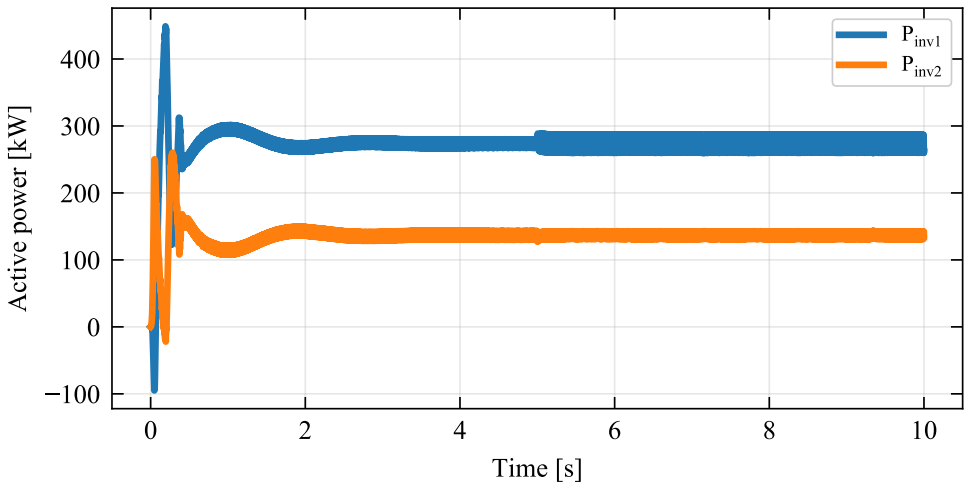

Figure 6.22: Simulation result: Measured active powers from Inverter 1 (blue) and Inverter 2 (orange).

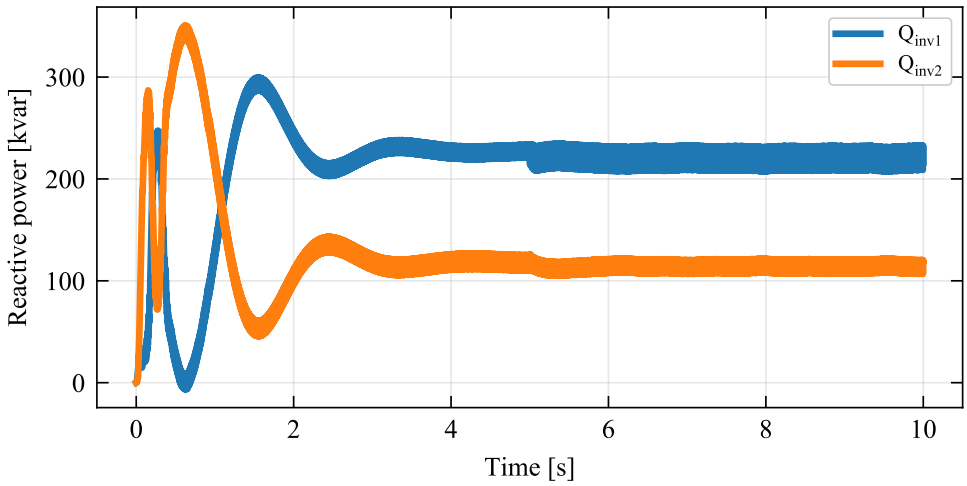

Figure 6.23: Simulation result: Measured reactive powers from Inverter 1 (blue) and Inverter 2 (orange).

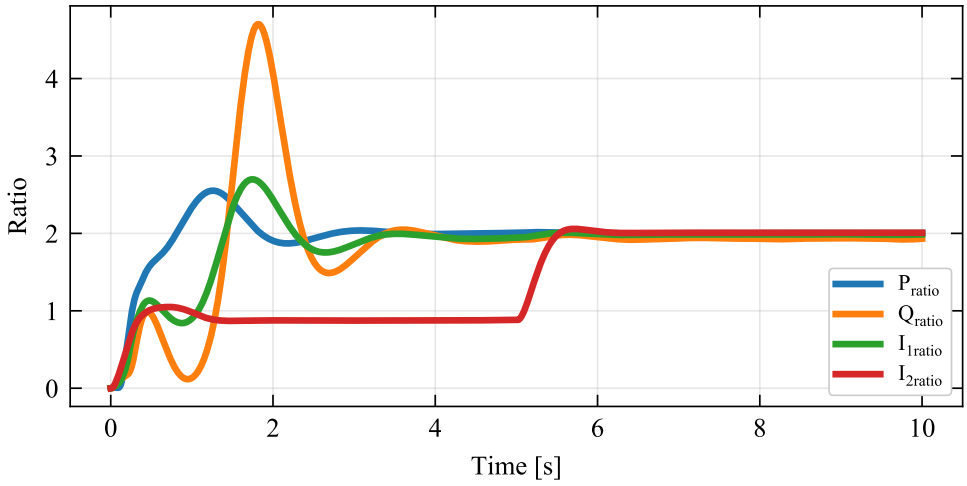

Figure 6.24: Simulation result: Ratio of measured power and currents.

6.4 Final Remarks

This chapter analyzed the operation of microgrids with multiple grid-forming inverters. A detailed model developed in PSCAD/EMTDC was used to examine the performance of controllers allocating both positive- and negative-sequence currents. Case studies showed that conventional P - ω and Q -V droop controls are capable of sharing positive-sequence current as intended. However, the negative-sequence currents supplied by each inverter was determined only by its equivalent negative-sequence impedance. Therefore, an adaptive virtual negative-sequence impedance controller was implemented to improve power-sharing capability of grid-forming inverters. Case studies demonstrated that adding an adaptive virtual negative-sequence controller improves negative-sequence current sharing and does not affect positive-sequence current supply.

Bibliography

[1] ERCOT Fact Sheet. [Online]. Available: http://www.ercot.com/content/wcm/lists/219736/ERCOT_Fact_Sheet_7.13.21.pdf

[2] A. I. A. Dissanayaka, J. Wiebe, "Panhandle and south texas stability and system strength assessment," *Available at http://www.ercot.com/*, ERCOT, Tech. Rep., 2018.

[3] L. Meegahapola and D. Flynn, "Impact on transient and frequency stability for a power system at very high wind penetration," in *IEEE PES General Meeting*, July 2010, pp. 1–8.

[4] Y. Zhou, D. D. Nguyen, P. C. Kjær, and S. Saylors, "Connecting wind power plant with weak grid - challenges and solutions," in *2013 IEEE Power Energy Society General Meeting*, 2013, pp. 1–7.

[5] *Electric Power Systems And Equipment - Voltage Ratings (60 Hz)*, National Electrical Manufacturers Association Std. ANSI C84.1, 2020.

[6] B. Meersman, B. Renders, L. Degroote, T. Vandoorn, and L. Vandevelde, "Three-phase inverter-connected dg-units and voltage unbalance," *Electric Power Systems Research*, vol. 81, no. 4, pp. 899–906, 2011.

[7] J. S. E. Rehman, M. Miller and S. H. Huang, "Dynamic stability assessment of high penetration of renewable generation in the ERCOT grid," *Available at http://www.ercot.com/*, ERCOT, Tech. Rep., 2018.

[8] P. Kundur, *Power System Stability and Control*. McGraw-Hill, Inc.

[9] NERC, "A technical reference paper fault-induced delayed voltage recovery," NERC, Tech. Rep., 2009.

[10] R. Liu, J. Yao, X. Wang, P. Sun, J. Pei, and J. Hu, "Dynamic stability analysis and improved lvrt schemes of dfig-based wind turbines during a symmetrical fault in a weak grid," *IEEE Transactions on Power Electronics*, vol. 35, no. 1, pp. 303–318, 2020.

[11] C. Wessels, F. Gebhardt, and F. W. Fuchs, "Fault ride-through of a dfig wind turbine using a dynamic voltage restorer during symmetrical and asymmetrical grid faults," *IEEE Transactions on Power Electronics*, vol. 26, no. 3, pp. 807–815, 2011.

[12] Y. Zhang, S. F. Huang, J. Schmall, J. Conto, J. Billo, and E. Rehman, "Evaluating system strength for large-scale wind plant integration," in *2014 IEEE PES General Meeting*, July 2014, pp. 1–5.

[13] D. Wu, G. Li, M. Javadi, A. M. Malyscheff, M. Hong, and J. N. Jiang, "Assessing impact of renewable energy integration on system strength using site-dependent short circuit ratio," *IEEE Transactions on Sustainable Energy*, vol. 9, no. 3, pp. 1072–1080, 2018.

[14] H. Gu, R. Yan, and T. Saha, "Review of system strength and inertia requirements for the national electricity market of australia," *CSEE Journal of Power and Energy Systems*, vol. 5, no. 3, pp. 295–305, 2019.

[15] Y. Tan, K. M. Muttaqi, P. Ciufo, and L. Meegahapola, "Enhanced frequency response strategy for a pmsg-based wind energy conversion system

using ultracapacitor in remote area power supply systems," *IEEE Transactions on Industry Applications*, vol. 53, no. 1, pp. 549–558, 2017.

[16] R. Yan, N. -Masood, T. Kumar Saha, F. Bai, and H. Gu, "The anatomy of the 2016 south australia blackout: A catastrophic event in a high renewable network," *IEEE Transactions on Power Systems*, vol. 33, no. 5, pp. 5374–5388, 2018.

[17] A. B. T. Attya and J. L. Dominguez-García, "Insights on the provision of frequency support by wind power and the impact on energy systems," *IEEE Trans. on Sustainable Energy*, vol. 9, no. 2, pp. 719–728, 2018.

[18] P. M. Ashton, C. S. Saunders, G. A. Taylor, A. M. Carter, and M. E. Bradley, "Inertia estimation of the gb power system using synchrophasor measurements," *IEEE Transactions on Power Systems*, vol. 30, no. 2, pp. 701–709, March 2015.

[19] K. Tuttelberg, J. Kilter, D. Wilson, and K. Uhlen, "Estimation of power system inertia from ambient wide area measurements," *IEEE Trans. Power System*, vol. 33, no. 6, pp. 7249–7257, Nov 2018.

[20] J. Rocabert, A. Luna, F. Blaabjerg, and P. Rodríguez, "Control of power converters in ac microgrids," *IEEE Transactions on Power Electronics*, vol. 27, no. 11, pp. 4734–4749, 2012.

[21] J. A. P. Lopes, C. L. Moreira, and A. G. Madureira, "Defining control strategies for microgrids islanded operation," *IEEE Transactions on Power Systems*, vol. 21, no. 2, pp. 916–924, 2006.

[22] H. Hooshyar and M. E. Baran, "Fault analysis on distribution feeders with high penetration of pv systems," *IEEE Transactions on Power Systems*, vol. 28, no. 3, pp. 2890–2896, 2013.

[23] B. Dağ, A. R. Boynueğri, Y. Ateş, A. Karakaş, A. Nadar, and M. Uzunoğlu, "Static modeling of microgrids for load flow and fault analysis," *IEEE Trans. on Power Systems*, vol. 32, no. 3, 2017.

[24] V. C. Cunha, T. Kim, P. Siratarnsophon, N. Barry, S. Santoso, and W. Freitas, "Quasi-static time-series power flow solution for islanded and unbalanced three-phase microgrids," *IEEE Open Access Journal of Power and Energy*, vol. 8, pp. 97–106, 2021.

[25] Q. Zhong and Y. Zeng, "Control of inverters via a virtual capacitor to achieve capacitive output impedance," *IEEE Transactions on Power Electronics*, vol. 29, no. 10, pp. 5568–5578, 2014.

[26] V. C. Cunha, T. Kim, N. Barry, P. Siratarnsophon, S. Santoso, W. Freitas, D. Ramasubramanian, and R. C. Dugan, "Generalized formulation of steady-state equivalent circuit models of grid-forming inverters," *IEEE Open Access Journal of Power and Energy*, vol. 8, pp. 352–364, 2021.

[27] A. Hooshyar and R. Iravani, "Microgrid protection," *Proceedings of the IEEE*, vol. 105, no. 7, pp. 1332–1353, 2017.

[28] H. Laaksonen and K. Kauhaniemi, "Control principles for blackstart and island operation of microgrid," ser. Proceedings of the Nordic Workshop on Power and Industrial Electronics. Helsinki University of Technology, 2008.

[29] M. Adibi, P. Clelland, L. Fink, H. Happ, R. Kafka, J. Raine, D. Scheurer, and F. Trefny, "Power system restoration - a task force report," *IEEE Transactions on Power Systems*, vol. 2, no. 2, pp. 271–277, 1987.

[30] J. C. Vasquez, J. M. Guerrero, J. Miret, M. Castilla, and L. G. de Vicuña, "Hierarchical control of intelligent microgrids," *IEEE Industrial Electronics Magazine*, vol. 4, no. 4, pp. 23–29, 2010.

[31] H. Jain, G.-S. Seo, E. Lockhart, V. Gevorgian, and B. Kroposki, "Black-start of power grids with inverter-based resources," in *2020 IEEE Power Energy Society General Meeting (PESGM)*, 2020, pp. 1–5.

[32] O. Bassey and K. L. Butler-Purry, "Black start restoration of islanded droop-controlled microgrids," *Energies*, vol. 13, no. 22, 2020.

[33] S. Alepuz, S. Busquets-Monge, J. Bordonau, J. A. Martinez-Velasco, C. A. Silva, J. Pontt, and J. Rodriguez, "Control strategies based on symmetrical components for grid-connected converters under voltage dips," *IEEE Transactions on Industrial Electronics*, vol. 56, no. 6, pp. 2162–2173, 2009.

[34] W. Jiang, Y. Wang, J. Wang, L. Wang, and H. Huang, "Maximizing instantaneous active power capability for pwm rectifier under unbalanced grid voltage dips considering the limitation of phase current," *IEEE Transactions on Industrial Electronics*, vol. 63, no. 10, pp. 5998–6009, 2016.

[35] M. M. Ghahderijani, A. Camacho, C. Moreira, M. Castilla, and L. García de Vicuña, "Imbalance-voltage mitigation in an inverter-based distributed generation system using a minimum current-based control strategy,"

IEEE Transactions on Power Delivery, vol. 35, no. 3, pp. 1399–1409, 2020.

[36] N. R. Merritt, C. Chakraborty, and P. Bajpai, "New voltage control strategies for vsc-based dg units in an unbalanced microgrid," *IEEE Transactions on Sustainable Energy*, vol. 8, no. 3, pp. 1127–1139, 2017.

[37] Y. Peng, Z. Shuai, J. M. Guerrero, Y. Li, A. Luo, and Z. J. Shen, "Performance improvement of the unbalanced voltage compensation in islanded microgrid based on small-signal analysis," *IEEE Transactions on Industrial Electronics*, vol. 67, no. 7, pp. 5531–5542, 2020.

[38] N. R. Merritt, C. Chakraborty, P. Bajpai, and B. C. Pal, "A unified control structure for grid connected and islanded mode of operation of voltage source converter based distributed generation units under unbalanced and non-linear conditions," *IEEE Trans. on Power Delivery*, 2020.

[39] Q.-C. Zhong and Y. Zeng, "Universal droop control of inverters with different types of output impedance," *IEEE Access*, vol. 4, pp. 702–712, 2016.

[40] Y. W. Li and C.-N. Kao, "An accurate power control strategy for power-electronics-interfaced distributed generation units operating in a low-voltage multibus microgrid," *IEEE Transactions on Power Electronics*, vol. 24, no. 12, pp. 2977–2988, 2009.

[41] J. He and Y. W. Li, "An enhanced microgrid load demand sharing strategy," *IEEE Transactions on Power Electronics*, vol. 27, no. 9, pp. 3984–3995, 2012.

[42] C.-T. Lee, C.-C. Chu, and P.-T. Cheng, "A new droop control method for the autonomous operation of distributed energy resource interface converters," *IEEE Transactions on Power Electronics*, vol. 28, no. 4, pp. 1980–1993, 2013.

[43] H. Zhang, S. Kim, Q. Sun, and J. Zhou, "Distributed adaptive virtual impedance control for accurate reactive power sharing based on consensus control in microgrids," *IEEE Transactions on Smart Grid*, vol. 8, no. 4, pp. 1749–1761, 2017.

[44] A. S. Vijay, S. Doolla, and M. C. Chandorkar, "Varying negative sequence virtual impedance adaptively for enhanced unbalanced power sharing among dgs in islanded ac microgrids," *IEEE Transactions on Energy Conversion*, vol. 36, no. 4, pp. 3271–3281, 2021.

[45] S. Z. Xiaoyu (Shawn) Wang and Y. Cheng, "2020 panhandle regional stability study," *Available at http://www.ercot.com/content/wcm/lists/197392/2020_PanhandleStudy_public_final__004_.pdf*, ERCOT, Tech. Rep., 2020.

[46] D. Ke, C. Y. Chung, J. Xu, Y. Shen, and Y. Sun, "Inertia emulation uncorrelated with electromechanical dynamics to improve frequency transients using center of inertia (coi) frequency signal," *IEEE Transactions on Power Systems*, pp. 1–1, 2020.

[47] Y. Li, Z. Xu, and K. P. Wong, "Advanced control strategies of pmsg-based wind turbines for system inertia support," *IEEE Transactions on Power Systems*, vol. 32, no. 4, pp. 3027–3037, 2017.

[48] Literature-based power flow test cases. [Online]. Available: http://icseg.iti.illinois.edu/power-cases/

[49] D. N. Hussein, M. Matar, and R. Iravani, "A type-4 wind power plant equivalent model for the analysis of electromagnetic transients in power systems," *IEEE Transactions on Power Systems*, vol. 28, no. 3, pp. 3096–3104, 2013.

[50] NERC, "Phase angle monitoring: Industry experience following the 2011 pacific southwest outage," NERC, Tech. Rep., 2016.

[51] N. Bottrell and T. C. Green, "Comparison of current-limiting strategies during fault ride-through of inverters to prevent latch-up and wind-up," *IEEE Trans. on Power Electronics*, vol. 29, no. 7, pp. 3786–3797, 2014.

[52] B. Mahamedi, M. Eskandari, J. E. Fletcher, and J. Zhu, "Sequence-based control strategy with current limiting for the fault ride-through of inverter-interfaced distributed generators," *IEEE Transactions on Sustainable Energy*, vol. 11, no. 1, pp. 165–174, 2020.

[53] X. Wang, L. Harnefors, and F. Blaabjerg, "Unified impedance model of grid-connected voltage-source converters," *IEEE Transactions on Power Electronics*, vol. 33, no. 2, pp. 1775–1787, 2018.

[54] Hong-Seok Song and Kwanghee Nam, "Dual current control scheme for pwm converter under unbalanced input voltage conditions," *IEEE Transactions on Industrial Electronics*, vol. 46, no. 5, pp. 953–959, 1999.

[55] "IEEE recommended practice for conducting motor-starting studies and analysis of industrial and commercial power systems," *IEEE Std 3002.7-2018*, pp. 1–107, 2019.

[56] R. F. Arritt and R. C. Dugan, "Distributed generation interconnection transformer and grounding selection," in *2008 IEEE Power and Energy Society General Meeting - Conversion and Delivery of Electrical Energy in the 21st Century*, 2008, pp. 1–7.

[57] Application note: Interconnection guidelines for Yaskawa Solectria solar transformerless inverters. [Online]. Available: https://solectria.com/technical-support/documentation-1/

[58] J. Ghijselen and A. Van den Bossche, "Exact voltage unbalance assessment without phase measurements," *IEEE Transactions on Power Systems*, vol. 20, no. 1, pp. 519–520, 2005.